

2005

Heat transfer phenomena in foams infiltrated with phase change materials: applications to cooling for electronics and energy storage devices

Osama M. S. Mesalhy
University of Dayton

Follow this and additional works at: https://ecommons.udayton.edu/graduate_theses

Recommended Citation

Mesalhy, Osama M. S., "Heat transfer phenomena in foams infiltrated with phase change materials: applications to cooling for electronics and energy storage devices" (2005). *Graduate Theses and Dissertations*. 4384.

https://ecommons.udayton.edu/graduate_theses/4384

This Dissertation is brought to you for free and open access by the Theses and Dissertations at eCommons. It has been accepted for inclusion in Graduate Theses and Dissertations by an authorized administrator of eCommons. For more information, please contact mschlange1@udayton.edu, ecommons@udayton.edu.

**HEAT TRANSFER PHENOMENA IN FOAMS INFILTRATED WITH
PHASE CHANGE MATERIALS: APPLICATIONS TO
COOLING FOR ELECTRONICS AND
ENERGY STORAGE DEVICES**

A Dissertation Submitted to
The School of Engineering of the
UNIVERSITY OF DAYTON

In Partial Fulfillment of the Requirements for
The Degree of
Doctor of Philosophy in Mechanical Engineering

by
Osama M. S. Mesalhy

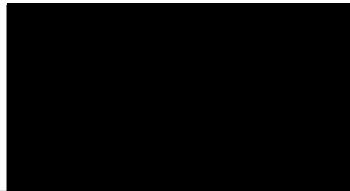
UNIVERSITY OF DAYTON

Dayton, Ohio

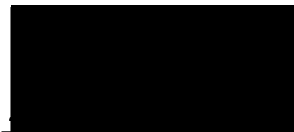
August, 2005

HEAT TRANSFER PHENOMENA IN FOAMS INFILTRATED WITH PHASE
CHANGE MATERIALS: APPLICATIONS TO COOLING FOR ELECTRONICS AND
ENERGY STORAGE DEVICES

APPROVED BY:



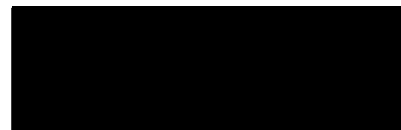
Khalid Lafdi, Ph.D.
Advisory Committee Chairman
Professor, Mechanical and
Aerospace Engineering Department



Kevin Hallinan, Ph.D.
Committee Member
Professor and Chair of Mechanical and
Aerospace Engineering Department



Robert Brockman, Ph.D.
Committee Member
Professor, Mechanical and
Aerospace Engineering Department



William Lee, Ph.D.
Committee Member
Professor, Chemical and Material
Engineering Department



Donald L. Moon, Ph.D.
Associate Dean
Graduate Engineering Programs & Research
School of Engineering



Joseph E. Saliba, Ph.D., P.E.
Dean, School of Engineering

ABSTRACT

Heat Transfer Phenomena in Foams Infiltrated With Phase Change Materials: Applications to Cooling for Electronics and Energy Storage Devices

Name: Osama M.S. Mesalhy

University of Dayton

Adviser: Dr. Khalid Lafdi

With the extremely rapid progress in developing new micro-electronic devices and the urgent need to harvest and store energy, designing a new generation of heat sinks and energy storage devices has become important. The materials used in these applications should possess high heat capacity and high thermal conductivity. Phase Change Materials (PCMs) have a huge heat capacity but low thermal conductivity. On the other hand, foams exhibit high thermal conductivity, low weight, and good mechanical properties.

A composite of a PCM infiltrated inside a high thermal conductivity foam was used in designing a heat sink and an energy storage device. First, a novel numerical technique was developed to solve the conservation equations of mass, momentum and energy in such a composite. A two-energy equation model was used to tackle the local thermal non-equilibrium between the two phases. The conservation equations were formulated in non-orthogonal curvilinear coordinates to accommodate both regular and irregular geometries. Second, an

experimental test rig was built to measure the thermal conductivity of the foam materials and to capture the temperature and the melting evolution of the PCM inside aluminum and carbon foams. The numerical model predicted the temperature field and the location of the solid-liquid interface during the melting process accurately compared to the experimental results.

Then, the numerical model was used to make a design optimization for the heat sink and the energy storage. Generally, it was found that using such high thermal conductivity foams significantly enhanced the performance. The performance of the heat sink for steady heat generation electronics enhanced with decreasing foam porosity, increasing foam pore size, and with activating the foam surface energy. Changing the geometry and inserting internal fins also showed little enhancement, while changing the heat sink orientation made the biggest impact on the performance. For electronics subjected to fluctuating energy spikes, the presence of the PCM showed a tremendous reduction in the heat sink resistance. For energy storage design, it was found that using high thermal conductivity foams showed significant improvements of the storage output power. The output power improved with increasing foam thermal conductivity and foam pore size.

NOMENCLATURE

A_S, N, W, E coefficients of the discretized equation

A area (m^2)

a_{sf} interfacial surface area

Bi Biot number ($h_{sf} a_{sf} l^2/k$)

c_p specific heat ($J/kg\ K$)

C Forchheimer coefficient

Da Darcy number (K/l^2)

d_p pore diameter (m)

d_{fi} fiber diameter (m)

Fo Fourier number ($\alpha t/l^2$)

g gravity acceleration (m/s^2)

h_{sf} interfacial heat transfer coefficient (W/m^2K)

J transformation Jacobian

K permeability (m^2)

k thermal conductivity (W/mK)

L latent heat of fusion (J/kg)

l length scale (m)

Pr Prandtl number ($\mu c_p/k$)

p static pressure (Pa)

Ra	Rayleigh number ($g\beta\Delta T l^3/\alpha\nu$)	Ste	Stefan number ($c_p\Delta T/L$)
T	temperature (K)		
t	time (sec.)		
u	velocity in x-direction (m/s)		
v	velocity in y-direction (m/s)		
x	distance in x-direction		
y	distance in y-direction		

Greek letters

α	thermal diffusivity (m^2/s)
β	thermal expansion coefficient ($1/K$)
χ	tortuosity
δ	porosity of solid matrix
ε	liquid phase fraction
ξ, η	coordinates in computational plane
ρ	density (kg/m^3)
Δt	time step (s)
Γ_ϕ	diffusion coefficient for any variable ϕ
μ	dynamic viscosity ($kg/(m.s)$)
τ_{ij}	stress tensor
θ	non-dimensional temperature

Subscripts

E,W,N,S	neighboring cells to point P, east, west, north, and south
---------	--

e,w,n,s	neighboring faces to point P, east, west, north, and south
f	fluid phase
eff	effective
s	solid matrix phase
sf	interfacial

Superscripts

old	beginning of time step
k	iteration number

LIST OF FIGURES

CHAPTER 3 MATHEMATICAL AND NUMERICAL MODEL

Fig. 3.1 2-D hexagonal pore and 3-D interconnected fiber models	54
Fig. 3.2 Foam effective thermal conductivity versus porosity	55
Fig. 3.3 2-D representation for the pore	57
Fig. 3.4 Pore corner approximation	57
Fig. 3.5 Change of area ratio with carbon surface energy	59
Fig. 3.6 Typical control volume in computational domain	62
Fig. 3.7 Enthalpy change with temperature during phase change	68
Fig. 3.8 Simple flow chart for the numerical procedure	73
Fig. 3.9 Geometry and grid for the rectangular cavity	76
Fig. 3.10 Velocity vectors and temperature contours at early stage of melting, $Fo=0.1045$ and 0.209	76
Fig. 3.11 Velocity vectors and temperature contours at later stage of melting, $Fo=0.418$, and 0.627	77
Fig. 3.12 Comparison between experimental and numerical liquid-solid interface at different times	78
Fig. 3.13 Grid for the irregular energy storage	79
Fig. 3.14 Velocity vectors and temperature contours at different times for irregular energy storage	80
Fig. 3.15 Comparison of liquid solid interface at $Fo = 0.1296$	81
Fig. 3.16 Velocity vectors and temperature contours for porous cavity $Da=1.37E-5$, $Ra=7.19E5$	83

Fig. 3.17 Comparison of temperature profile with experimental measurements for the porous cavity.....	83
Fig. 3.18 Fluid temperature contours for different Da (a) $Da = 1.37E-5$, $Ra = 7.19E5$, (b) $Da = 1.162E-3$, $Ra = 7.19E5$	85
Fig. 3.19 Solid-liquid temperature difference contours for different Da, (a) $Da = 1.37E-5$, $Ra = 7.19E5$, (b) $Da = 1.162E-3$, $Ra = 7.19E5$	85
Fig. 3.20 Fluid temperature contours for different Ra (a) $Da = 2.035E-4$, $Ra = 1.438E5$, (b) $Da = 2.035E-4$, $Ra = 3.595E6$	86
Fig. 3.21 Solid-liquid temperature difference contours for different Ra (a) $Da = 2.035E-4$, $Ra = 1.438E5$, (b) $Da = 2.035E-4$, $Ra = 3.595E6$	86
 CHAPTER 4 EXPERIMENTAL WORK	
Fig. 4.1 Test rig for thermal conductivity measurements (The number between brackets is the thermocouple number).....	91
Fig. 4.2 Temperature time history and the calculated effective thermal conductivity for foam 20PPI, 6.1%, near the steady state condition.....	93
Fig. 4.3 DSC melting point and latent heat measurements.....	96
Fig. 4.4 Variation of pure wax viscosity with temperature.....	98
Fig. 4.5 Viscosity-temperature variations of wax with 3 % fume silicate.....	99
Fig. 4.6 Test rig.....	100
Fig. 4.7 Thermocouples locations.....	102
Fig. 4.8 Liquid-solid interface at time= 75 min from applying the heat for different porosity aluminum foam.....	103
Fig. 4.9 Heater temperature time history for different density Al foam.....	105
Fig. 4.10 Liquid-solid interface at time = 80 min from applying the heat for different pore size aluminum foams.....	105
Fig. 4.11 Temperature time history for different pore size foams.....	106

Fig. 4.12 Liquid-solid interface for aluminum foam (6.6% and 10PPI) with different wax viscosity at time = 80 min.....	107
---	-----

Fig. 4.13 Temperature time history of the heater for different values of wax viscosity.....	108
--	-----

CHAPTER 5 PERFORMANCE OF FOAM-PCM COMPOSITE AS A HEAT SINK AND ENERGY STORAGE

Fig. 5.1 Comparison between numerical and experimental solid-liquid interface for aluminum foam 10PPI, 93.4% porosity.....	115
---	-----

Fig. 5.2 Temperature time history at different points at the same level.....	116
--	-----

Fig. 5.3 Temperature-time history at different points in different levels.....	117
--	-----

Fig. (5.4) Effect of changing pore size of the foam on steady state heater temperature.....	118
--	-----

Fig. 5.5 Non-dimensional temperature against Fourier Number at the beginning of melting.....	120
---	-----

Fig. 5.6 Effect of porosity on the steady state heater temperature.....	120
---	-----

Fig. 5.7 Heater temperature for different wax viscosity.....	121
--	-----

Fig. 5.8 Solid liquid interface for different wax viscosity.....	122
--	-----

Fig. 5.9 Physical domain of the heat sink.....	124
--	-----

Fig. 5.10 PCM and solid phase temperature contours Continuous (solid), Dotted (PCM).....	126
---	-----

Fig. 5.11 Junction temperature at different locations for Al foam (porosity =94%, and Pore size= 10PPI).....	127
---	-----

Fig. 5.12 Maximum junction temperature for different foam porosity.....	129
---	-----

Fig. 5.13 Maximum junction temperature for different foam pore size.....	130
--	-----

Fig. 5.14 Maximum junction temperature for different interfacial heat transfer Coefficient.....	130
--	-----

Fig. 5.15 PCM temperature contours for a heat sink supported with one and two fins.....	132
--	-----

Fig. 5.16 Maximum junction temperature for using fins.....	132
Fig. 5.17 PCM phase temperature contours for different angles (80 ⁰ , and 70 ⁰).....	134
Fig. 5.18 PCM phase temperature contours for bottom heating.....	134
Fig. 5.19 PCM phase temperature contours for top heating.....	135
Fig. 5.20 Maximum junction temperature for different shapes and orientations.....	135
Fig. 5.21 Heat flux at the left side for fluctuating energy.....	136
Fig. 5.22 Maximum junction temperature for different latent heat.....	137
Fig. 5.23 Maximum junction temperature for different melting temperature.....	137
Fig. 5.24 Solar receiver.....	140
Fig. 5.25 The computational model for the energy Storage.....	141
Fig. 5.26 Output power from the solar receiver for different foam thermal conductivity.....	142
Fig. (5.27) Liquid fraction contours at the end of the first cycle charging time time=20 min.....	143
Fig 5.28 Liquid fraction contours for pure PCM at different times.....	144
Fig. 5.29 Changing of energy storage output power with time for using different porosity Al foam.....	145
Fig. 5.30 Changing of energy storage output power with time for using Different pore size Al foam.....	146

LIST OF TABLES

CHAPTER 3 MATHEMATICAL AND NUMERICAL MODEL

Table 3.1 Source term definitions.....	51
Table 3.2 Run inputs for melting inside the irregular geometry.....	82

CHAPTER 4 EXPERIMENTAL WORK

Table 4.1 Aluminum foam properties.....	90
Table 4.2 Measured thermal conductivity of the Aluminum foam.....	92
Table 4.3 Surface energy of the carbon foam.....	95
Table 4.4 Wax properties.....	97
Table 4.5 Results for Carbon foam.....	109

CHAPTER 5 PERFORMANCE OF FOAM-PCM COMPOSITE AS A HEAT SINK AND ENERGY STORAGE

Table 5.1 PCM properties for the heat sink.....	125
Table 5.2 Changing of HSR for different foam properties.....	131
Table 5-3 HSR for adding fins and changing shape and orientation.....	146
Table (5.4) HSR for fluctuating heat generation.....	138
Table 5.5 High melting temperature PCM (LiF-CaF ₂) properties [109].....	141

TABLE OF CONTENTS

Abstract	iii
Nomenclature	v
List of Figures	viii
List of Tables	xii
CHAPTER 1 INTRODUCTION	1
CHAPTER 2 LITRATURE REVIEW	7
2.1 Introduction	7
2.2 Review	8
2.2.1 Solid-liquid phase change heat transfer	8
2.2.1.1 Analytical solutions	9
2.2.1.2 Experimental Methods	11
2.2.1.3 Numerical Techniques	13
2.2.2 Ways to enhance thermal conductivity of PCM	20
2.2.3 Foam materials	23
2.2.4 Conduction and convection heat transfer in porous media	26
2.2.5 PCM in energy storage and cooling applications	28
2.2.6 Effect of surface characteristics during phase change	36
2.3 Work statement	38
2.4 Goals and objectives	41
CHAPTER 3 MATHEMATICAL AND NUMERICAL MODEL	43
3.1 Introduction	43
3.2 Mathematical Modeling	44
3.2.1 Volume averaging technique	44
3.2.2 Local thermal equilibrium	46
3.2.3 Governing equations in 2-D general coordinates	48
3.2.4 Important non-dimensional parameters	51
3.2.5 Modeling of effective thermal conductivity	53
3.2.6 Modeling of carbon foam wettability	55

3.3 Numerical Technique	58
3.3.1 Grid generation	59
3.3.2 Discretization of conservation equations	61
3.3.3 Treatment of Momentum equations	64
3.3.4 Treatment of phase change and evolution of liquid-solid Interface	67
3.4 Numerical procedures	72
3.5 Validations	74
3.5.1 Melting of Pure Gallium inside rectangular cavity	75
3.5.2 Melting of pure PCM in irregular geometry	78
3.5.3 Convection heat transfer in a porous cavity	82
CHAPTER 4 EXPERIMENTAL WORK	87
4.1 Introduction	87
4.2 Experimental facilities	88
4.2.1 Guarded hot plate (As a heat source)	88
4.2.2 Data acquisition	88
4.2.3 Samples	89
4.3 Thermal conductivity measurements	90
4.4 Carbon foam surface activation and surface energy measurements	94
4.5 Measuring PCM properties	95
4.5.1 Thermal properties	95
4.5.2 Viscosity	97
4.6 Enclosure manufacturing	99
4.6.1 Visual tracing of the liquid solid interface	102
4.7 Results for Aluminum foam	103
4.8 Results for carbon foam	107
CHAPTER 5 NUMERICAL RESULTS AND PERFORMANCE OF FOAM-PCM COMPOSITE AS A HEAT SINK AND ENERGY STORAGE	110
5.1 Introduction	110
5.2 Numerical treatment of energy exchange between the PCM and solid materials	110
5.3 Numerical model validation with the experimental work	113
5.4 Heat sink	123
5.4.1 Design parameters of the Foam-PCM heat sink	124
5.4.2 Steady heat generation	126
5.4.2.1 Changing foam porosity, pore size, and interfacial heat transfer coefficient	128
5.4.2.2 Adding fins	130
5.4.2.3 Changing shape and orientation	132
5.4.3 Performance for fluctuating heat generation	135
5.5 Energy storage	138
5. 5.1 Effect of using carbon foam for space applications	140

5.5.2 Using Aluminum foam in energy storage for ground Applications	143
CHAPTER 6 CONCLUSIONS AND RECOMMENDATIONS.....	147
REFERENCES	152

CHAPTER 1

INTRODUCTION

With the extremely rapid progress in developing new micro-electronic devices and the urgent need to harvest and store energy, thermal control and the design of a new generation of energy storage have grown in importance. Thermal control issues appear in designing small size electronic chips, which are subjected to high heat generation densities, and in controlling space vehicles from the excessive aerodynamic heating. In designing a thermal protection system of such applications, selecting the materials is a very important issue. The materials used should have high specific heat with high thermal conductivity to be able to absorb and diffuse heat quickly. Moreover, in spacecraft applications, these materials should possess high specific stiffness and strength as well as creep resistance and resistance to oxidation at elevated temperatures.

In electronic cooling applications, temperature stabilization requirements typically range from near ambient (20 °C) up to (100 °C). Using active cooling by circulating a coolant fluid to absorb the heat from these kinds of electronic chips is known to consume too much power and to add complexity to the system design. Therefore, developing a new generation of electronic devices, which have high capabilities and high mobility, requires using passive cooling

systems, which can be achieved using PCMs. These systems do not need any power for cooling. In some cases, just a DC fan represents the best compromised solution. In new electronic applications, the electronic chips are subjected to high heat fluxes due to the increasing demand to reduce their sizes and to increase their functions. The generated heat from these electronic chips may be steady or transient in multi-chip modules and sensors that operate irregularly or have variable power. Dissipating heat from these devices and suppressing temperature overshoots during the transient power spikes has become an important challenge in electronic packaging design.

Conversely, in space applications, energy storage is a critical task. In space vehicles, the electrical power is generated by photovoltaic solar arrays. These solar arrays employ a concentrator to collect and focus the solar energy into PCM energy storage where it is converted to thermal energy. A fraction of this thermal energy is transferred to a circulating working fluid to run the heat engine and produce electrical power. The remaining thermal energy is used to melt the PCM contained in the energy storage. The PCM stores the excess energy by undergoing phase change at its transition temperature. This permits continuous operation of the heat engine during the substantial eclipse periods where there is no solar energy available. The response time or the time for charging and discharging is a key factor in designing any energy storage system, especially applications that are restricted to a limited time for energy absorption. The charging or discharging time of the energy storage depends mainly on the

thermal properties of the energy storage material. The higher the thermal conductivity the better response this energy storage can achieve.

This study is intended to address phase change materials, which have been gaining popularity due to their ease of handling and high performance. By definition, PCMs are those materials that experience phase change from solid-solid, solid-liquid or liquid-gas under normal operating conditions. The advantage of this type of material in energy storage or temperature control stems from their higher heat capacity and the isothermal nature of the phase change process. A negative aspect of PCMs is that most of these materials suffer from inherent low thermal conductivity. The lower thermal conductivity of these materials increases the charging and discharging time for any PCM energy storage. Also, in the case of temperature control of electronic devices, the low thermal conductivity of the PCM makes the temperature shoot up rapidly once the melting interface moves away from the surface subjected to the heat flux.

Thermal performance of PCM energy storage or PCM heat spreaders could be improved by enhancing the thermal conductivity of PCMs. Several techniques were invented to enhance PCMs thermal conductivity. The first attempt was the design of a PCM storage container from a high thermal conductivity material with sufficient surface to volume ratio. But this technique was not effective, because it put a restriction on the PCM storage capacity. Other techniques have been used to enhance the inherent thermal conductivity of the PCM, such as adding metal fillers, additive or fins, using porous Silica catalyst or porous activated carbon, and using carbon fibers. Using high thermal

conductivity metal or graphite foams could be a superior technique because of their high thermal conductivity and their good mechanical properties. In this thesis, we will concentrate on using high thermal conductivity foams to enhance the performance of the PCM as an energy storage medium and as a heat spreader for electronic devices.

Studying the thermal performance of PCM energy storage or heat spreading supported by high thermal conductivity foam is a complicated process. Besides the complex nature of heat transfer with melting due to the presence of a moving interface between solid and liquid phases, the heat will diffuse with different speeds inside both the PCM and the foam phases due to the great difference in their thermal properties. Also, the phase change process will keep the temperature of the PCM phase nearly constant during its phase transition period. This will generate local thermal non-equilibrium, which will generate heat exchange between the two phases. The heat exchange between the two phases will be affected by the surface characteristics of the foam and its interfacial surface area. Moreover, the liquid phase of the PCM will move inside the porous media due to buoyancy forces. This liquid motion could enhance the heat transfer process, but it will make the performance of the system sensitive to orientation. The intensity of the convection motion will depend on the permeability of the porous media. So, to optimize the thermal performance of such a complicated system, a great importance should be placed on both the foam and PCM properties.

The aim of this study is to investigate in detail numerically and experimentally the phenomenon of phase change of PCMs inside high thermal conductivity foams. The practical use of this study, as mentioned before, could appear in thermal management applications, such as energy harvesting, active and passive cooling of electronic devices, and energy storage systems. Throughout this study, we will develop a numerical model capable of dealing with conduction/convection heat transfer with phase change inside foam-PCM composite.

Chapter 2 focuses on previous researches that investigate phase change (solid-liquid) heat transfer, enhancement of PCM thermal conductivity, conduction and convection heat transfer in porous media, and the use of PCM in electronic cooling and energy storing. Finally, a work statement and the objective of the current work will be presented.

Chapter 3 states the mathematical formulations and the numerical solution technique for conduction-convection heat transfer with phase change inside high thermal conductivity foam impregnated with PCM. A two-energy equation model will be employed in this work due to the great difference in thermal properties between the two phases. In addition, simple models to predict the effective thermal conductivity and wettability of the porous foam will be presented. Some case studies will be discussed. These cases will include melting of pure PCM inside cavity and irregular geometry energy storage, and convection heat transfer in a cavity filled with glass beads saturated with liquid Gallium.

In chapter 4, an experimental test rig is used to measure the foam thermal conductivity and to capture the temperature and liquid-solid interface motion during melting of low melting temperature wax inside high porosity Aluminum foams. The experimental results are used to validate the numerical technique proposed in chapter 3. In chapter 5, the numerical model is compared with the experimental measurements. In addition, a numerical design is carried out to simulate electronic heat sink and energy storage devices using a PCM supported with high thermal conductivity foam. Finally, chapter 6 covers some conclusions and recommendations for future work.

CHAPTER 2

LITRATURE REVIEW

2.1 Introduction

Studying hybrid foam-phase change materials behavior in thermal management systems and energy storage is very complex. It includes many interacting and competitive mechanisms such as phase change of the PCM, heat diffusion in a multi-component system, and convection motion of the molten liquid inside the solid porous matrix. Then, the system performance is dependent on many parameters such as the effective conductivity of the foam, pore size, and surface area of the foam as well as the PCM properties such as melting point, liquid phase viscosity and latent heat. So, to optimize the thermal performance of such a complicated system, a great importance should be focused on these parameters.

Due to the need to highlight the aforementioned related phenomena, a review for the researches related to phase change and heat transfer in porous media is presented in this chapter. This review includes phase change of pure PCMs, methods to enhance PCMs thermal conductivity, properties of foam materials, conduction and convection heat transfer inside porous media, and the

practical researches for the use of PCMs in energy storage, thermal protection, and cooling of electronic devices.

2.2 Review

2.2.1 Solid-Liquid phase change heat transfer

The phase structure of many materials changes as the temperature of the material reaches a certain transition point. The phase transformation could be solid-solid, solid-liquid, or liquid-gas. During the phase transformation, the structure of the material changes and a certain amount of energy is absorbed or released to achieve this phase transformation. Conventional types of solid-liquid PCMs are paraffin waxes, mineral salts, metal alloys, and some types of polymers.

The analysis of heat transfer problems involving melting and solidification processes lies under the category of moving boundary problems. Studying melting and solidification processes is complicated due to the fact that the solid-liquid boundary moves depending on the speed at which the latent heat is absorbed or lost at the boundary, so that the position of the boundary is not known a priori and forms a part of the solution. For the theoretical analysis of phase change phenomena, a simultaneous solution is needed for the Fourier equation in the solid phase and for the mass, momentum and energy equations in the liquid phase coupled with proper boundary conditions at the solid-liquid interface. This makes the analytical model strongly nonlinear. Further difficulties arise when two or three-dimensional geometries are considered or temperature dependence of the thermo-physical properties is taken into account. For all these

reasons, only limited analytical solutions exist and most of the predictions mainly depend on experiments and numerical techniques.

2.2.1.1 Analytical solutions

The analytical solutions of phase change are mainly based on solving the Stefan moving boundary problems. The effect of liquid phase motion and consequently the convection heat is neglected. An extensive review for the analytical techniques for solving such moving boundary problems is presented by Crank [1] and Zerroukat et al. [2]. The experimental data for melting and solidification of PCMs showed that the convection motion of the liquid phase due to the buoyancy effects has a great effect on the rate of melting and solidification. Soma and Dutta [3] conducted experimental and theoretical work to describe the melting characteristics of paraffin wax encapsulated between two concentric cylinders. It was found that the melting time depends on the rate of natural convection; the higher the rate of natural convection the smaller the melting time. When considering the liquid phase motion, the analytical formulation of the phase change problem became very difficult to be analytically solved. The analytical solutions for phase change problems considering liquid phase convection motion have been constrained to solve contact melting problems. In this type of problem, the liquid phase layer was assumed to be very small so that the flow equations could be simplified and solved explicitly from the energy equation.

Bareiss and Beer [4] studied analytically the temporal geometric shape, melting rates, and heat flux for melting of PCM inside a metallic isothermally heated copper tube. A force balance between pressure forces in a thin liquid

layer between the bottom of the sinking solid bulk and the heated tube wall and the gravitational force of the solid bulk allowed a closed-form solution of the melting process. For contact melting, Moallemi and Viskanta [5] developed a mathematical model for melting of a solid, which was continuously in close contact with a heat source. They assumed that the heat source and the solid phase are continuously separated by a very thin film in which the flow is predominantly in one direction. Following the same process, Lacroix [6] set a mathematical model for contact melting of a subcooled PCM inside a heated parallelepipedic capsule. He simplified the momentum equation and solved it explicitly from the energy equation. His results indicated that the melted fraction from close contact melting at the bottom of the capsule was larger, by an order of magnitude, than that from the conduction dominated melting from the top. The steady close-contact melting occurring between a PCM and an isothermally heated flat surface in relative motion was investigated analytically by Hoseon et al. [7]. Transverse convection across the liquid film and solid-liquid density change had been taken into account.

In the case of buoyancy driven convection motion of the liquid phase, the energy equation and flow equations are coupled together through the buoyancy source term which appears in the momentum equation. In this case, the momentum equation should be solved simultaneously with the energy equations. This will make the analytical solution not viable.

2.2.1.2 Experimental Methods

Many experimental works have been carried out to study melting processes of PCMs, to investigate the heat transfer regimes during phase change processes, and to study melting characteristics of some PCMs. Wang et al. [8] investigated the melting process in the vicinity of a heated vertical wall. The liquid flow patterns during the melting process were captured and the instantaneous marching of the liquid-solid interface was presented. It was found that during the melting process, three different heat transfer regimes were identified; these are pure conduction mode, transition mode, and convection mode. The critical Rayleigh number where the transition from the conduction to the convection regime occurs was found to be in the range of 7.869×10^6 - 3.237×10^7 . The role of natural convection on the solid-liquid interface during melting and solidification of Lipowitz metal and pure Gallium in a rectangular cavity were studied by Gau and Viskanta [9, 10]. The measurements of both temperature distributions and temperature fluctuations were used as a qualitative indication of the natural convection flow regimes and structures of melting during the phase transformation. For melting, the measured melt volume and heat transfer coefficients were correlated in terms of relevant dimensionless parameters. For solidification, the measured volume of metal solidified on the wall was compared with predictions based on a one-dimensional model.

Ho and Viskanta [11] used a shadowgraph technique to study the melting of n-octadecane from an isothermal vertical wall. The shadowgraph technique was used to measure the local heat transfer coefficients at the hot surface, and

the solid-liquid interface motion during the phase change was recorded photographically. For melting from heat flux wall, Debabrata and Yogendra [12] studied melting of organic PCM, n-triacontane, in a side heated tall enclosure of aspect ratio 10, by a uniform dissipating heat source. Experimental visualization of melt front locations was performed. Their results showed that natural convection plays a dominant role during initial stages of melting.

Melting of a mixture of PCMs has been studied experimentally to investigate the enhancing of heat absorption of energy storage by using multiple phase change materials. Melting characteristics of a mixture of stearic acid, sliced paraffin, and Lauric acid encapsulated in a cylindrical storage was studied experimentally [13]. The results showed that using multiple PCMs enhances the charging rate of the PCM energy storage. Also, Ahmet et al. [14, 15] investigated experimentally palmitic acid and an eutectic mixture of palmitic and stearic acids as a PCM in a simple tube-in-tube heat exchanger. It was observed that the convection heat transfer in the liquid phase plays an important role in the melting process and the melting and solidification times can be changed by placing the PCM storage in different positions. Experimental results also showed that the eutectic mixture had good phase change and heat transfer characteristics during the melting and solidification processes, and it is an attractive candidate as a potential PCM for heat storage in latent heat thermal energy storage systems.

Knowing PCM Thermal behavior in devices under periodic heat loads is crucial. Giovani [16] numerically and experimentally the periodic heating of a plane slab of PCM from the top by applying a sinusoidal heat flow. He found that

the system is able to act as a damper of entering energy oscillations and the heat flux emerging from the output surface was almost constant.

2.2.1.3 Numerical Techniques

In general there are different numerical methods for solving problems of heat transfer and fluid flow during phase change processes. In the past, finite difference methods have been frequently used for problems of flow and heat transfer in regular geometries [17,18]. Recently, Mittal et al. [19] developed a method for solving flow and heat transfer around immersed bodies using orthogonal grid, but this still needs a lot of programming effort. On the other hand, finite volume method is a very powerful tool for solving heat transfer and fluid flow equations. For curvilinear systems, finite volume technique has been found to be very efficient in conjunction with numerical grid generation [20-22]. Numerical grid generation has become an integral part of the curvilinear control volume technique. The literature on grid generation techniques is vast and growing rapidly. Extensive surveys have been presented by Warsi [23] and Eisenman [24].

The numerical methods for handling moving solid-liquid interface during phase change processes can be classified into the so-called Eulerian, Lagrangian, and Eulerian-Lagrangian methods. In the Lagrangian methods, the domain is divided into two zones, one for liquid and one for solid. A certain grid line is supposed to coincide with the liquid-solid interface. In this way, the grid should be adapted for every time step during the solution, and the motion of the interface is defined by applying an energy balance at the interface region. In the

Lagrangian methods, the required jump conditions can be easily applied across the interface, and the interface is strictly treated as a discontinuity without any numerical diffusion.

Using Lagrangian technique, Sparrow, et al. [25] analyzed the transient multidimensional melting, which takes into account the natural convection induced by temperature differences in the liquid melt. The molten region was created by a vertical heated tube embedded in a solid PCM at its fusion temperature. Solutions were obtained by an implicit finite-difference scheme capable of treating the movement of the liquid-solid interface. A numerical study of natural convection melting within an isothermal vertical cylinder was conducted by Yong and Lacroix [26]. They formulated the governing equations in terms of a stream function, vorticity, and temperature. Body-fitted coordinates were employed for tracking the irregular shape of the time-wise changing solid-liquid phase front. Their numerical results showed that the convective flow patterns and time evolution of the phase front, resulting from simultaneous bottom, side, and top heating, are more complicated than those for melting from a single isothermal boundary. Damir and Gretar [27] presented a new front tracking method to simulate time dependent two-dimensional dendritic solidification of pure substances. Their method was based on a finite difference approximation of the heat equation and explicit tracking of the liquid-solid interface. This method was also easily able to simulate surface tension and kinetic mobility anisotropies as well as topology changes.

Lagrangian methods can be used successfully in some of the phase-change problems in which the PCM is subjected to severe volume changes. For example, it has been used to investigate a molten micro-droplet impact and solidification on a cooler flat substrate of the same material that melts due to the energy input from the impacting molten material [28]. The melted volume was determined and presented as a function of time for various combinations of thermal and fluid dynamics parameters. In the same way, Sripada et al. [29] studied melting and rolling up due to surface tension of a metallic wire electrode heated from below. This problem was a three-phase problem (solid, liquid, and the ambient medium) with two simultaneous interfaces. The outer interface was tracked by orthogonal grid generation conforming with the evolving boundary surface at each time interval.

Numerical grid generation with front fixing techniques has been used to solve phase change problems in a Lagrangian way. Dursunkaya and Odabasi [30] used this technique to study the solidification of an infinitely long square prism. It was assumed that the liquid phase is at the melting temperature throughout the computation, so the convection motion effects were neglected. In the same way, Kamal et al. [31] performed a numerical study for the melting of PCM around a horizontal circular cylinder of constant wall temperature in the presence of the natural convection in the melt region. The phase change front was immobilized by using coordinate transformation and the method of control volume used to discretize the governing equations.

On the other hand, the Eulerian approach uses a fixed computational grid. A single set of conservation equations and boundary conditions are used for the whole domain. As a result of this, an additional field variable should be introduced to model the presence of the moving liquid-solid interface on the grid. The interface is not explicitly tracked but has to be constructed from the distribution of the field variable. This variable could be liquid fraction or total enthalpy. The energy equation is formulated in terms of total enthalpy, which represents both of the sensible and latent heat parts. Two different formulations of the energy conservation equation could be derived for Eulerian methods, namely: apparent heat capacity and latent heat source [32]. In the apparent heat capacity method, the specific heat is set as a function of temperature, which has an artificial jump around the melting temperature. On the other hand, the latent heat source method represents the heat absorption or release due to the phase change process by adding a heat source/sink term in the energy equation.

Since the whole domain is formulated with the same set of equations in Eulerian methods, the zero velocity condition should be assigned to the solid region. This could be accomplished in two approaches. The first requires setting the viscosity of the solid phase equal to a very big number, which in turn will bring all the velocities to zeros. The second approach, which is known as enthalpy-porosity method, accomplishes this condition by adding a source term to the momentum equation. This approach depends on considering the cell that undergoes phase-change as a pseudo-porous media with a porosity equal to the liquid fraction of that cell.

Fixed grid or Eulerian techniques have been used successfully by many authors to model phase-change problems. Brent et al. [33] used the enthalpy porosity method to study the melting of pure metal in a rectangular cavity. The left and right sides of this cavity were kept at constant temperatures while the bottom and top sides were insulated. The numerical results showed agreement with the experimental data. Asko et al. [34, 35] employed the enthalpy-porosity method to study the melting of an unfixed rectangular PCM in a low gravitational environment while considering the effect of density change during phase change. The PCM was initially at its melting temperature and the lower surface of the container was exposed to a uniform temperature higher than the melting point. A parametric study has been presented to investigate the effect of Archimedes number, Stefan number, Prandtl number, and the geometric parameters on the phase change process. They mentioned that in a low gravity environment, the melting rate became very slow. Melting and solidification of a pure metal in a rectangular cavity has been studied numerically by Rady and Mohanty [36] using an enthalpy-porosity method. They noticed that, during solidification, the recirculation cells vanished with time while the numerical results from the multi-zone (Lagrangian) method predicted their enlargement. They showed that the results from the enthalpy-porosity method agreed with the experimental data.

Ghasemi and Molki [37] used fixed grid enthalpy method to study the melting of an unfixed solid in a square cavity. The cavity was initially filled with the solid material and all four walls were heated to a temperature above the melting. This made the solid release as a result of melting near the walls. Falling

of the solid in the melt and the buoyancy were the main factors affecting the liquid motion and the melting process.

Following the enthalpy-porosity method, Sasaguchi et al. [38] developed a numerical model to study solid-liquid phase change in a complicated geometry using a general coordinate system. Solidification calculations of pure water around a single cylinder or two cylinders were performed to check the validity of their model. Ng et al [39] presented a finite element method to simulate the convection dominated melting of PCM in a cylindrical-horizontal annulus heated isothermally from an inside wall. Their mathematical model was based on the enthalpy-porosity method. They studied the effects of Rayleigh number on the melting rate as well as the evolution of the flow patterns. Their results revealed that an increase in Rayleigh number promoted the heat transfer rate and generated multiple cellular flow patterns in the molten region. Different configurations have been studied using the same finite element model by Khillarkar et al. [40]. They considered melting of an organic PCM occupied between a square external channel and a circular inner tube. They studied the effect of Rayleigh number as well as heating from inside, outside or both walls at a temperature above the melting point of the PCM on the melting process.

The flow pattern formation in the molten region beside a vertical wall of a rectangular cavity has been studied by Fulvio and Marilena [41]. A structure of a multiple cells has been found during the first stage of melting while a merging of the small recirculating cells into larger ones was observed during the following stage of the transient melting. A grid sensitivity study has been carried out to

ensure the validity of the model. They found that only the use of a fine mesh allows the observation of the multi-cellular flow structure. Scanlon and Stickland [42] investigated buoyancy driven melting and freezing using the commercial software FLUENT. The model used in this software is based on the fixed-grid enthalpy-porosity method. In this study, different materials were considered such as Lauric acid and water. A non-Boussinesq approach was considered which accounts for any density extrema in the flow, particularly for the density inversion found in water.

The fixed grid method is very useful and convenient in modeling mushy zone region (the region which has liquid fraction from 0-1 between solid and liquid phase). This is because it does not consider the solid-liquid interface as a thin layer with negligible thickness as Lagrangian methods does. Ilegbusi and Mat [43] developed a hybrid model for the mushy region as a non-Newtonian semi-solid medium below the coherency point and a porous medium thereafter. The validity of their model was tested on the solidification of a generic binary alloy in a two-dimensional rectangular cavity. The predictions included temporal evolution of the flow and thermal fields and spatial distribution of the viscosity, velocity components and temperature. Using the same model, they studied the solidification of an aqueous ammonium chloride ($\text{NH}_4\text{Cl}-\text{H}_2\text{O}$) solution inside a two dimensional cavity [44]. A critical solid fraction was chosen as that corresponding to the coherency point, where a solid skeleton begins to form. Their numerical results showed that the solidification of a hypereutectic $\text{NH}_4\text{Cl}-\text{H}_2\text{O}$ solution was mainly characterized by the rejection of solute at the mushy

region and double diffusive convection induced by the opposing solutal and thermal buoyancy forces.

In the Eulerian-Lagrangian method a fixed grid is used, and the interface is explicitly tracked by means of marker particles [45, 46]. So, this method has the advantage of simplicity like the fixed grid method as well as the ability to easily incorporate the surface forces arising from the elasticity of the interface or the surface tension like the Lagrangian method.

Finally, we can say that, there are advantages and disadvantages of the Lagrangian, or the moving boundary fitted grid approach in comparison with the fixed grid methods. Lagrangian approach makes the application of the required interfacial conditions straightforward because the phase boundary coincides with a grid line. The main drawback of this approach is the difficulty of handling complex geometries and topological changes, such as merger and breakup of the interface. Also, it cannot model mushy regions.

2.2.2 Ways to enhance thermal conductivity of PCM

Use of PCMs in heat protection applications requires a high melting temperature, high thermal conductivity, and high latent heat. Most of the existing PCMs present low thermal conductivity. This property reduces the rate of heat storage and extraction, so the response of these PCMs to sudden high heating fluxes is not good. In the case of space based power systems, this represents a great issue because a large amount of heat should be stored or dissipated in a short period of time. As reported by Bugaje [47] the phase change (melting or

solidification) time is the most important design parameter in latent heat storage systems.

The lower thermal conductivity of the PCM can be enhanced by using metal filler additives, fins, or metal porous structures. Experiments were carried out by Bogaje [47] to investigate the methods of enhancing the thermal response of paraffin wax heat storage tubes by incorporating aluminum thermal conductivity promoters of various designs into the body of the wax. He used aluminum sheets and expanded aluminum matrices. It was found that the melting and solidification times were reduced significantly due to these promoters. For Energy storage systems for spacecraft applications, Chow et al. [48] concluded that the effective thermal conductivity of the PCM can be significantly increased by using smaller encapsulated PCMs enclosed in a container filled with a liquid metal. Siegel [49] has studied the improvement of the solidification rate in molten salt dispersed with high thermal conductivity particles. He concluded that even though there was an improvement in heat transfer rate, there was a compensating effect due to the reduction in volume fraction occupied by the phase change material.

Velraj et al. [50] performed a detailed investigation for different heat transfer enhancement methods for the latent heat thermal storage system, such as using fins and lessing rings. They concluded that applying these methods was highly suitable for solidification enhancement. Experiments were performed by Cabeza et al. [51] in a small energy storage device to study heat transfer

improvement in PCM with the addition of stainless steel pieces and copper pieces. The PCM used was water. They noticed that addition of steel pieces did not increase the heat flux significantly but adding copper had a significant effect on enhancing the heat transfer process. Uros [52] presented an experimental work to investigate melting and solidification of paraffin and the time dependent storage of heat in the PCM with and without steel fins for heat transfer enhancement. Through this study, new correlations between Nusselt and Rayleigh numbers were made.

Due to the attractive properties of carbon fibers, Fukai et al. [53,54] investigated experimentally two thermal conductivity enhancement techniques using carbon fibers. In the first technique, the fibers were randomly distributed in the PCM while in the second technique they used fiber brushes such that the directions of the fibers coincided with the heat transfer direction. Their results showed that the two methods were useful in enhancing the thermal conductivity, and using fiber brushes was better in enhancing the thermal conductivity in the fiber direction. Hamada et al. [55] also studied experimentally and numerically using carbon fiber chips and carbon brushes as additives to enhance the performance of PCM energy storage. They considered the effect of these additives on the thermal resistance beside the heat transfer walls. They mentioned that the carbon fiber chips were effective for improving the heat transfer rate but they found that the thermal resistance near the heat transfer surface was higher than that for carbon brushes. As a result, the overall heat

transfer rate for fiber chips was lower than that for carbon brushes even though the effective thermal conductivity of the bulk of the former was higher.

On the other hand, some researchers tried to study the enhancement of the thermal conductivity of the PCM using a porous matrix. Hoogendoorn and Bart [56] have reported that the low thermal conductivity of the PCM can be greatly enhanced by embedding a metal matrix structure in them. Erk and Dudukovic [57] utilized low-density additives such as porous silica catalyst while Eltouney et al. [58] used metal screens/spheres placed inside the PCM. Maurant et al. [59] used a solid matrix made of graphite as a support for low thermal conductivity reactive salts. This support presented several advantages such as achieving a high external heat transfer coefficient, very low bulk density, good mechanical properties, and chemical inertness. Graphite matrix is known to be superior to porous metallic foams made of aluminum, copper or nickel. Py et al. [60] proposed a supported PCM made of paraffin impregnated by capillary forces in a graphite matrix. They found that the thermal conductivity of the composite was equal to that of the sole porous graphite matrix. Moreover, the composite presented the same anisotropy with respect to the compression axis.

2.2.3 Foam materials

Porous media has been used for several years in various engineering applications as well as in the environment. Heat and mass transfer in packed beds, underground water flow, and heat pipes are some of these applications. Porous media is characterized by the presence of two or more phases. One of these phases is solid and the others can be fluid or just void spaces. The ratio

between void volumes to the total volume is called porosity. The porosity of porous media ranges from low values for packed beads to high values for open cell metal foams. In open cell metal or carbon foams, the void spaces are connected to each other. Open cell metal foams are suitable to be used as a heat sink due to their high thermal conductivity and permeability for fluid flow. The properties which have the most important impact on thermal performance of such foams are the effective thermal conductivity, interfacial surface area, and the permeability of this material to fluid phase motion.

The metal foams have an open cell structure composed of dodecahedron-like cells, which have pentagonal or hexagonal faces. The edges of these cells are composed of metal fibers and, typically, there is a lumping of metal at the intersection of the fibers. The fibrous matrix is usually made of Aluminum, Nickel, or Copper. Two quantities, the porosity and the pore density, are used to characterize the foam. The pore density is expressed in units of pores per inch (PPI). The cross section of the fiber is a function of porosity, and changes from a circle at lower porosity to a concave triangle at higher porosity.

Defining the effective thermal conductivity of porous media saturated with fluid has been tackled by many researchers, starting with the pioneer work of Maxwell in 1891[61] to define the effective thermal conductivity of packed beds of cylinders and spheres. Kaviany [62] has provided an extensive review of the available literature on the subject along with a number of correlations and their ranges of applicability. The thermal conductivity of the porous media depends on the thermal conductivity of both solid and fluid phase, the porosity, and the pore

shape, which define the tortuous path of the heat flow. Calmidi and Mahjan [63] investigated the effective thermal conductivity of high porosity Aluminum foam experimentally. Their experiments were conducted using both air and water as the fluid phase. Besides the experiments, a theoretical model based on one-dimensional heat conduction was derived. The foam structure was considered as a two dimensional hexagonal shape. A three dimensional cell geometry of metal foam has been proposed by Boomsma, and Poulikaks [64]. The shape was assumed to be like a tetrakaidecahedron, which consists of 14 faces, eight hexagons, and six squares. The vertices of the tetrakaidecahedron were connected to each other with metallic cylindrical cross section bars. This model also was based on 1-D heat conduction in the metallic foam ligaments.

The effective thermal conductivity and permeability of Al foam has been measured by Peak et al. [65]. They investigated the effect of porosity and pore size on the foam properties. The effective thermal conductivity was found to increase with decreasing porosity, but it showed little difference with changing pore size. On the other hand, pressure drop across the foam was strongly affected by the cell size as well as the porosity. They found that the pressure drop reached its minimum value at a porosity equal to 0.94 at a fixed pore size. An extensive experimental investigation for the determination of the effective thermal conductivity and permeability has been carried out by Bhattacharya et al. [66]. They showed also that the effective thermal conductivity depends on the porosity and the ratio of the cross-sections of the fiber. However, no systematic dependence was found on the pore density.

To determine the permeability of high porosity metal foam Du Plessis et al. [67] and Fourie [68] developed theoretical models to predict the pressure drop in a Newtonian fluid flowing through highly porous, isotropic metallic foams. Their models were based on rigorous assumptions of piece-wise plane Poiseuille flow and a simplistic geometrical model. Their models showed accurate predictions of the hydrodynamic conditions in both Darcy and Forchheimer regimes without a priori knowledge of the flow behavior of the particular metallic foam.

2.2.4 Conduction and convection heat transfer in porous media

There are limited studies dealing with phase change processes (melting and solidification) inside porous media. All of these studies are restricted to the study of melting and solidification processes of PCM inside packed beds. Freezing and melting of water in saturated porous media contained in various enclosures have been studied experimentally and numerically by Weaver and Viskanta [69], Chellaiah and Viskanta [70]. Their freezing experiments in a rectangular cavity clearly showed the influence of natural convection on the solid/liquid interface shape and motion. The transient behavior and heat transfer for melting of ice in porous media within a rectangular enclosure has been studied numerically by Chang and Yang [71]. They showed that the temperature dependent density of the water was a significant contributor to the temperature field, flow field, and the position of solid-liquid interface. Beckermann and Viskanta [72] combined numerical and experimental studies for solid/liquid phase change in porous media with natural convection in the molten region. Their model was based on volume averaged transport equations, while phase change

was assumed to occur over a small temperature range. Experiments were performed in a vertical, square enclosure using gallium and glass beads as the PCM and the porous matrix respectively. They showed that natural convection as well as the conduction in the solid has a considerable influence on the interface shape during both melting and solidification processes. All these works considered local thermal equilibrium between the solid matrix and the PCM, and this was acceptable because in most of the cases they were dealing with low thermal conductivity porous matrices. Harris et al. [73] introduced a linearized enthalpy model that maintains a temperature difference between the PCM and the walls of the pore while it accepted a standard analytical solution technique. Due to the very high difference between the thermal properties of the PCM and the porous matrix in the current application, the thermal equilibrium between the PCM phase and the solid matrix phase will not occur.

Most of the researches that considered local thermal non-equilibrium dealt with heat conduction and convection without phase change processes. One of the earliest studies for convection heat transfer in a packed bed considering local thermal non-equilibrium was carried out by Vafi, et al. [74,75]. They presented an analysis for the forced convective flow of a gas or liquid through a packed bed of spherical solid particles. Recently Calmidi et al. [76] and Phanikumar et al. [77] studied natural and forced convection inside high porosity metal foam using a two-energy equation model. It was shown that the deviation from local thermal equilibrium became significant for high values of Darcy and Rayleigh numbers. For conduction heat transfer in porous media, Whitaker [78] carried out an

extensive analysis to determine the conditions for local thermal equilibrium. He concluded that the deviation from local thermal equilibrium would be significant if there is a large difference between the physical properties of the fluid and solid phase. By applying local thermal non-equilibrium, some parameters are needed to close up the model. These parameters are the effective thermal conductivity for the two phases, the interfacial heat transfer coefficient, and the interfacial surface area.

To define the interfacial heat transfer coefficient, Kuwahara [79] solved the microscopic flow at pore scale for two-dimensional porous structure. He defined the interfacial heat transfer coefficient, effective thermal conductivity, and fluid dispersion in convection heat transfer in porous media. The flow was assumed to pass through a collection of square rods placed regularly in an infinite space. In conduction heat transfer in porous media, defining the interfacial heat transfer coefficient is a rigorous task. Quintard and Whitaker [80] developed closure problems to model the conduction heat transfer in porous media. These closure problems are solved numerically for certain geometries such as stratified systems and uniform arrays of cylinders to get the transport coefficients. Hsu [81] derived a simple correlation to define the Nusselt number considering the porous media consists of dispersed spheres immersed in a stagnant fluid.

2.2.5 PCM in energy storage and cooling applications

Currently, electronic devices experience high and fluctuating heat generation rates. Many multi-chip modules and sensors are either operated irregularly or they have variable power. As a consequence, the cooling system

must be designed for the peak power operation otherwise another system should be incorporated to accommodate the power variation during the transient operation conditions. The design of a cooling system for such devices became a very big challenge. Different designs of active cooling have been used utilizing micro-channels and finned high thermal conductivity foams.

A detailed numerical simulation of forced convection heat transfer occurring in silicon-based micro-channel heat sinks was conducted by Li et al. [82] using a simplified 2D fluid flow and 3D heat transfer numerical model. In this study, they showed the effect of changing the geometric parameters and the thermo-physical properties of the cooling fluid on the performance of the micro-channel heat sink. Bhattacharya and Mahajan [83] investigated experimentally forced convective heat transfer in novel finned metal foam sinks. Their experiments were carried out on aluminum foams of 90% porosity and pore sizes corresponding to 5PPI and 20 PPI where PPI stands for pore per inch. Different configurations of fins were used. The results showed that the heat transfer was significantly enhanced when fins were incorporated in metal foam. The heat transfer coefficient increased with increasing the number of fins until adding more fins retarded the heat transfer due to interference of thermal boundary layers. These kinds of designs for active cooling will work effectively for steady state operations, but for transient operations the temperature may jump above the maximum allowed temperature which is assigned to achieve efficient performance.

Solid-liquid phase change has been used in a wide range of applications of energy storage [84]. Besides that, PCMs seems also to be a good choice for use in passive cooling of electronic devices. The latent heat of fusion, which is usually higher than the sensible heat adds an extra heat capacity to the cooling system. Also, the fluctuations of the generated power could be converted into oscillations in the solid-liquid interface without significant fluctuations in the electronic device temperature. PCM thermal energy storage could be used, where during the peak the excess power will be stored as a latent heat and released during the periods of low power operation.

Some analytical studies have been carried out to investigate the potential use of PCM in the cooling applications of high power electronics. Lu [85] studied analytically, using PCM in the cooling of high power electronics. He emphasized on minimizing the rise of junction temperatures due to the thermal transient effect. His analytical model was a one dimensional finite slab of PCM exposed suddenly to a uniform heat flux at the top surface and cooled by convective air at the bottom. Through the analytical solution, the time domain has been partitioned into two regimes separated by the time needed for the thermal front to transverse across the whole slab. Chakraborty and Dutta [86] also developed an analytical heat transfer model, which was capable of analyzing cyclic melting and solidification processes of a PCM used in the context of an electronic cooling system. In their model, they analyzed the heat transfer for a number of temporal regimes. The analytical solution that was carried out in each regime was formulated either using semi-infinity consideration, or employing a method of

quasi-steady state, depending on the applicability. The disadvantage of using such analytical techniques is that it is limited to simple configurations and boundary conditions. Also, these models are mainly based on pure conduction. To include the convection motion of the liquid phase, the analytical solution will be very difficult if not impossible.

The feasibility of using metallic solid-liquid PCM in periodic power dissipating devices has been studied by Siva et al. [87]. The PCM is enclosed inside micro-channels with semiconductor devices. Both numerical and experimental investigations have been carried out. They noticed that PCMs perform well at lower power levels for silicon carbide semiconductor devices, but the use of high thermal conductivity spreaders such as diamond becomes mandatory at higher power levels. They mentioned that temperature reductions up to 25 °C can be achieved with a combination of a high thermal conductivity heat spreader and PCM. A thermal analysis was performed for a package design relevant to power electronics by Evans et al. [88]. They tried to derive a straightforward expression to relate the materials used and their physical dimensions to the power input and the junction temperature for both steady-state operating conditions and for pulses. The role of PCM in suppressing temperature elevations during pulses was evident.

For mobile electronic devices, PCMs appear to be a good choice to extend the operational periods. Marc et al. [89] studied the feasibility of transient thermal management of handsets using PCMs experimentally. In their experiments, they used an ABS handset mock-up. They measured the

temperature field of the handset case at selected intervals of time using an infrared camera while thermocouples were used to measure the temperatures of the PCM. It was concluded that using PCMs can very substantially increase the time of service for the handset. For example, they mentioned that for 3 Watts of power supplied to the handset, the presence of about 10 gm of PCM allowed for three to five times longer use before the handset case temperature became unbearable. Tan and Tso [90] studied experimentally cooling electronic devices, such as personal digital assistants and wearable computers, using a heat storage unit filled with PCM of n-eicosane inside the device. They noticed that using PCM maintains the chip temperature below the allowable service temperature for 2 hours of transient operation. The heat dissipation of the chip and the orientation of the heat storage unit was investigated. It was found that different orientations of the heat storage unit could affect significantly the temperature distribution.

PCMs also have been used to reduce the temperature of photovoltaic devices to increase their efficiency. Huang et al. [91] studied the use of PCMs to moderate building integrated photovoltaic temperature rises experimentally and numerically. The numerical model was a 2-D finite volume heat transfer conjugated hydrodynamically to solve the Navier-Stokes and energy equations. The experimental data was used to validate the numerical model. Two different configurations were used, one with internal fins and one without. The predicted temperature distributions for different insolation and ambient temperatures at the photovoltaic surface showed that the moderation of temperature achieved can

lead to significant improvements in the operational efficiency of photovoltaic facades.

Natural convection motion, which occurs due to buoyancy forces in the molten liquid has been found to have a considerable effect on the performance. It enhances the heat transfer process, but at the same time, it makes the performance dependent on the orientation of the electronic device. In the devices, which need a high degree of mobility, solid-solid PCM or use of immobilization to prevent the liquid phase motion could be used. Writz, R.A. et al. [92] used hybrid coolers consisting of aluminum plate-fins and solid-solid PCM for temperature stabilization of electronic modules having time dependent heat dissipation rates. In their model, they considered that the module could be viewed as thermally connected volumes with each volume having a specific functionality. The used solid-solid PCM is called Temperature Control Compound (TCC), which is a one of organic solid solutions. The material is a waxy granulate that is plastic in its high temperature phase. The particle size ranges from 0.1 mm to 1 mm. Their numerical simulations showed that an efficient hybrid cooler should have a high PCM conductance and small transition temperature interval in order to provide tight thermal control. The PCM conductance can be maximized by proper incorporation of metallization into the storage volume. To immobilize the solid-liquid PCM during its melting process, Wrtiz et al. [93] developed a novel lamination consisting of aluminum heat spreader plates interspersed with a polymer-based thermal energy storage composite. The composite consisted of a thermoplastic matrix that encapsulated paraffin such that it was immobilized in

liquid phase. Composites with paraffin mass fractions as high as 80% have been formulated.

Different types of PCMs have been utilized such as metallic and organic PCMs. Metallic PCMs have the advantage of having high thermal conductivity, but at the same time suffer from having higher densities which add more weight to the system. On the other hand, organic PCMs have high latent heat and lower densities but suffer from having very low thermal conductivity. The lower thermal conductivity of the organic PCM causes the temperature of hot surfaces to shoot up directly after the melting interface moves away from the surface. Pal and Joshi [94] developed a computational model to predict the performance of PCMs for passive thermal control of electronic modules during power variations or following an active cooling system failure. Two different ways to incorporate the PCM in the module were considered. One was to place a laminate between the substrate and cold plate, and the other was to place a laminate of PCM outside the chip module. They used two different types of PCMs, one was organic paraffin, and the other was eutectic alloy of Bi/Pb/Sn/In. They concluded that organic PCMs have higher latent heat per unit mass but their low thermal conductivity causes a higher steady state temperature of the module. On the other hand, they mentioned that metallic PCMs in the primary heat flow path prove to be a better choice due to their high thermal conductivity and high latent heat per unit volume.

Masaru [95] studied the performance of metallic alloy PCM to control the operational time of high density electronic packaging using a thermal network

method. The thermal experiments using this alloy confirmed that the substrate back surface temperature could be kept constant at the melting temperature of the PCM for several minutes by thermal absorption, while the PCM phase changed from solid to liquid state. Also, in his study he confirmed that the thermal network method is practical for the thermal design of packages with PCM. Shankar and Suresh [96] studied numerically the melting of PCM in a container with multiple discrete heat sources mounted on one side for electronic cooling by latent heat energy storage. Their study focused on the thermal management issues that arise when electronic components experience sudden surges in power dissipation. The analysis was performed under different pulse frequencies, different aspect ratio for the energy storage, as well as different locations for the heat sources. They characterized their system based on the rate of heat absorption and the maximum temperature experienced at the heater sources. They mentioned that the heat source location and the container aspect ratio play very significant roles in the performance of the PCM energy storage unit. They showed that locating the heat sources on the bottom wall had the best thermal performance with a higher rate of heat absorption and lower maximum temperatures. Shankar and Suresh [97] also investigated numerically the thermal control of power semi-conductors using PCMs and compared the performance to the performance of a copper heat sink. They used different types of PCMs, organic and metallic. Simple expressions for the melt depth, melt time, and temperature distribution were presented in terms of the dimensions of the heat sink and the thermo-physical properties of the PCM. They showed that the use of

organic PCMs without thermal conductivity enhancers is a poor choice due to its low thermal conductivity. The performance of the metallic PCMs and organic PCMs with thermal conductivity enhancers could be comparable with each other depending on the thermal conductivity of the enhancer.

2.2.6 Effect of surface characteristics during phase change

Using high thermal conductivity porous matrices to enhance heat transfer processes inside low thermal conductivity PCM systems is found to be an effective technique. This is because heat diffuses faster in the solid matrix and this heat is exchanged effectively with the PCM phase due to the higher interfacial surface area between the two phases. In other words, the porous matrix will play as a heat carrier to the PCM phase. The effectiveness of the heat exchange between the two phases depends on how good the contact is between the two phases. As mentioned by Writz et al. [92,93], an efficient hybrid heat storage or cooler should have a high PCM conductance between the two phases. The degree of contact or thermal conductance could be enhanced by increasing the interfacial surface area or by increasing the wettability (surface energy) between the solid matrix and the PCM phase.

Defining thermal conductance between two adjacent phases of a composite material is a difficult task. Some of the researches in this field have studied the thermal conductance between the mould and liquid metal during the solidification process. Assar [98] studied the influence of the mould inner surface roughness on the interfacial heat transfer coefficient (IHTC). The value of the IHTC was defined by comparing experimental data and numerical simulation for

the solidification process of zinc inside steel moulds with different surface roughness. It was found that the IHTC decreases as the mould surface roughness increases due to formation of air gaps between the mould and the molten liquid. Experimental work has been done by Loulou et al. [99] to study the transient heat transfer in the early stages of solidification of some pure metals on water-cooled substrates. Their experiments were performed to measure the thermal contact resistance during solidification of tin, lead, and zinc dropped on Nickel substrate. They showed that the surface tension, contact angle, and surface roughness have the biggest effect on the interfacial heat transfer coefficient. Taha et al. [100] mentioned that several factors interact to determine the value of IHTC between the casting and the mould surface. These factors are, the type of metal, the mould material surface conditions, the mould and pouring temperatures, and the type of gases at the interfacial gap formed. Narayan K. et al. [101] also estimated the IHTC during unidirectional solidification of a cast iron alloy against a sand block. They showed that the IHTC is a function of the surface roughness, characteristics of the casting, and the sand surface. Wang and Matthys [102] evaluated the IHTC between molten splat and a substrate by matching numerical model calculations with the top splat surface temperature history measured by a fast-response pyrometer. They showed that the value of the IHTC is affected by the surface conditions: the smoother the surface, the better the thermal contact and the higher value of the IHTC.

In heat transfer applications, especially in electronic devices, the contact resistance between the electronic chip and the substrate can lead to a high

temperature rise in the electronic chip. The contact could be increased by using thermal interface material. To study the effect of the contact surface shape, Syed [103] performed a numerical analysis to study contact heat transfer through a constriction of a frustum shape in a gaseous environment. The results showed that the gas gap thermal conductance is a significant parameter of the cone angle of the frustum. Prasher et al. [104] studied the performance of a particle laden polymer as a thermal interface material. They mentioned that the thermal resistance is not only a function of thermal conductivity but it also depends on the bond line thickness (BLT) of the interface material. They introduced a rheology based semi-empirical model for the prediction of the BLT as a function of yield stress of the interface material and the applied pressure. Prasher [105] developed an analytical model for the thermal contact resistance of liquid interface materials. In his model, the thermal resistance is set as a function of surface tension, contact angle, thermal conductivity, roughness, and pressure. The results of this analytical model matched the experimental data.

2.3 Work Statement

Due to the high value of the latent heat and the isothermal nature of the phase change process, using PCMs in the applications of energy storage, thermal protection, and cooling seems to be superior. In these applications, it is important to absorb/reject a certain amount of heat in a certain time, especially for the systems which are restricted to certain periodic heat fluxes. While absorbing or rejecting heat, the solid-liquid interface moves away from the

surface from which the energy is absorbed or rejected. Therefore, the surface temperature will diverge from the phase change temperature rapidly if the utilized PCM has low thermal conductivity. Due to the low thermal conductivity of most of the available PCMs, it is necessary to look for some ways to enhance the thermal conductivity of these materials to be able to achieve the required heat transfer rates. The heat transfer enhancement required for melting or solidification depends on the type of application. Some applications require heat to be charged at a faster rate while others require heat to be discharged at a faster rate. Most of the applications nowadays such as storing energy, thermal protection in space applications, and cooling of electronic devices require high heat transfer rates.

Adding high thermal conductivity additives such as metal fins or carbon fibers is not so effective because of the random alignment and the missing of connectivity between the constituents of the high thermal conductivity phase. Using high thermal conductivity porous foams such as metal foam or graphite foam seems to be more effective.

It was obvious from the literature review that phase change processes (melting and solidification) inside high thermal conductivity porous media did not receive extensive research. All the researches which have been conducted in this field, are concentrated on heat conduction in multiphase systems and free and forced convection in porous media. Melting and solidification of PCM inside packed beds has been studied using simple models based on the assumption of local thermal equilibrium. This can be accepted when the thermal properties of the two phases are close to one another. At the same time, all of the researches

that have been carried out to enhance the thermal conductivity of the PCMs by addition of some kind of high thermal conductivity additives or porous structures are mainly experimental. They mainly concentrated on testing the enhancement in the effective thermal conductivity of the composite. They did not take the phase change process and the molten liquid flow motion into consideration. In addition, they did not study the parameters that affect the performance of such composites in thermal management applications.

The second point of interest we are planning to focus on, deals with a new composite structure of the foam and PCM using a local thermal non-equilibrium approach. This could be considered a mandatory assumption because, as we mentioned earlier, there is a big difference between the thermal properties of the two phases. Consequently, the heat will diffuse faster in the solid phase while the diffusion will be very slow in the PCM phase. Moreover, the melting interface will generate a barrier for heat diffusion inside the PCM phase. Due to this temperature difference between the solid and the PCM phase, there will be a significant local heat exchange between the two phases, which will have a significant effect on the performance of the porous composite. The effectiveness of the heat exchange between the two phases will depend on how good the contact is between the two phases. The contact between the two phases can be enhanced by increasing the interfacial surface area or by increasing the wettability between the solid matrix and the PCM. This can be achieved by surface alteration of the porous foam either by etching (creating roughness) or by

chemically adding some surface functional groups on the foam surface to increase the dispersive surface energy.

2.4 Goals and objectives

Our objective in this research is to study the phenomenon of phase change processes of PCM infiltrated high thermal conductivity porous foams. First, we will study the process from the macro-scale point of view using a volume-averaging technique. This study will include heat conduction and convection with phase changes inside open cell foams considering the local thermal non-equilibrium between the two phases. Through this step we will need to define some parameters which depend on the foam microstructure such as the effective thermal conductivity, permeability, and the interfacial heat transfer coefficient between the two phases. Simple analytical models will be developed to correlate these parameters with the foam pore structure.

We are planning to tackle this problem numerically and experimentally. Regarding the numerical part, a numerical model based on solving the volume averaged conservation equations of mass, momentum, and energy with phase change in the porous media will be developed. A finite difference technique based on control volume approach with a non-staggered curvilinear body fitted grid will be used in dealing with regular or irregular geometries. Energy transport in this system will be studied using a two-equation model, which will be able to consider the local thermal non-equilibrium condition. The natural convection motion of molten liquid PCM inside the porous matrix will be studied considering Darcy, Brinkmann, and Forchheimer effects. A mathematical model for predicting

effective thermal conductivity of the foam material will be developed based on a 1-D heat conduction approximation through the foam ligaments. The interfacial heat transfer coefficient will be correlated to the foam surface energy through the application of a simple wettability model.

Besides the modeling effort, an experimental setup will be built to validate the numerical work. A regular porous matrix such as high porosity open cell Aluminum foam, and high thermal conductivity carbon foam will be used. Low melting temperature PCM will be tested in this experimental analysis. After validating the numerical model with the experiments, a comprehensive parametric study will be carried out to define the system parameters that can achieve optimum performance of this system as a heat storage or heat sink. The parametric study will include studying the effect of changing both the foam and the PCM properties. Regarding foam, the effect of changing porosity, pore size, surface energy, and effective thermal conductivity will be studied. For PCM, we will check the effect of changing the melting point, liquid phase viscosity, and the latent heat of fusion on the system performance.

CHAPTER 3

MATHEMATICAL AND NUMERICAL MODEL

3.1 Introduction

Melting and solidification of PCMs inside high thermal conductivity porous matrices includes many intricate phenomena. Three phases exist beside each other, namely the solid phase of the porous matrix beside the liquid and solid phases of the PCM. Moreover, a moving interface may exist between the solid and liquid phase of the PCM. In the regions where the solid PCM phase exists, the problem is governed by conduction heat transfer in a multiphase system. When the PCM changes to liquid, the problem is governed by conduction/convection heat transfer inside porous media. In addition, the system is expected to be in local thermal non-equilibrium due to the large difference between the PCM and foam thermal properties.

In this chapter, a mathematical model based on the application of the conservation of mass, momentum, and energy principles was developed. The governing equations are set in 2-D curvilinear coordinates. The important non-dimensional parameters are defined by non-dimensionalizing the governing equations. The numerical treatment and implementation with the goal to develop a robust numerical code that can be used to solve problems of

conduction/convection heat transfer with phase change inside porous media have been explained. Finally, the numerical model is validated with some documented published data.

3.2 Mathematical Modeling

3.2.1 Volume averaging technique

The complexity associated with the geometric structure of porous medium does not allow treatment of the detailed temperature and velocity fields inside each individual porous structure. Thus, it is a common practice to smooth out the local complexity of the actual phenomena, and concentrate on the overall aspects of mass, momentum, and energy conservation principles. This is done by applying a volume-averaging technique. The process of volume averaging depends on integrating the microscopic conservation equations of mass, momentum, and energy over a Representative Elementary Volume (REV), which contains both the solid and fluid phases of the porous media. The REV should have a good representation of the porous system. It should be larger than the pore size and very small compared to the system length scale.

It is necessary to make use of two different averages of any quantity; these are the local volume average and the intrinsic phase average. The local volume average for any quantity ϕ associated with phase f is defined as,

$$\langle \phi \rangle = \frac{1}{V} \int_{V_f} \phi dV, \text{ where } V_f \text{ and } V \text{ are the volumes of the } f \text{ phase inside the REV}$$

and the total volume of the REV respectively. The intrinsic phase average is defined as,

$$\langle \phi \rangle^f = \frac{1}{V_f} \int \phi dV \text{ and } \langle \phi \rangle^f = \langle \phi \rangle / \delta, \text{ where } \delta \text{ is the porosity of the porous media.}$$

The microscopic conservation equations can be volume averaged using these definitions for the averages and by applying the following averaging rules:

1- The average of a product of two variables a and b

$$\langle ab \rangle = \frac{1}{\delta} \langle a \rangle \langle b \rangle + \langle a'b' \rangle \text{ where } a' = a - \langle a \rangle^f$$

2- The average of the gradient of any variable a

$$\langle \nabla a \rangle = \nabla \langle a \rangle + \frac{1}{V} \int a dA_{int}$$

where the integration is over the interfacial area between the two phases.

For example, upon volume averaging the microscopic momentum equation ($\frac{\partial \rho u}{\partial t} + \nabla \cdot \rho u u = -\nabla p + \rho g + \nabla \cdot \tau$) over the REV, the volume averaged momentum equation will take the following form:

$$\frac{1}{\delta} \frac{\partial \rho \langle u \rangle}{\partial t} + \frac{1}{\delta^2} \nabla \cdot \rho \langle u \rangle \langle u \rangle = -\nabla \langle p \rangle + \rho g + \frac{\mu}{\delta} \nabla^2 \langle u \rangle + S \quad (3.1)$$

$$\text{where } S = \frac{1}{V_f} \int (\tau_{ij} dA_j - p dA_i) - \frac{\rho}{\delta} \frac{\partial}{\partial x_j} \langle u_i' u_j' \rangle.$$

The first term in S represents the total surface force acting on the fluid inside the microstructure of the porous media while the second term represents the inertial dispersion due to the creation of small eddies within the

microstructure. Vafai and Tien [106] corresponded these two terms to the empirical Forchheimer-extended Darcy law as,

$$S = -\frac{\mu}{K}\langle u \rangle - \frac{\rho C}{\sqrt{K}}|\langle u \rangle|\langle u \rangle. \quad (3.2)$$

It is obvious here that the volume averaging process converted the porous media into a multiphase domain in which each phase is assumed to behave as a continuum with specific physical properties that fills the entire domain. The different phases of the porous media may interact with each other by exchanging mass, momentum, and energy. It is shown that the volume averaged momentum equation takes the same form as the microscopic equation with a new value of viscosity, μ/δ , and with added source terms. These source terms represent the momentum exchange between different phases of the porous media through the interfacial area. The volume averaged energy equation of any phase of the porous media will also take the same form as the microscopic energy equation with a modified value for the thermal conductivity, which is known as the effective thermal conductivity, and with an added source term, which represents the heat exchange between the solid and fluid phases of the porous media.

3.2.2 Local thermal equilibrium

The volume averaged energy equations for the fluid and solid phase have the following form:

Fluid phase

$$\delta(\rho c_p)_f \frac{\partial \langle T_f \rangle^f}{\partial t} + \nabla \cdot (\rho c_p)_f \langle u \rangle \langle T_f \rangle^f = \nabla \cdot (k_{feff} \nabla \langle T_f \rangle^f) + h_{sf} a_{sf} (\langle T_s \rangle^f - \langle T_f \rangle^f) \quad (3.3)$$

Solid phase

$$(1 - \delta)(\rho c)_s \frac{\partial \langle T_s \rangle^f}{\partial t} = \nabla \cdot (k_{seff} \nabla \langle T_s \rangle^f) - h_{sf} a_{sf} (\langle T_s \rangle^f - \langle T_f \rangle^f) \quad (3.4)$$

where, k_{seff} and k_{feff} are the effective thermal conductivities of the solid and fluid phases, and the subscripts s and f refer to the solid and fluid phases respectively. The last term on the right of equations (3.3 and 3.4), represents the interfacial heat exchange between the two phases, where h_{sf} is the interfacial heat transfer coefficient and a_{sf} is the interfacial surface area.

Local thermal equilibrium can be assumed if the solid and fluid phase temperatures are very close to each other. In this case, a single value of temperature, $\langle T_f \rangle^f \approx \langle T_s \rangle^f \approx \langle T \rangle$, could be used to represent the local temperature inside the porous media and the two equations can be added together to give a general energy equation.

$$(\delta(\rho c_p)_f + (1 - \delta)(\rho c_p)_s) \frac{\partial \langle T \rangle}{\partial t} + \nabla \cdot (\rho c_p)_f \langle u \rangle \langle T_f \rangle = \nabla \cdot (k_{feff} + k_{seff}) \nabla \langle T \rangle \quad (3.5)$$

The local thermal equilibrium condition can only be achieved when one of these conditions occurs:

- 1- Either of the two phase's porosity is very small and tends to zero

- 2- The difference between the thermal properties of two phases is negligible
- 3- The ratio of $(k_{eff} / a_{sf} h_{sf})$ is very small compared to the square of the problem length scale. This condition means that the ability of the system to conduct heat is very small compared to the heat exchange between the two phases.

In our case, we are dealing with high thermal conductivity foam impregnated with low thermal conductivity PCM to cool or to absorb heat from a surface subjected to high heat flux. Therefore, it is expected that our case will be far from a local thermal equilibrium condition.

3.2.3 Governing equations in 2-D general coordinates

It is more convenient to write and solve the governing equations in generalized, non-orthogonal, curvilinear coordinates, especially when complex geometries are involved. Furthermore, in many applications it may be desirable to preferentially improve resolution in certain regions of the domain. Then, the grid is required either to adapt by moving it during the solution or by concentrating the grid at the expected high gradient regions which will make the grid irregular. The governing equations are transformed into 2-D general coordinates by making coordinate transformations from the regular (x-y) coordinate to the general coordinate system (ξ, η) .

The final formulation for the governing equations is set in a manner such that physical properties of both porous media and PCM could be constant or varying with temperature. The porosity is considered spatially constant.

Furthermore, the following assumptions have been considered in the mathematical model:

- 1- The molten phase of the PCM is a Newtonian fluid
- 2- The liquid phase motion is laminar and the viscous dissipation is negligible
- 3- Boussinesq approximation is applicable
- 4- Volume change due to phase change process is negligible

Considering 2-D configuration, the physical domain (x,y) could be transformed into a computational domain (ξ,η).

$$x = x(\xi, \eta) \text{ and } y = y(\xi, \eta)$$

The mathematical formulation of the governing equations in a non-orthogonal curvilinear system can be written as follows:

$$\textbf{Continuity} \quad \frac{\partial}{\partial t}(\rho J) + \frac{\partial}{\partial \xi}(\rho U) + \frac{\partial}{\partial \eta}(\rho V) = 0 \quad (3.6)$$

u-momentum

$$\begin{aligned} \frac{J}{\epsilon} \frac{\partial \rho u}{\partial t} + \frac{1}{\epsilon^2} \frac{\partial \rho U u}{\partial \xi} + \frac{1}{\epsilon^2} \frac{\partial \rho V u}{\partial \eta} = & -y_\eta \frac{\partial p}{\partial \xi} + y_\xi \frac{\partial p}{\partial \eta} + \frac{\partial}{\partial \xi} \left[\frac{\mu}{J\epsilon} \left(a_{11} \frac{\partial u}{\partial \xi} - a_{12} \frac{\partial u}{\partial \eta} \right) \right] \\ & + \frac{\partial}{\partial \eta} \left[\frac{\mu}{J\epsilon} \left(-a_{12} \frac{\partial u}{\partial \xi} + a_{22} \frac{\partial u}{\partial \eta} \right) \right] + S_u(\xi, \eta) J \end{aligned} \quad (3.7)$$

v-momentum

$$\begin{aligned} \frac{J}{\epsilon} \frac{\partial \rho v}{\partial t} + \frac{1}{\epsilon^2} \frac{\partial \rho U v}{\partial \xi} + \frac{1}{\epsilon^2} \frac{\partial \rho V v}{\partial \eta} = & -x_\xi \frac{\partial p}{\partial \eta} + x_\eta \frac{\partial p}{\partial \xi} + \frac{\partial}{\partial \xi} \left[\frac{\mu}{J\epsilon} \left(a_{11} \frac{\partial v}{\partial \xi} - a_{12} \frac{\partial v}{\partial \eta} \right) \right] \\ & + \frac{\partial}{\partial \eta} \left[\frac{\mu}{J\epsilon} \left(-a_{12} \frac{\partial v}{\partial \xi} + a_{22} \frac{\partial v}{\partial \eta} \right) \right] + S_v(\xi, \eta) J \end{aligned} \quad (3.8)$$

PCM phase energy equation

$$J\delta \frac{\partial \rho c_{pf} T_f}{\partial t} + \frac{\partial \rho c_{pf} U T_f}{\partial \xi} + \frac{\partial \rho c_{pf} V T_f}{\partial \eta} = \frac{\partial}{\partial \xi} \left[\frac{k_{feff}}{J} \left(a_{11} \frac{\partial T_f}{\partial \xi} - a_{12} \frac{\partial T_f}{\partial \eta} \right) \right] + \frac{\partial}{\partial \eta} \left[\frac{k_{feff}}{J} \left(-a_{12} \frac{\partial T_f}{\partial \xi} + a_{22} \frac{\partial T_f}{\partial \eta} \right) \right] + S_{T_f}(\xi, \eta)J \quad (3.9)$$

Solid matrix energy equation

$$J(1-\delta) \frac{\partial \rho c_{ps} T_s}{\partial t} = \frac{\partial}{\partial \xi} \left[\frac{k_{seff}}{J} \left(a_{11} \frac{\partial T_s}{\partial \xi} - a_{12} \frac{\partial T_s}{\partial \eta} \right) \right] + \frac{\partial}{\partial \eta} \left[\frac{k_{seff}}{J} \left(-a_{12} \frac{\partial T_s}{\partial \xi} + a_{22} \frac{\partial T_s}{\partial \eta} \right) \right] + S_{T_s}(\xi, \eta)J \quad (3.10)$$

where, δ is the solid matrix porosity and ε is the liquid phase fraction. The value of ε is defined as the product of the PCM liquid fraction and the foam porosity.

The geometrical diffusion coefficients a_{11} , a_{12} , a_{21} , a_{22} and Jacobian J are given by,

$$a_{11} = \left(\frac{\partial x}{\partial \eta} \right)^2 + \left(\frac{\partial y}{\partial \eta} \right)^2, \quad a_{12} = \left(\frac{\partial x}{\partial \xi} \right) \left(\frac{\partial x}{\partial \eta} \right) + \left(\frac{\partial y}{\partial \xi} \right) \left(\frac{\partial y}{\partial \eta} \right), \quad a_{22} = \left(\frac{\partial x}{\partial \xi} \right)^2 + \left(\frac{\partial y}{\partial \xi} \right)^2$$

$$J = \left(\frac{\partial x}{\partial \xi} \right) \left(\frac{\partial y}{\partial \eta} \right) - \left(\frac{\partial x}{\partial \eta} \right) \left(\frac{\partial y}{\partial \xi} \right)$$

The contravariant velocity U and V are defined as,

$$U = u \frac{\partial y}{\partial \eta} - v \frac{\partial x}{\partial \eta} \quad \text{and} \quad V = v \frac{\partial x}{\partial \xi} - u \frac{\partial y}{\partial \xi}$$

A general form of momentum and energy equations can be written as,

$$J \frac{\partial \rho \phi}{\partial t} + \frac{\partial \rho U \phi}{\partial \xi} + \frac{\partial \rho V \phi}{\partial \eta} = \frac{\partial}{\partial \xi} \left[\frac{\Gamma_\phi}{J} \left(a_{11} \frac{\partial \phi}{\partial \xi} - a_{12} \frac{\partial \phi}{\partial \eta} \right) \right] + \frac{\partial}{\partial \eta} \left[\frac{\Gamma_\phi}{J} \left(-a_{12} \frac{\partial \phi}{\partial \xi} + a_{22} \frac{\partial \phi}{\partial \eta} \right) \right] + S_\phi J \quad (3.11)$$

where ϕ could be u , v , T_s , and T_f . Γ_ϕ is the modified viscosity when ϕ represents u or v and k_{eff}/c_p when ϕ represents T_f and T_s . The source term S_ϕ that appears in the previous equation can be expressed for all the variables as shown in the following table (1).

Table (3.1) Source term definition

S_u	S_v	S_{Tf}	S_{Ts}
$-\frac{\mu}{K}u - \frac{\rho C \vec{u} u}{\sqrt{K}}$	$-\frac{\mu}{K}v - \frac{\rho C \vec{u} v}{\sqrt{K}} + \rho g \beta_f (T_f - T_{ref})$	$h_{sf} a_{sf} (T_s - T_f) - \delta \rho L \frac{df_l}{dt}$	$h_{sf} a_{sf} (T_f - T_s)$

The first term appearing in the momentum source terms in the u and v directions is the Darcy effect where K is the permeability of the porous matrix. The second term represents the Forchhiemer effect, and C is an empirical constant. β_f is the fluid thermal expansion coefficient and g is the acceleration of gravity. The first term appearing in the energy source terms S_{Tf} and S_{Ts} represents the heat exchange between the solid matrix and PCM phase. The second term in S_{Tf} represents the melting source term where f_l and L are the liquid fraction and latent heat of fusion of the PCM respectively.

3.2.4 Important non-dimensional parameters

Numerical study of fluid flow and heat transfer involves several coupled equations, at least, continuity, momentum and energy. Owing to the presence of many parameters, it is judicious to non-dimensionalize these equations. The non-dimensionalization makes the equations simpler, and it greatly simplifies the parametric study and the analysis of the problem. In this section, we will put the

conservation equations for phase change heat transfer inside porous media (using a two-energy equation model) in non-dimensional form to define the non-dimensional parameters that govern the physics involved in this heat transfer problem.

The physical dimensions are normalized by the selected length scale l . Since the liquid phase motion is mainly driven by buoyancy forces, the velocities will be normalized by the characteristic velocity $u^* = \alpha/l$, where α is the thermal diffusivity of the liquid phase of the PCM. The time is normalized by $t^* = l^2/\alpha$. The temperature should be normalized by a characteristic temperature difference. This temperature difference will depend on the boundary conditions of the problem. For example, if the problem is subjected to an isothermal boundary, the temperature could be normalized based on the temperature difference between the two isothermal surfaces ($T_H - T_C$). The non-dimensional averaged momentum and energy equations in vector form could be written as,

$$\frac{1}{\varepsilon} \frac{\partial \bar{u}^*}{\partial t^*} + \frac{1}{\varepsilon^2} \bar{u}^* \cdot (\nabla \bar{u}^*) = -\nabla p^* + \nabla \cdot \left(\frac{\text{Pr}}{\varepsilon} \nabla \bar{u}^* \right) - \left(\frac{\text{Pr}}{\text{Da}} + \frac{C}{\sqrt{\text{Da}}} |\bar{u}^*| \right) \bar{u}^* + \text{Ra Pr } \theta_f \hat{i}_g \quad (3.12)$$

$$\delta \frac{\partial \theta_f}{\partial t^*} + \bar{u}^* \cdot \nabla \theta_f = \nabla \cdot \left(\frac{k_{\text{feff}}}{k_f} \nabla \theta_f \right) - \delta \text{Ste} \frac{\partial f_l}{\partial t^*} + \text{Bi}(\theta_s - \theta_f) \quad (3.13)$$

$$(1 - \delta) \frac{\partial \theta_s}{\partial t^*} = \nabla \cdot \left(\frac{k_{\text{seff}}}{k_f} \frac{(\rho c_p)_f}{(\rho c_p)_s} \right) \nabla \theta_s - \text{Bi} \frac{(\rho c_p)_f}{(\rho c_p)_s} (\theta_s - \theta_f) \quad (3.14)$$

where Pr is the Prandtl number, Da is the Darcy number, Ra is the Rayleigh number, Ste is the Stefan number, and Bi is the Biot number. The definitions of these non-dimensional quantities are given in the nomenclature.

It is clear from these equations that the molten PCM flow could be related to the Prandtl number, Darcy number, and Rayleigh number. On the other hand, the heat transfer inside this system can be correlated with the Stefan number, Biot number, and the ratio of the PCM phase and the solid matrix phase thermal properties.

3.2.5 Modeling of effective thermal conductivity

The effective thermal conductivity of the foam depends on the thermal conductivity of the solid phase and the pore shape. It can be calculated analytically by assuming one-dimensional heat conduction through the porous media ligaments. The difficulty facing this technique is the complexity and the irregularity of the pore shape. For high porosity foams, like metal foams, the ligaments usually take regular shapes. Ligaments take the shape of regular hexagons with extra mass concentration at the nodes. For very high porosity metal foams, the concentrated mass at the nodes decreases and the foam can be approximated as interconnected fibers. The model used for calculating the effective thermal conductivity is based on dividing the unit cell into different layers such that in each layer, the void and solid phase should be parallel in conducting heat. The effective thermal conductivity of each layer is calculated based on the volume ratio between the void and the solid phase as,

$$k_i = \frac{V_{si}}{V_{Ti}} k_s + \frac{V_{vi}}{V_{Ti}} k_v .$$

where k_i is the thermal conductivity of the i th layer and V_s , V_v , and V_T are the solid, void, and total volumes respectively. Then, the total effective thermal conductivity of the unit cell is calculated by combining all the layers together in series.

$$\frac{\sum L_i}{k_e} = \sum \frac{L_i}{k_i}$$

where L_i is the length of each layer in the heat transfer direction.

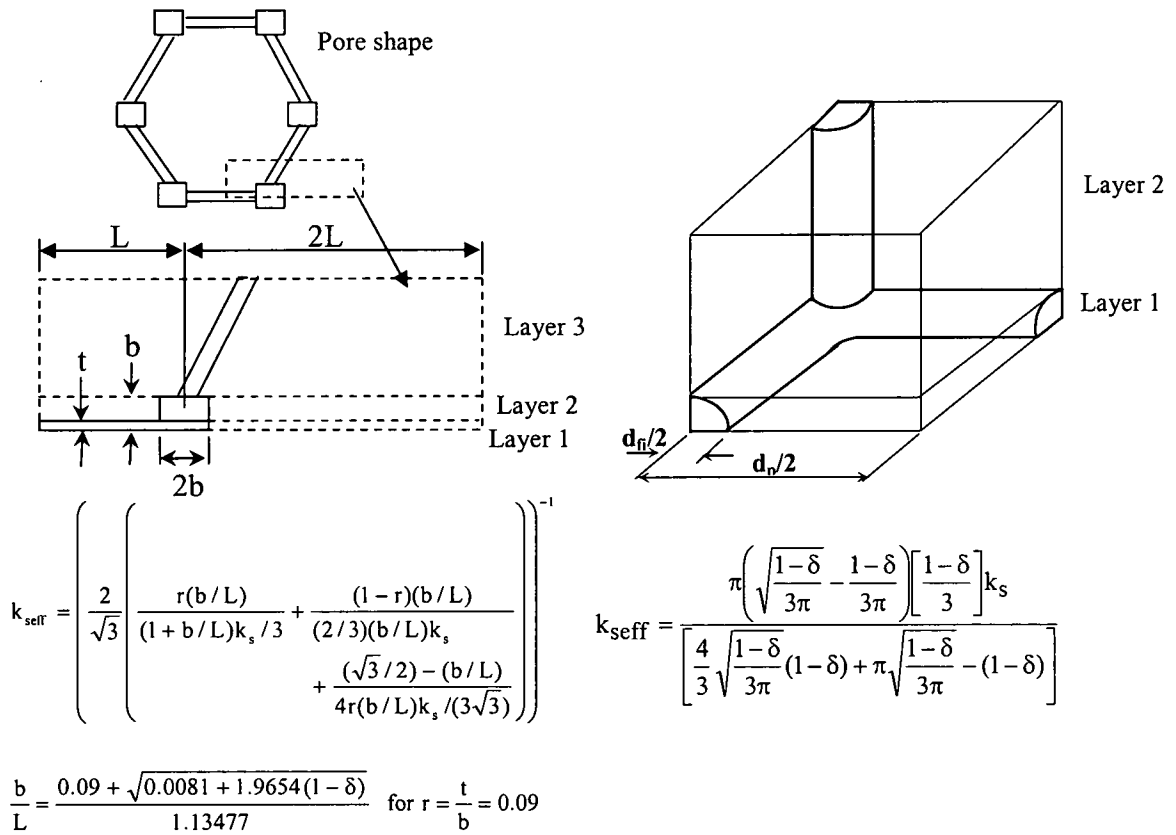


Fig. (3.1) 2-D hexagonal pore and 3-D interconnected fiber models

Two foam structures were examined, one for 2-D hexagonal structure and the other for 3-D interconnected fibers as shown in Fig. (3.1). The results for both of the two models agreed with the measurements for high porosity foam, but it over-estimated the thermal conductivity for low porosity foams because of the increase in mass concentration at the fiber intersections, as shown in Fig. (3.2).

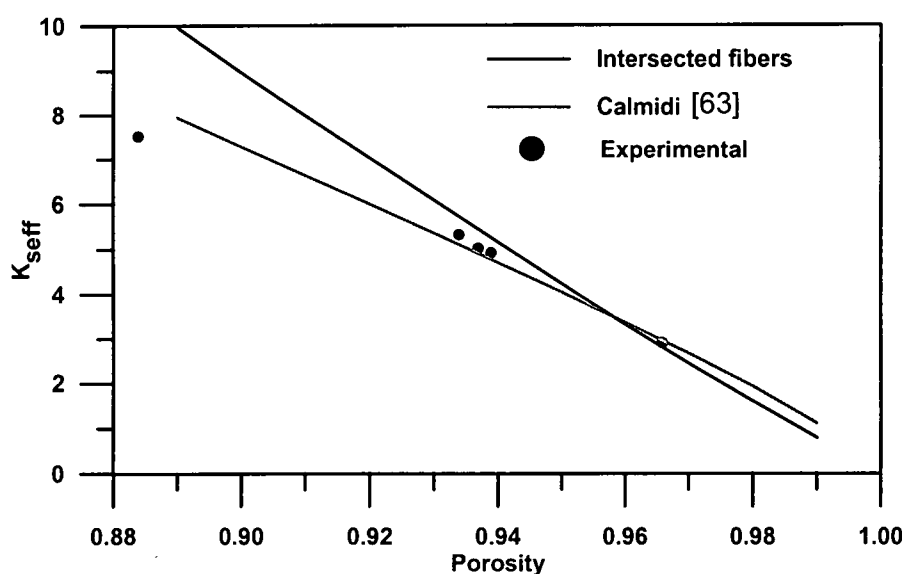


Fig. (3.2) Foam effective thermal conductivity versus porosity

3.2.6 Modeling of Carbon Foam Wettability

Infiltrating PCMs inside the pores of the foam depends on the pore size and the surface energy of the liquid phase of the PCM and the foam material. Since the surface energy of Aluminum is high compared to the molten wax, and the pore size of the aluminum foam is relatively high, the infiltration process is easy and the wax will completely wet the foam surface. On the other hand, carbon foam pore size is very small and the surface energy of the untreated

carbon is too low compared to the molten PCM surface energy. For this reason, during the infiltration process, some air gaps or pockets are expected to form between the PCM and the pore surface. This causes thermal resistance between the high thermal conductivity phase, the foam solid phase, and the PCM phase. At the same time, low wettability will reduce the amount of infiltrated PCM which affects the overall heat capacity of the system.

The size and shape of these air-trapped pockets is expected to depend on the pore shape and the PCM-carbon wettability. The pore structure of the open cell carbon foam consists of interconnected ligaments which form the pores. In the ligament planes, there are holes connecting the pores with each other. These holes are created when two adjacent bubbles intersect during the foaming process. According to the optical pictures of carbon foam, each pore could be approximated as a hexagon as shown in Fig. (3.3). The corners of the pores will be the most probable spaces to entrap air, so we assumed that some air pockets will be formed in these corners and the surface tension force will try to push the PCM inside the corner against the trapped air pressure. The corner region is approximated as a conical shape with an angle ranging between 90-120 degrees, and the open region in the ligament is assumed to be 1/3 of the ligament length as shown from Fig. (3.4).

The capillary pressure, which is the difference between the pressure in the liquid PCM and the air gap pressure can be defined as,

$$P_c = \frac{2\sigma_l \sin(\theta + \phi)}{R - x \cot \phi} \quad (3.15)$$

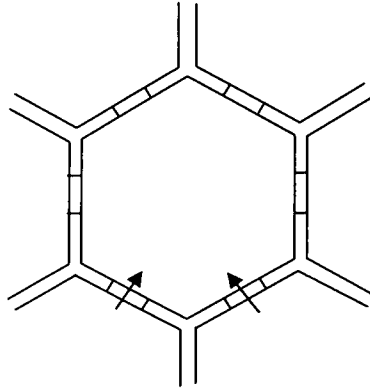


Fig. (3.3) 2-D representation for the pore

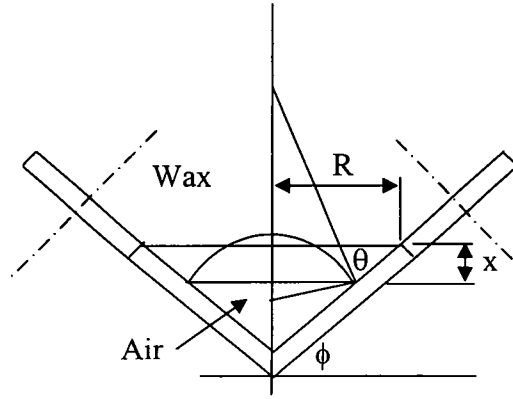


Fig. (3.4) Pore corner approximation

Where θ is the contact angle, σ_l is the surface tension of liquid PCM, ϕ is the corner angle, and R is the maximum radius of the groove, which will range from $15 \mu\text{m}$ to $30 \mu\text{m}$ for foam pore sizes from $100\text{-}200 \mu\text{m}$.

The contact angle and the surface energy of each material can be correlated as, $\cos \theta = 2\sqrt{\sigma_s \sigma_l} - 1$, where σ_s is the surface energy of the carbon foam. This correlation can be used only when the liquid PCM has larger surface energy than the carbon material, which is the case for untreated carbon. If the carbon surface is more energetic than the liquid wax, the contact angle will become zero and the equilibrium condition will be achieved by complete infiltration of the wax inside the grooves.

The force generated from the liquid pressure plus the capillary pressure will be balanced by the force generated from the compressed gas pressure inside the groove. If we consider that the gas inside the groove obeys the ideal gas law and it is compressed isothermally, the force balance can be written as,

$$P_l + \frac{2\sigma_l \sin(\theta + \phi)}{R - x \cot \phi} = P_{\text{init}} \frac{V_{\text{init}}}{V} \quad (3.16)$$

where P_{init} and V_{init} are the initial pressure and volume of the gas inside the groove. By assuming that the initial volume of the gas is the total volume of the conical groove and calculating the volume at equilibrium from the geometry in Fig. (3.5), equation (3.16) will take the following from:

$$1 + \frac{2\sigma_1 \sin(\pi - (\theta + \phi))}{RP_1 [1 - (x/R)\cot\phi]} = \frac{P_{init}/P_1}{[1 - (x/R)\cot\phi]^3} f(\theta, \phi) \quad (3.17)$$

Where, $f(\theta, \phi) = \frac{\tan\phi}{[2/\sin(\pi - \theta - \phi) + 1/\tan(\pi - \theta - \phi)][1/\sin(\pi - \theta - \phi) - 1/\tan(\pi - \theta - \phi)]^2 + \tan\phi}$.

Equation (3.17) is a cubic equation, which can be solved for $(1 - (x/R)\cot\phi)$ and hence the infiltration of the wax inside the groove can be determined. Using this simple model, we can estimate roughly the change of the contact area between the wax and the foam surface for different surface energy. The contact area between the carbon surface and the wax for each corner can be expressed as,

$$A_{cont} / A_T = \sqrt{x^2 + x^2 \cot^2 \phi} [2R - x \cot \phi] / (R^2 \sqrt{1 + \tan^2 \phi}).$$

The area ratio can be used as a weighting factor for the interfacial heat transfer coefficient between the PCM phase and carbon foam material. From calculations, the area ratio has been found to increase by more than 10 times, as shown in Fig. (3.5), when the carbon surface energy changed from 1 to 21 mJ/m², which is the surface energy of the wax at the infiltration temperature.

3.3 Numerical Technique

The partial differential equations (Equations 3.6-3.10) that describe the physical phenomena are complex and cannot be solved in closed form. A finite difference

technique based on the control volume approach in conjunction with numerical grid generation based on a body-fitted coordinate transformation is considered for solving this problem.

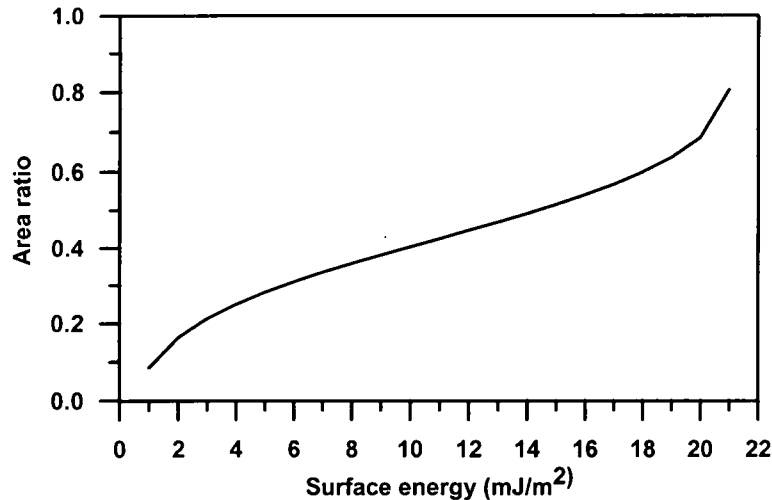


Fig. (3.5) Change of area ratio with carbon surface energy

3.3.1 Grid generation

When the system of governing equations is solved in a generalized non-orthogonal coordinate system, numerical grid generation becomes an integral part of the solution. An elliptic grid generator was developed to generate the grid. Elliptic grid generation is based on solving the elliptic partial differential equations that describe the coordinate transformation between the physical coordinates (x, y) and the curvilinear coordinates (ξ, η). A major advantage of this approach is that the interior grid will be very smooth.

The equations that relate (x, y) to (ξ, η) are two elliptic equations, which can be written as,

$$\xi_{xx} + \xi_{yy} = P(\xi, \eta), \text{ and}$$

$$\eta_{xx} + \eta_{yy} = Q(\xi, \eta) \quad (3.18)$$

where, P and Q are two additional functions to attract the grid lines to certain lines or points in space. At the boundaries the general coordinates (ξ, η) were monotone, each of them varying from one up to the total number of the grid points in each direction. Since we need to define locations of the grid points on the physical domain (x, y) , the above equations were transformed from (ξ, η) plane to (x, y) plane. The transformed equations took the following form:

$$\begin{aligned} a_{11}x_{\xi\xi} - 2a_{12}x_{\xi\eta} + a_{22}x_{\eta\eta} + J^2(Px_{\xi} + Qx_{\eta}) &= 0 \\ a_{11}y_{\xi\xi} - 2a_{12}y_{\xi\eta} + a_{22}y_{\eta\eta} + J^2(Py_{\xi} + Qy_{\eta}) &= 0 \end{aligned} \quad (3.19)$$

The functions P and Q that were used to concentrate the grid near any specified wall, were considered to take the following shape at any grid point (i, j) :

$$\begin{aligned} P(i, j) &= -C_{11}\text{Sign}(i - i_w)\text{Exp}(C_{12}|i - i_w|) \\ Q(i, j) &= -C_{21}\text{Sign}(j - j_w)\text{Exp}(C_{22}|j - j_w|) \end{aligned} \quad (3.20)$$

where i_w and j_w are the i and j indices of the line where the grid will be concentrated. The degree of concentration was defined by the values of the constants C_{11} , C_{12} , C_{21} , and C_{22} in the previous equations.

To generate the grid, the previous equations were discretized using a finite difference technique. The resulting algebraic equations were solved using Gauss-Seidel iteration with the application of a certain value of under-relaxation factor equal to 0.5 to prevent divergence.

3.3.2 Discretization of Conservation Equations

In order to convert the governing equations into algebraic equations for numerical solution, the governing equations were discretized using a control volume approach. A non-staggered grid was used where all the variables (velocities and all the other scalar variables) were stored at the control volume center. A typical control volume in the computational domain is shown in Fig. (3.6). Upon integrating the general governing equation of any generic variable ϕ (u , v , T_f , T_s), equation (3.11), over the control volume P and keeping $\Delta\xi = \Delta\eta = 1$, the following discretized equation was obtained.

$$\begin{aligned} \rho J \frac{\phi_P - \phi_P^{\text{old}}}{\Delta t} + (\rho U \phi)_e - (\rho U \phi)_w + (\rho V \phi)_n - (\rho V \phi)_s = & \left(\frac{\Gamma_\phi a_{11}}{J} \frac{\partial \phi}{\partial \xi} \right)_e - \left(\frac{\Gamma_\phi a_{11}}{J} \frac{\partial \phi}{\partial \xi} \right)_w \\ & \left[\left(\frac{\Gamma_\phi a_{22}}{J} \frac{\partial \phi}{\partial \eta} \right)_n - \left(\frac{\Gamma_\phi a_{22}}{J} \frac{\partial \phi}{\partial \eta} \right)_s + \left[- \left(\frac{\Gamma_\phi a_{12}}{J} \frac{\partial \phi}{\partial \eta} \right)_e + \left(\frac{\Gamma_\phi a_{12}}{J} \frac{\partial \phi}{\partial \eta} \right)_w \right. \right. \\ & \left. \left. - \left(\frac{\Gamma_\phi a_{12}}{J} \frac{\partial \phi}{\partial \xi} \right)_n + \left(\frac{\Gamma_\phi a_{12}}{J} \frac{\partial \phi}{\partial \xi} \right)_s + S_\phi J \right] \right] \end{aligned} \quad (3.21)$$

The last term on the right hand side of the previous equation can be considered as a source term. This source term can be divided into two parts, one coming from the non-orthogonality of the grid and the other is the physical source term that appears in the original equation:

$$S_{\text{non}} = - \left(\frac{\Gamma_\phi a_{12}}{J} \frac{\partial \phi}{\partial \eta} \right)_e + \left(\frac{\Gamma_\phi a_{12}}{J} \frac{\partial \phi}{\partial \eta} \right)_w - \left(\frac{\Gamma_\phi a_{12}}{J} \frac{\partial \phi}{\partial \xi} \right)_n + \left(\frac{\Gamma_\phi a_{12}}{J} \frac{\partial \phi}{\partial \xi} \right)_s$$

The physical source term was linearized based on Patanker [17] as follows:

$$(S_\phi)_P = S_u + S_p \phi_P \quad (3.22)$$

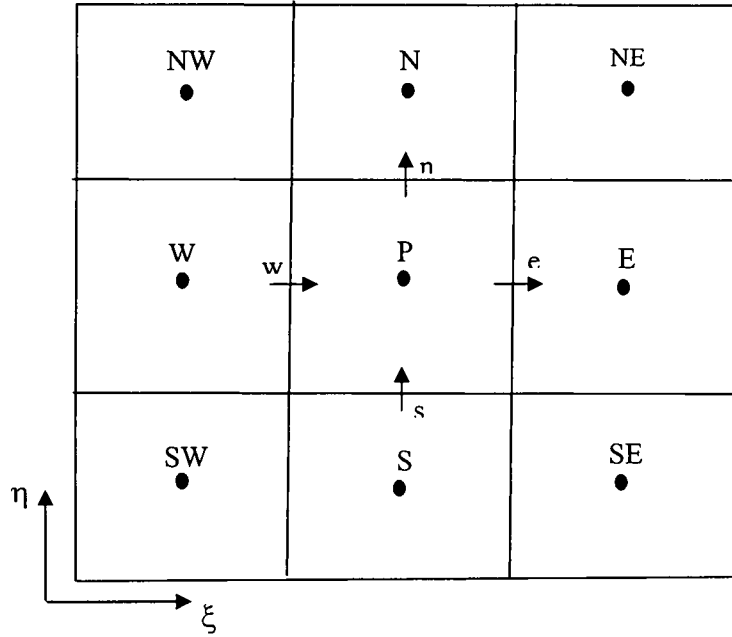


Fig. (3.6) Typical control volume in computational domain

The fluxes at the interfaces of the control volume P were evaluated using a hybrid scheme [17]. This scheme is based on a combination of the central and upwind differencing schemes. The central differencing scheme is employed for

$|\text{Pe}| = \left| \frac{\rho U}{\Gamma_\phi} \right|$, Peclet number, less than two. When $|\text{Pe}|$ is greater than two, the

upwind differencing scheme with neglecting diffusion is employed. Upon performing these operations, the final form of the discretized equation has taken the following form:

$$A_P \phi_P = A_E \phi_E + A_W \phi_W + A_N \phi_N + A_S \phi_S + S \quad (3.23)$$

where,

$$A_W = \max \left[(\rho U)_w, \left[\left(\frac{a_{11} \Gamma \phi}{J} \right)_w + (\rho U)_w / 2, 0 \right] \right],$$

$$A_E = \max \left[-(\rho U)_e, \left[\left(\frac{a_{11} \Gamma \phi}{J} \right)_e - (\rho U)_e / 2, 0 \right] \right],$$

$$A_S = \max \left[(\rho V)_s, \left[\left(\frac{a_{22} \Gamma \phi}{J} \right)_s + (\rho V)_s / 2, 0 \right] \right],$$

$$A_N = \max \left[-(\rho V)_n, \left[\left(\frac{a_{22} \Gamma \phi}{J} \right)_n - (\rho V)_n / 2, 0 \right] \right],$$

$$\text{and } A_P = (A_W + A_E + A_S + A_N + A_P^0 - \Delta F) - S_P J$$

$$\text{where } \Delta F = (\rho U)_e - (\rho U)_w + (\rho V)_n - (\rho V)_s, \text{ and } A_P^0 = \frac{\rho J}{\text{Const} * \Delta t}.$$

In the numerical solution, the non-orthogonal components were treated explicitly and added with the other source terms.

$$S = A_P^0 \phi_P^{\text{old}} + S_u J - \left[\left(\frac{a_{12} \Gamma \phi}{J} \frac{\partial \phi}{\partial \eta} \right)_e - \left(\frac{a_{12} \Gamma \phi}{J} \frac{\partial \phi}{\partial \eta} \right)_w + \left(\frac{a_{12} \Gamma \phi}{J} \frac{\partial \phi}{\partial \epsilon} \right)_n - \left(\frac{a_{12} \Gamma \phi}{J} \frac{\partial \phi}{\partial \epsilon} \right)_s \right] \quad (3.24)$$

Second order finite difference approximations were used to approximate the above derivatives, for example:

$$\left(\frac{\partial \phi}{\partial \eta} \right)_e = \frac{\phi_{NE} - \phi_{SE} + \phi_N - \phi_S}{4}$$

3.3.3 Treatment of momentum equations

The basic framework of the momentum equations is the same as any other scalar variable conservation equation. The only difference arises from the presence of the pressure gradient term. Velocities and pressure are mutually coupled and numerical treatment should deal with it accordingly. An equation for the remaining unknown pressure can be established by combining the continuity and momentum equations. One of the most popular schemes to achieve this is known as the SIMPLE algorithm, which stands for Semi-Implicit Method for Pressure-Linked Equations. We employed this scheme in the current study. The SIMPLE algorithm is based on guessing and correcting the pressure field until the resulting velocity field satisfies the continuity equation. To explain this procedure in some detail, it is assumed that the discretized equations for the momentum equations can be written for a guessed value of the pressure p^* as,

$$\begin{aligned} u_p^* &= \sum_{n=EWNS} A_n^u u_n^* + S^u + (B^u p_\xi^* + C^u p_\eta^*) \\ v_p^* &= \sum_{n=EWNS} A_n^v v_n^* + S^v + (B^v p_\xi^* + C^v p_\eta^*) \end{aligned} \quad (3.25)$$

where $B^u = \frac{-y_\eta}{A_p}$, $C^u = \frac{y_\xi}{A_p}$, $B^v = \frac{x_\eta}{A_p}$, and $C^v = \frac{x_\xi}{A_p}$.

The values of A^u and A^v have the same values as the coefficients in equation (3.23) but divided by the corresponding value of A_p for the u and v momentum equation respectively. The values of S^u and S^v represent all the source terms in the momentum equations except the pressure source term.

The superscript * for u and v denotes that they are based on the guessed pressure field p^* . In general, u^* and v^* will not satisfy the continuity equation and a net mass source will be produced. To remove this mass source, the pressure is assumed to be corrected by adding a pressure correction value p' .

$$p = p^* + p' \quad (3.26)$$

The velocity field is also assumed to be corrected based on this pressure correction pressure term as,

$$u = u^* + (B^u p'_\xi + C^u p'_\eta), \quad v = v^* + (B^v p'_\xi + C^v p'_\eta) \quad (3.27)$$

Based on these corrected values of u and v, the contravariant velocities U and V can be calculated as,

$$\begin{aligned} U &= U^* + (B^u y_\eta - B^v x_\eta) p'_\xi + (C^u y_\eta - C^v x_\eta) p'_\eta = U^* + B p'_\xi + C_{\text{non}} p'_\eta \\ V &= V^* + (C^v x_\xi - C^u y_\xi) p'_\eta + (B^v x_\xi - B^u y_\xi) p'_\xi = V^* + C p'_\eta + B_{\text{non}} p'_\xi \end{aligned} \quad (3.28)$$

The discretized continuity equation is taking the form:

$$(\rho U)_e - (\rho U)_w + (\rho V)_n - (\rho V)_s = 0 \quad (3.29)$$

After substituting the values of U and V from equation (3.28) into the discretized continuity equation (3.29), the continuity equation is converted into an equation in pressure correction. Upon substitution, the new pressure correction equation takes the following form:

$$\begin{aligned}
& \left(\rho B p'_\xi \right)_e - \left(\rho B p'_\xi \right)_w + \left(\rho C p'_\eta \right)_n - \left(\rho C p'_\eta \right)_s + \\
& \left[\left(\rho C_{\text{non}} p'_\eta \right)_e - \left(\rho C_{\text{non}} p'_\eta \right)_w + \left(\rho B_{\text{non}} p'_\xi \right)_n - \left(\rho B_{\text{non}} p'_\xi \right)_s \right] + m_p = 0
\end{aligned} \tag{3.30}$$

The quantity between the square brackets in the previous equation represents the non-orthogonal terms. In the numerical solution, this quantity will be treated explicitly and added to the resulting mass source term, m_p , that will take the following form:

$$m_p = \left(\rho U^* \right)_e - \left(\rho U^* \right)_w + \left(\rho V^* \right)_n - \left(\rho V^* \right)_s \tag{3.31}$$

The mass source term represents the imbalance in the continuity equation arising from the incorrect velocity field u^* and v^* , which are calculated based on the guessed pressure field p^* . With the second order center-difference approximations for the corrected pressure gradients on the cell boundaries and after some arrangements, the discretized pressure correction equation can be set on the general form as,

$$A_P^p p'_P = A_E^p p'_E + A_W^p p'_W + A_N^p p'_N + A_S^p p'_S + S^p \tag{3.32}$$

where $A_E^p = (\rho B)_e$, $A_W^p = (\rho B)_w$, $A_N^p = (\rho C)_n$, $A_S^p = (\rho C)_s$, and

$$A_P^p = A_E^p + A_W^p + A_N^p + A_S^p.$$

The discretized pressure correction equation, equation (3.32), will be solved iteratively with the two momentum equations for u and v to get the velocity and pressure field in the molten liquid phase of the PCM.

Using pressure correction scheme with ordinary grid arrangement produces pressure oscillations. The major source of this instability originates from the second order of the pressure gradient at the grid nodes. This scheme cannot sense the $1\Delta x$ pressure oscillation. Using a staggered grid in which the velocity control volume shifted $\frac{1}{2}\Delta x$ from the pressure control volume can eliminate this problem. However, this technique cannot be applied easily for irregular grids since the Cartesian velocity components are not related to the grid line orientations. For non-staggered grid, the velocities are stored at the centers of the control volumes while the contravariant velocities, which are functions of both u and v , are needed at the control volumes' interfaces. Thus, the velocity components at the interfaces have to be calculated since the velocities are stored at cell centers. This requires a suitable interface interpolation scheme that not only gives accurate velocity values but also maintains proper links with the adjacent pressures. The momentum interpolation scheme of Rhie and Chow [21] has been found to be suitable for this situation. In this scheme, the contravariant interface velocity at the control volume interfaces is set as a function of both the 1Δ and 2Δ pressure gradient approximations, for example the contravariant velocity at the east face is calculated according to:

$$U_e^* = \frac{U_E^* + U_P^*}{2} + (B)_e \left(\frac{P_E^* - P_P^*}{\Delta\xi} - \frac{P_E^* - P_W^*}{2\Delta\xi} \right) \quad (3.33)$$

3.3.4 Treatment of phase change and evolution of liquid-solid interface

The energy equation in the case of phase change could be inferred from the energy conservation principle, which simply states that the total enthalpy is

conserved. The total enthalpy can be divided into sensible and latent heat. Due to phase change processes, the total enthalpy shows a discontinuity at the transition temperature. The behavior of enthalpy change with temperature is very important during phase change processes. For pure PCMs, this change will behave like a step function and the jump will happen exactly at the melting temperature. Mixtures of PCMs or alloys show a continuous enthalpy curve as a function of temperature. This leads to a “mushy region” between the solid and liquid phase. Feustel [107] described the enthalpy change during phase change as a hyperbolic function as shown in Fig. (3.7). It can be described as,

$$h(T) = c_p T + \frac{L}{2} \left(1 + \tanh \left[\frac{2\beta}{\tau} (T - T_m) \right] \right) \quad (3.34)$$

where, β is a constant and τ represents the difference between the solidus and liquidus temperature for the PCM.

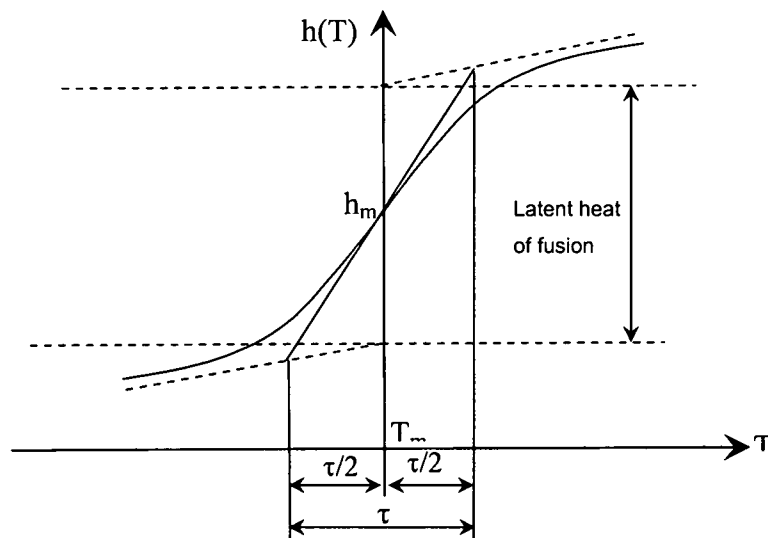


Fig. (3.7) Enthalpy change with temperature during phase change

In our calculations we assumed that the enthalpy and liquid fraction change linearly between the solidus and liquidus temperature as,

$$h(T) = c_p T + f_l L = c_p T + \left(\frac{T - T_{m1}}{T_{m2} - T_{m1}} \right) L \quad (3.35)$$

where T_{m1} and T_{m2} are the solidus and liquidus temperature and f_l is the liquid fraction.

The enthalpy porosity method was used to predict the phase change evolution. The essential feature of this method is that the latent heat evolution can be accounted for either defining the total enthalpy, an effective specific heat, or a heat source/sink term. In this study, a heat source/sink was assigned in the PCM phase energy equation to account for the latent heat evolution. The major advantage of this technique is that the numerical treatment can be achieved through simple modifications of the existing heat transfer numerical methods. Moreover, this technique could be more suitable to predict the profile of the mushy zone. The source term that appears in the PCM energy equation takes the form of, $S = -\rho L \delta \frac{df_l}{dt}$ J.

Adding this source term to the energy equation and updating the liquid fraction should be done carefully, because the value of this source term is very sensitive to the change in liquid fraction due to the high value of the latent heat of fusion. If the liquid fraction has not been updated appropriately, the temperature will fluctuate and the solution will diverge. A simple and robust scheme suitable for the general phase change system where the phase change happens through

a certain temperature range was used to update the liquid fraction. This scheme can be illustrated as follows:

After the k^{th} application of the solver, the discretized equation of the PCM phase energy equation can be set as,

$$A_p T_p = \sum_{nb} A_{nb} T_{nb} + S^T + \rho \delta L J \frac{(f_l^{\text{old}} - f_l^k)}{\Delta t} \quad (3.36)$$

where, S^T represents all the source terms except for phase change. If the phase change is occurring at the p^{th} node, then the k^{th} estimate of nodal temperature should be such that $T_p = F^{-1}(f_p)$, which is the inverse of the liquid fraction-temperature relationship, which will take this form:

$$F^{-1}(f_l) = \begin{cases} T \leq T_{m1} & \text{if } f_l = 0 \\ f_l (T_{m2} - T_{m1}) + T_{m1} & \text{if } 0 \leq f_l \leq 1 \\ T \geq T_{m2} & \text{if } f_l = 1 \end{cases} \quad (3.37)$$

To achieve this k^{th} estimate of the liquid fraction, the value of f_l needs to be corrected such that:

$$A_p F^{-1}(f_l) = \sum_{nb} A_{nb} T_{nb} + S^T + \rho \delta L J \frac{(f_l^{\text{old}} - f_l^k - \Delta f_l)}{\Delta t} \quad (3.38)$$

where Δf_l is the required correction to the liquid fraction. Subtracting equation (3.38) from equation (3.36), the corrected liquid fraction can be approximated as,

$$\Delta f_l = A_p \frac{T_p - F^{-1}(f_p)}{\rho \delta L J / \Delta t}.$$

The updated liquid fraction is set as,

$$f_l^{k+1} = f_l^k + \lambda(\Delta f_l) \quad (3.39)$$

where, the parameter λ is an under-relaxation factor, which helps to achieve convergence. To get rid of any unrealistic results, the liquid fraction is subjected to this restriction,

$$f_l^{k+1} = \begin{cases} 0 & \text{if } f_l^{k+1} < 0 \\ 1 & \text{if } f_l^{k+1} > 1 \end{cases}.$$

As mentioned above, due to the large values of the added source term the solution can diverge unless the under-relaxation factor λ is selected wisely. Practical experience indicates that a relaxation value in the range of 0.4-0.7 will provide efficient convergence. The liquid-solid interface is defined based on the distribution of the calculated liquid fraction.

The permeability of the porous medium is calculated based on the actual porosity of the porous matrix and the liquid fraction of the PCM inside the pores. The permeability is calculated based on the analytical formula derived by Fourie and Du Plessis [68] for isotropic open cell high porosity foam.

$$K = \frac{\varepsilon^2 d^2}{36(\chi - 1)\chi} \quad (3.40)$$

$$\text{where } \frac{d_p}{d} = \frac{3 - \chi}{\chi} \text{ and } \chi = 2 + 2 \cos \left[\frac{4\pi}{3} + \frac{1}{3} \cos^{-1}(2\delta - 1) \right].$$

The variable ε is the product of the porous matrix porosity δ and the PCM liquid fraction f_l . In the region where the PCM is in the solid phase, the variable ε is set to a very small number. This results in a very small value for the calculated permeability and consequently makes the Darcy and Forchheimer source terms in the momentum equations dominate all the other terms and bring the velocities to

nearly zeros. Inside the totally-melted regions, the problem has been treated as natural convection in porous media.

3.4 Numerical procedures

Control volume formulation and discretization reduced the governing equations at every control volume nodes to a set of multivariable algebraic equations. These sets of algebraic equations can be solved numerically. In this work, a line-by-line TDMA (Tri-Diagonal Matrix Algorithm) solver was used to solve these algebraic equations. Under-relaxation factors were used for all the equations (u velocity, v velocity, corrected pressure, solid phase temperature, PCM phase temperature, and for updating liquid fraction) to ensure solution stability. The convergence was assumed to be achieved when the normalized summation of the residuals over all the computational cells reduced to 10^{-4} . The residuals in the energy equations were normalized by a reference value equals to the heat power flowing inside the system. The mass residual was normalized by the total mass of the PCM. After generating the grid and initializing all the dependent variables, the numerical solution procedure for every time step could be summarized, as shown in the flow chart Fig. (3.8), as follows:

- 1- Set a guessed value for the pressure field and solve the momentum equations, equation (3.25) based on this guessed value
- 2- Define the contravariant velocities at the control volume faces based on Rhie and Chow interpolation, equation (3.33), to calculate the mass imbalance source term from equation (3.31)

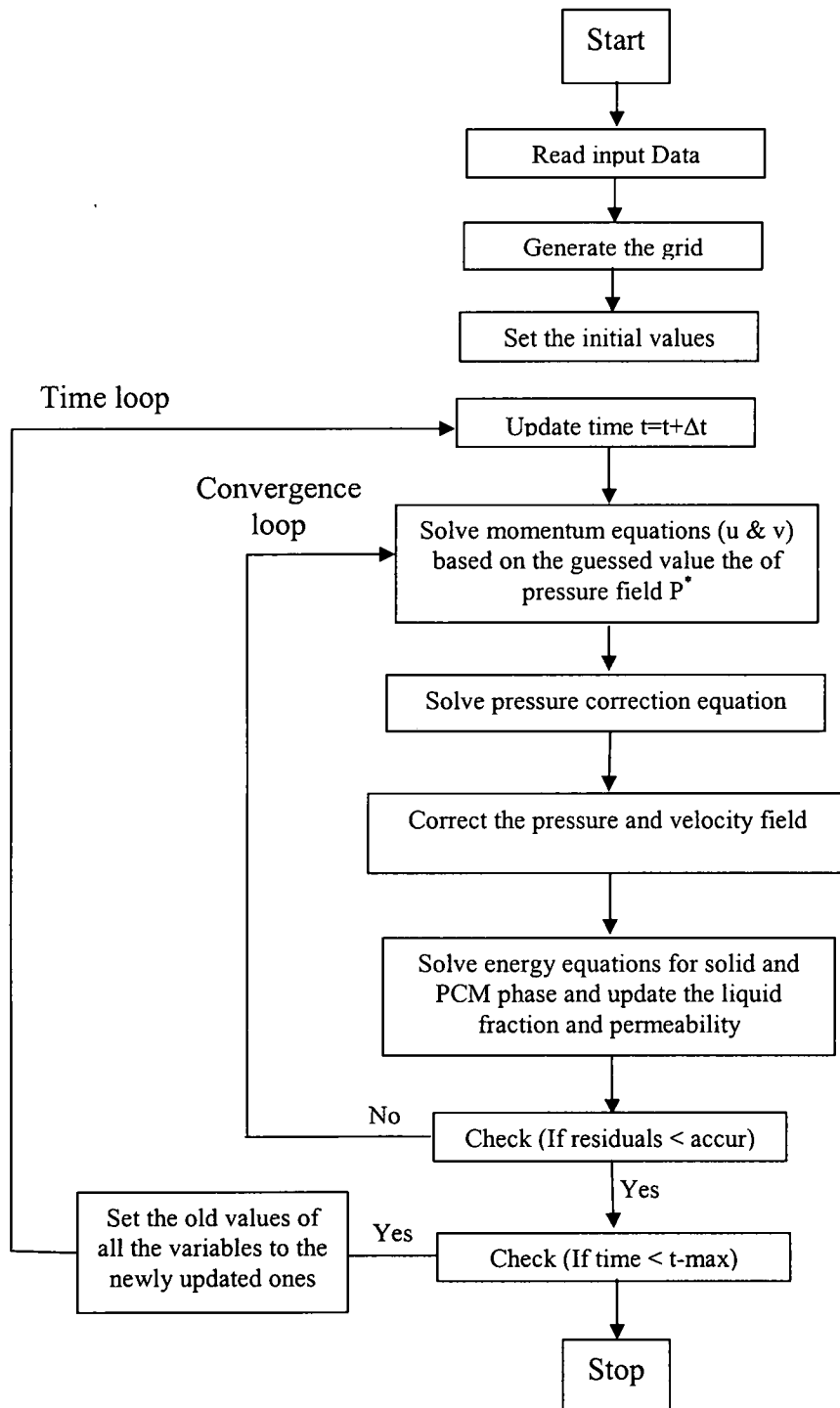


Fig. (3.8) Simple flow chart for the numerical procedure

- 3- Solve the pressure correction equation, equation (3.32), to get the pressure correction value p'
- 4- Correct the pressure and velocity fields based on equations (3.26) and (3.27)
- 5- Solve the discretized form of PCM phase and solid matrix phase energy equations, equations (3.12) and (3.13)
- 6- Based on the temperature field of the PCM phase, update the liquid fraction of the PCM, from equation (3.39)
- 7- Calculate the new values of permeability based on the calculated values of liquid fraction, from equation (3.40). Based on the updated permeability, the Darcy and Forchheimer momentum source terms will be calculated.

3.5 Validations

The generalized coordinate control volume numerical method presented in this chapter can be considered as a flexible and robust way to solve heat transfer problems with phase change inside a porous system occupying regular or irregular geometries. Before going on to apply it in our application, using high thermal conductivity porous matrix infiltrated with PCM in energy storage and cooling applications, some validation tests will be performed to ascertain the validity and applicability of the numerical solution. We will try to restrict our validation tests to some cases for which we have documented experimental and numerical results from the literature. The validations will include melting of pure PCMs occupying a rectangular cavity, natural convection inside a square cavity

filled with porous media, packed bed saturated with liquid Gallium, and melting of PCMs inside an irregular shape PCM energy storage.

3.5.1 Melting of Pure Gallium inside rectangular cavity

Gau and Viskanta [9] performed a benchmark experiment to study melting of pure materials. In their experiments, they studied melting of Gallium in a rectangular cavity that had inside dimensions of (8.89 X 6.35 X 3.81 cm). The left and right walls served as an isothermal heat source/sink. They were made of multi-pass heat exchangers machined from copper plate. The other walls, sides, bottom and top, were made of plexiglass. They selected the material, Gallium, for different reasons. First, the thermo-physical properties are reasonably well established and the volume change during melting is not high. Second, it has a lower melting temperature, which is very near to the ambient temperature. This low melting temperature will minimize the losses. The performance of the present model in studying melting or solidification in a regular geometry has been verified with this benchmark experiment. The grid and the geometry of the cavity are shown in Fig. (3.9), the grid has been concentrated besides the isothermal walls. The non-dimensional parameters corresponding to this case were $Ra = 1.962E6$, $Pr = 0.021578$, and $Ste = 0.04616$.

It was found that at the early stage of the melting process some convection vortex cells are formed beside the isothermal hot wall. The appearance of these vortex cells was dependent on the grid density. Through a grid sensitivity study, we have found that these cells did not appear for a coarse grid beside the hot wall. The vortex motion of the liquid phase at this early stage

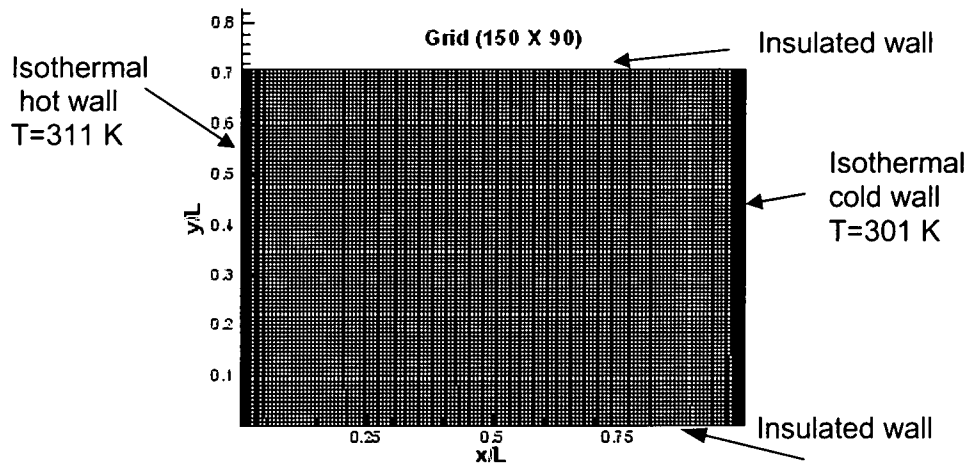


Fig. (3.9) Geometry and grid for the rectangular cavity

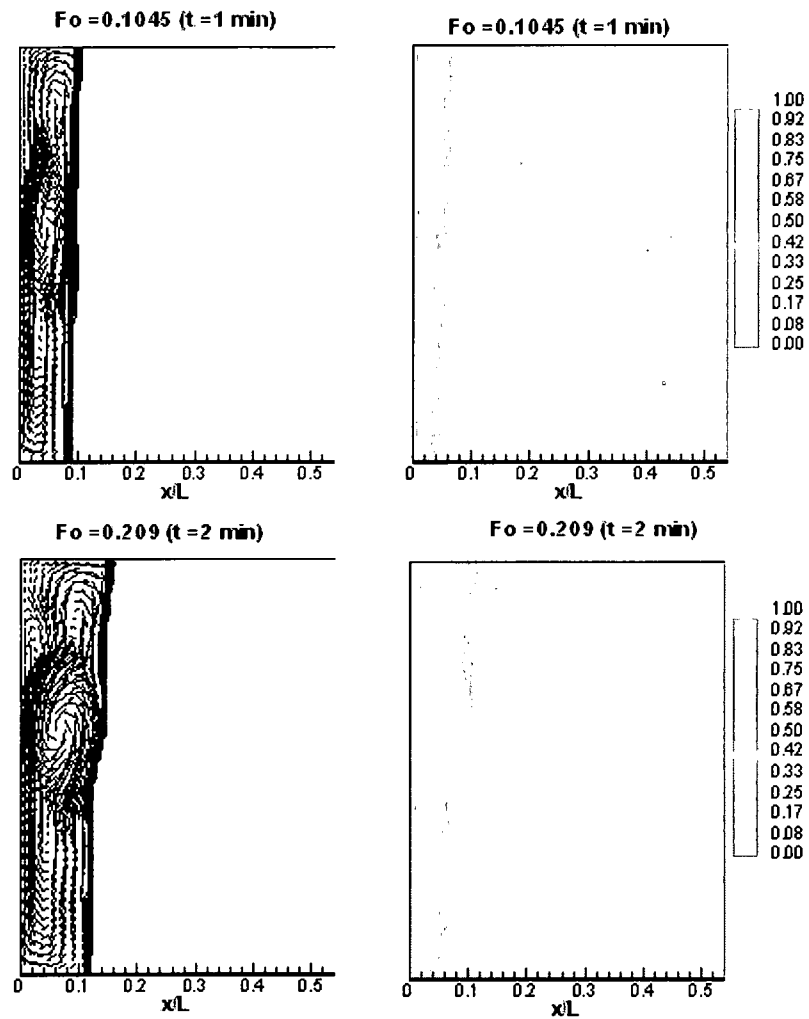


Fig. (3.10) Velocity vectors and temperature contours at early stage of melting, $Fo=0.1045$ and 0.209

of melting affected the liquid-solid interface shape and also the temperature field as shown in Fig. (3.10). During the following stages of the transient melting process, it was found that these small vortices merged together to form bigger ones as shown in Fig. (3.11). The location of the liquid-solid interface was compared with the experimental results at different time levels. Good agreement has been found between the numerical and the experimental data as shown in Fig. (3.12).

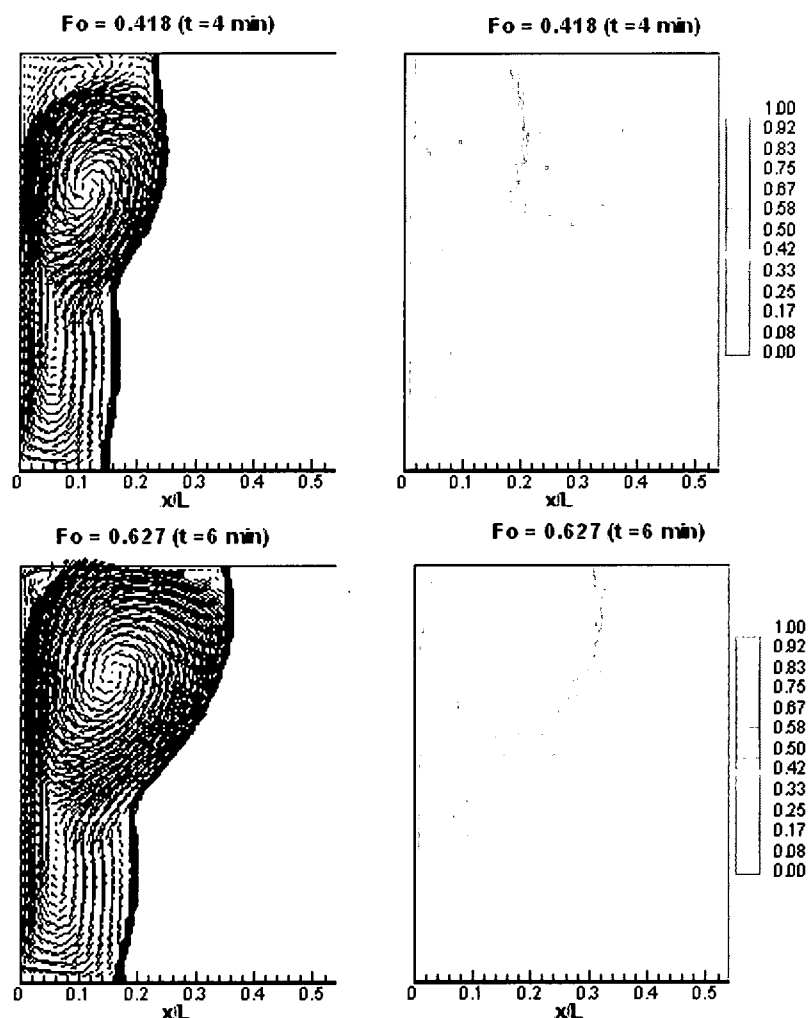


Fig. (3.11) Velocity vectors and temperature contours at later stage of melting, $Fo=0.418$, and 0.627

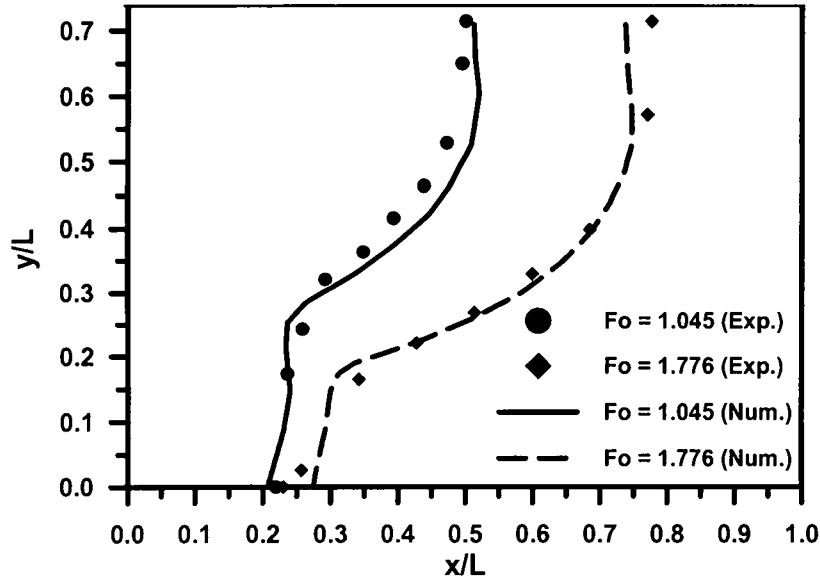


Fig. (3.12) Comparison between experimental and numerical liquid solid interface at different times

3.5.2 Melting of pure PCM in irregular geometry

Due to the lack of experimental results for melting in irregular geometry, we validated our model with another numerical study carried out by Khillarkar et al. [40]. They were studying free convection-dominated melting of a pure PCM contained in concentric horizontal annuli. The configuration of their geometry was a square external tube with a circular tube inside it. The inner cylindrical wall was subjected to uniform temperature higher than the melting temperature of the PCM and the outer wall was kept insulated. Using our grid generator, we generated a fine grid for this configuration. The grid is shown in Fig. (3.13). They used fixed grid technique in their simulation and used a finite element method to solve the equations. The comparison has been carried out for the same conditions, which are summarized in table (3.2).

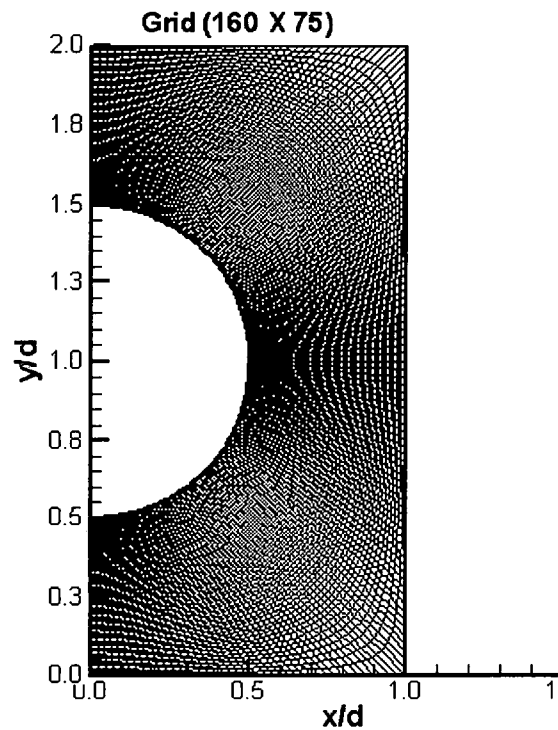


Fig. (3.13) Grid for the irregular energy storage

Table (3.2) Run inputs for code validation case

Ra	2.844×10^6	$k_{\text{solid}} / k_{\text{liquid}}$	2.419
Ste	0.138	$cp_{\text{solid}} / cp_{\text{liquid}}$	0.964
Pr	46.1	Initial temperature [K]	300.0
Melting temp. [K]	300.4	Hot wall temp. [K]	316.0

The temperature field and velocity vectors at different times during the melting process are shown in Fig. (3.14). At the beginning of the melting process, the melting was controlled mainly by conduction and the liquid solid interface moved uniformly in all directions away from the hot inner cylinder wall. When the liquid layer started to increase at $Fo > 0.04$, two convection cells started to

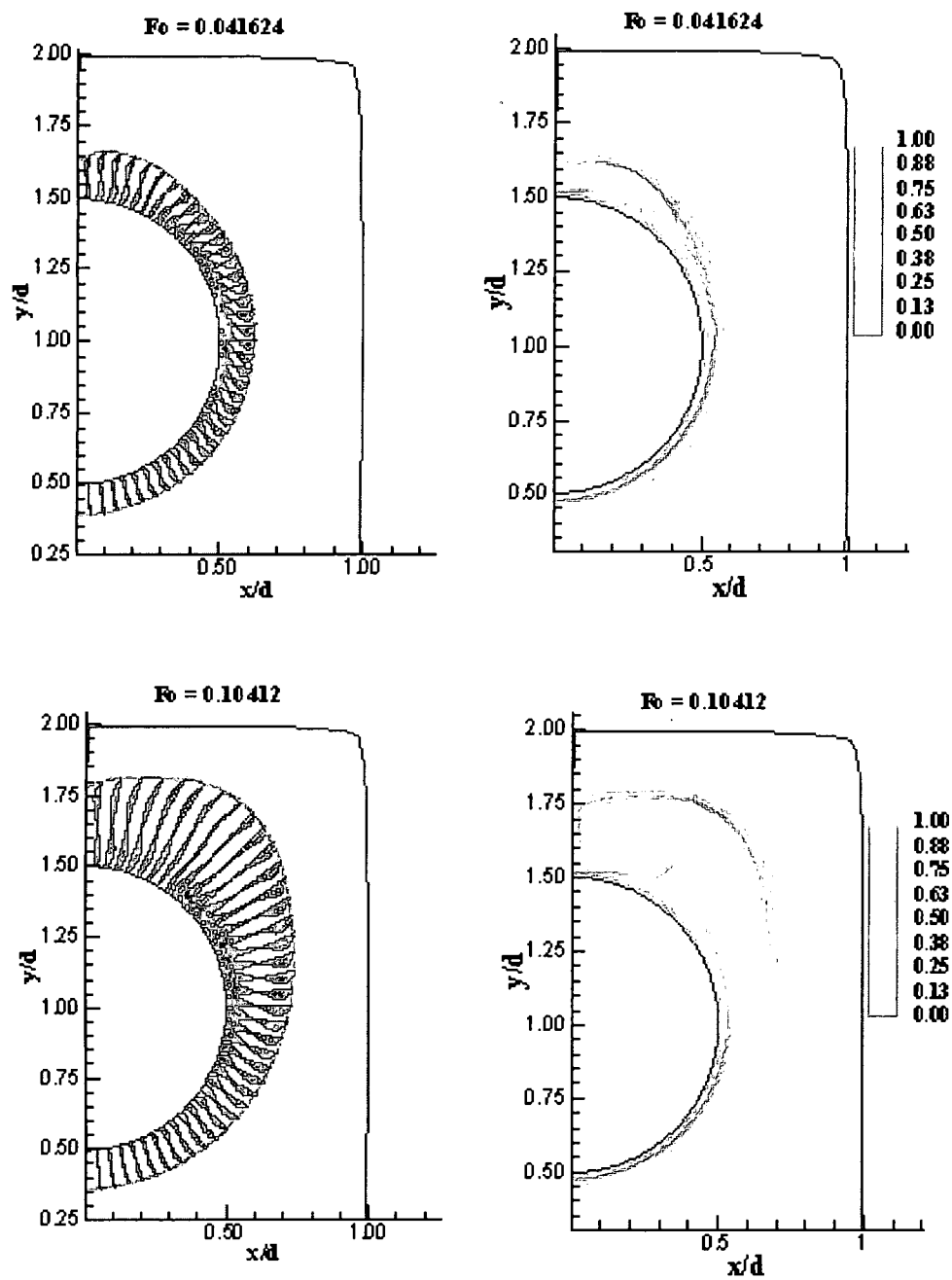


Fig. (3.14) Velocity vectors and temperature contours at different times for irregular energy storage

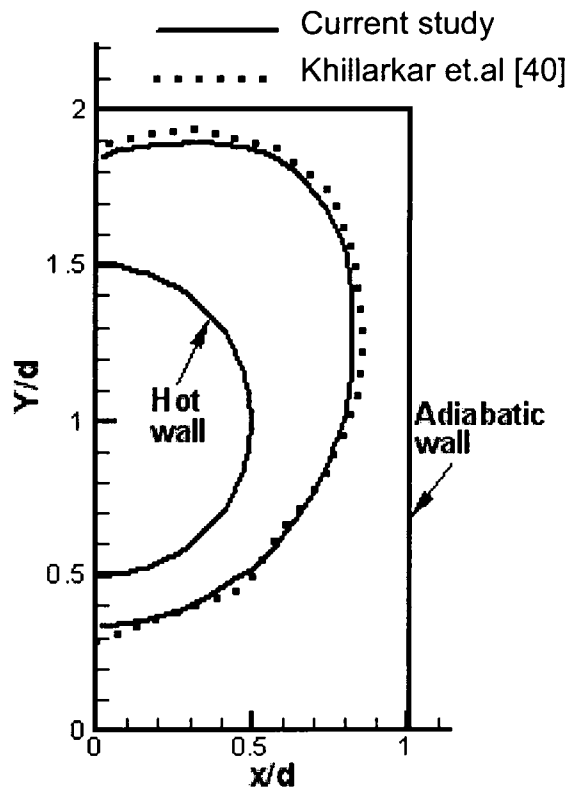


Fig. (3.15) Comparison of liquid solid interface at $Fo = 0.1296$

appear. The generation of these two cells came due to the interaction between two streams. One of these streams came from the motion of the cold liquid phase beside the melting interface at the top of the inner cylinder downward and the second stream came from the motion of the hot liquid around the inner cylinder upward. When these two streams intersected, the hot stream separated from the inner cylinder surface and generated a clockwise convection cell. As time goes on, these cells got bigger. Solid-liquid interface at Fo equal to 0.1296 for our code and for Khillarkar work is shown in Fig. (3.15). As shown from the figure, the two results were in agreement.

3.5.3 Convection heat transfer in a porous cavity

Since our study is dealing with a porous system, convection heat transfer inside a square cavity filled with packed beads totally saturated with liquid phase has been investigated using our two-energy equation model. The equations are solved in unsteady state form and the steady state is considered to be achieved when the solution reaches the state where there is no change in the values of all the dependent variables with time. We considered the case of Beckermann, et al. [72] for natural convection in a square cavity filled with glass beads saturated with liquid Gallium. This case study was for $Da=1.37 \times 10^{-5}$, which was corresponding to porosity equal to 0.385, and the Rayleigh number was equal to 7.19×10^5 . The cavity was subjected to isothermal hot and cold surfaces on the left and the right sides respectively while the top and bottom surfaces were insulated. In this case, heat transfer was driven by the liquid phase because liquid gallium has higher thermal conductivity compared to the glass beads.

The non-dimensional quantities relating the thermal properties of both the liquid and solid phases are considered as: $k_{seff}/k_f = 0.0192$, $k_{feff}/k_f = 0.25$, and $(\rho c p)_s/(\rho c p)_f = 0.85$. These values were calculated after estimating the effective thermal conductivity of both the solid and liquid phases. The velocity vectors and the nondimensional temperature contours are shown in Fig. (3.16). The numerical results of temperature distribution along x-axis at different levels are compared with the experimental results as shown in Fig. (3.17). The results showed a very good agreement with the experimental data except at the regions

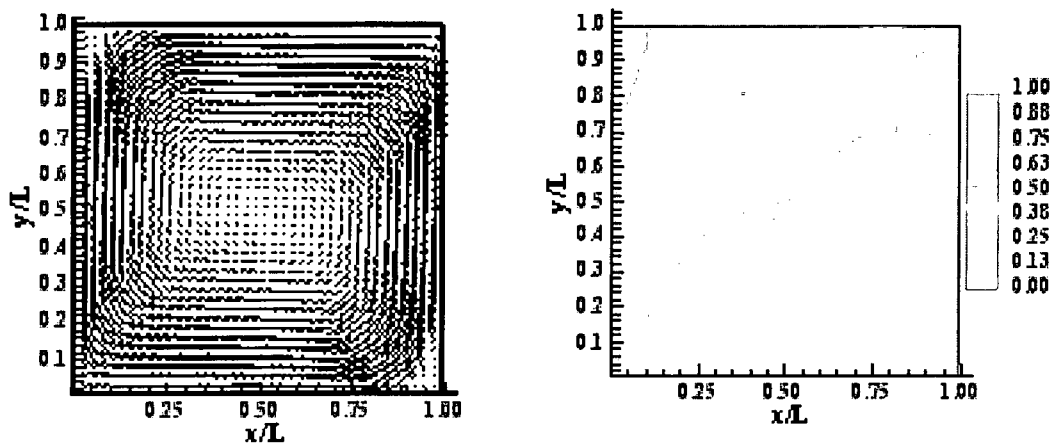


Fig. (3.16) Velocity vectors and temperature contours for porous cavity, $Da=1.37E-5$, $Ra=7.19E5$

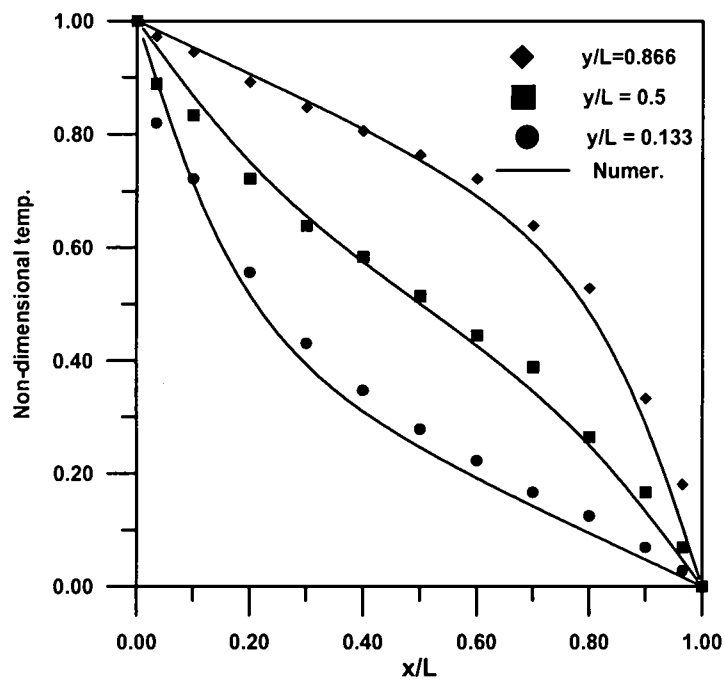


Fig. (3.17) Comparison of temperature profile with experimental measurements for porous cavity

very close to the isothermal walls. This may be due to the channeling effect, which we did not consider in this case.

A parametric study has been carried out to check the performance of the model for different Darcy and Rayleigh numbers. The heat transfer process and the deviation from the local thermal equilibrium has been monitored by showing the temperature contours of the liquid phase and the contours of the absolute value of the difference between the liquid and solid phase temperatures. It was found that increasing the Darcy and Rayleigh number has the same effect in intensifying the liquid motion inside the porous media and therefore increasing the heat transfer coefficient. The temperature gradient at the lower left corner and upper right corner increased with increasing Darcy and Rayleigh numbers, which means higher values for Nusselt number at these locations as shown from Figs. (3.18-3.21). The regions where the solid and the liquid phase temperatures deviated from each other were the regions beside the upper right corner and the left lower corner of the cavity. This was attributed to the impinging of the hot fluid at the top on the cold right wall and the cold fluid at the bottom on the left hot wall respectively. The temperature difference between the solid and liquid phase increased as the Darcy and Rayleigh number increased. This was obviously due to the increase in liquid convection motion inside the cavity.

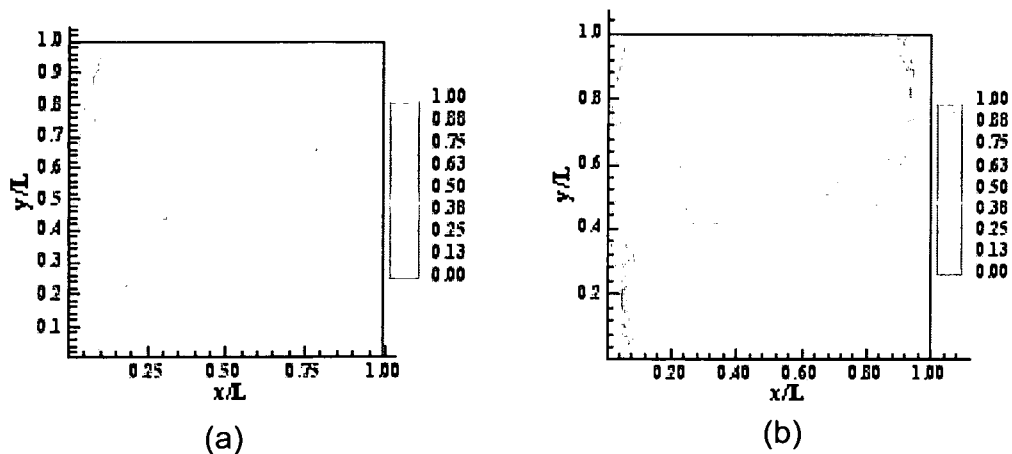


Fig. (3.18) Fluid temperature contours for different Da
a) $Da = 1.37E-5$, $Ra = 7.19E5$
b) $Da = 1.162E-3$, $Ra = 7.19E5$

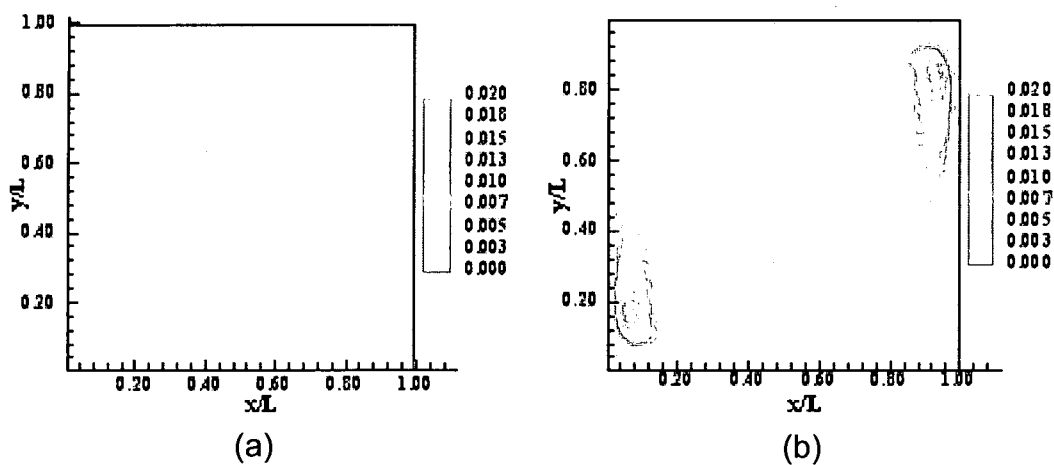


Fig. (3.19) Solid-liquid temperature difference contours for different Da
a) $Da = 1.37E-5$, $Ra = 7.19E5$
b) $Da = 1.162E-3$, $Ra = 7.19E5$

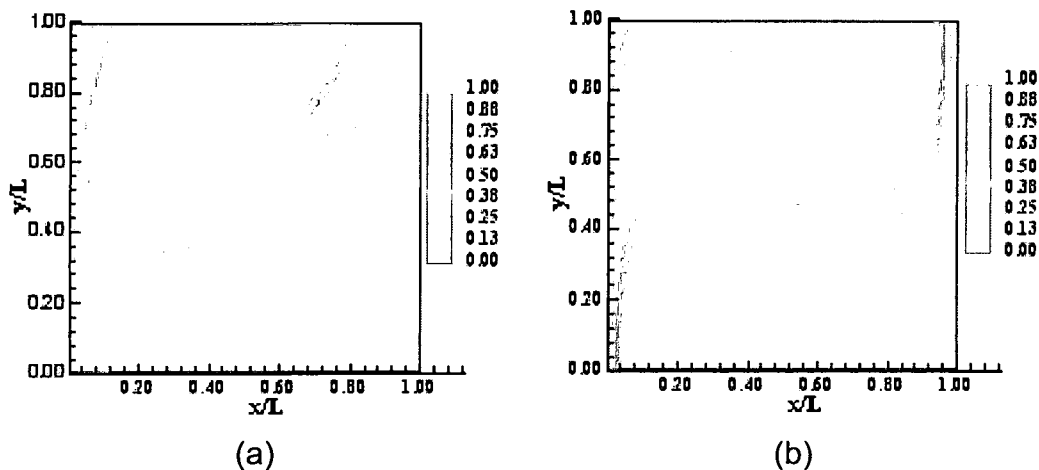


Fig. (3.20) Fluid temperature contours for different Ra

a) $Da = 2.035E-4$, $Ra = 1.438E5$

b) $Da = 2.035E-4$, $Ra = 3.595E6$

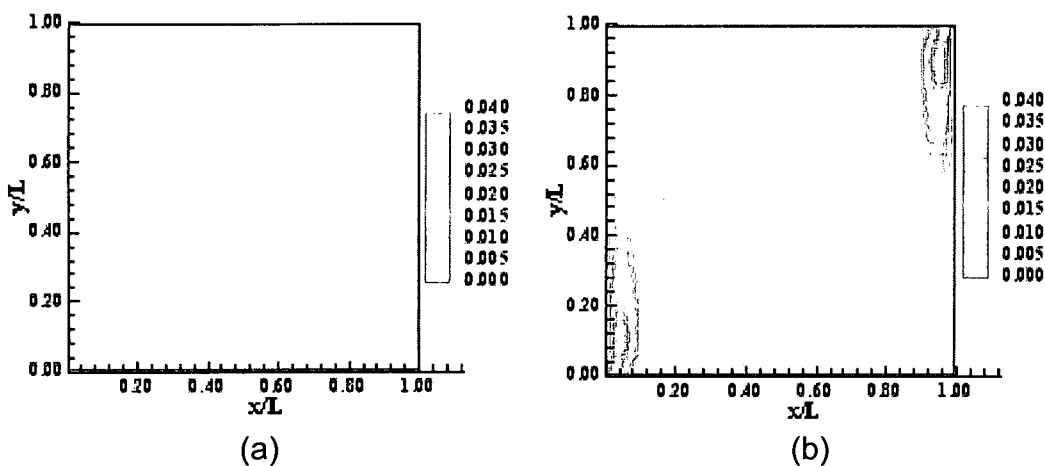


Fig. (3.21) Solid-liquid temperature difference contours for different Ra

c) $Da = 2.035E-4$, $Ra = 1.438E5$

d) $Da = 2.035E-4$, $Ra = 3.595E6$

CHAPTER 4

EXPERIMENTAL WORK

4.1 Introduction

Numerical results need to be validated with experiments to make sure that the assumptions used in the modeling process are accepted. In this chapter, we performed an experimental work to study heat transfer and phase change processes inside high thermal conductivity foam saturated with PCM. Both Aluminum and carbon foam were used. In the case of using carbon foam, the surface of the foam was activated to increase the foam-PCM wettability. The work started with building an experimental setup to measure the temperature field and to capture the liquid-solid interface motion during the melting process. At the same time, the test rig was adjusted to measure the thermal conductivity of the porous foam material, which we used in this study. All PCM properties such as viscosity, melting point, specific heat, and latent heat of fusion were measured using a rheometer and DSC respectively. All the experimental facilities and measurements used in this study are described below.

4.2 Experimental facilities

4.2.1 Guarded hot plate (As a heat source)

The principle of the guarded hot plate is to generate a known unidirectional heat flux through the specimen of interest. This apparatus was used mainly to measure the thermal conductivity. To achieve unidirectional heat flow, it is customary to use a heater plate composed of two parts, a central plate (or main heater) surrounded by an annular guarded heater and separated from it by a small air gap, which acts as a thermal barrier. Electrical power is supplied to the guarded heater independently of the main heater and the heat flux produced serves to maintain the heat flow perpendicular to the hot face in the central metering region, thereby creating isothermal planes across the measured region of the specimen. We used the guarded hot plate to generate a heat flux inside our samples. The left surface of the heater was insulated and the sample was fixed in contact with the right surface.

The heat was supplied to the main and guarded heater through two well-controlled power supplies, one for the main heater and the other for the guarded heater. Both the main and guarded power supplies were Kepco model, series ATE for the main heater and JQE series for the guarded one. Both of these power supplies were quarter-rack (100 Watt maximum). The maximum output voltage and current were 100 DC volt and one amp respectively.

4.2.2 Data acquisition

A high performance analog and digital 16 bits I/O board DT2805 which is compatible with IBM personal computers was used to control the power output

from both main and guarded power supplies as well as to measure the thermocouples' output. This board could be programmed from the personal computer's interpreted or compiled BASIC language to perform analog to digital (A/D) conversions, digital to analog (D/A) conversions, and digital input and digital output transfers. The board also contained an on-board programmable clock, which could be used to provide clock pulses to control the operations of the board A/D and D/A subsystems.

A visual basic program was developed to make the interface between the DT2805 board and the PC. The interface program allowed controlling the output power of both main and guarded heaters, reading the thermocouples output and converting them to temperature, recording the temperature time history, and performing any other required calculations. The temperature field of the porous matrix with the PCM was measured using accurate K-type thermocouples.

4.2.3 Samples

Cubic high porosity aluminum and carbon foam samples of dimensions 4"x 4" x 2" were used in this study. Different samples with different porosity and pore size were selected for Aluminum foam. Aluminum foam is an open cell structure foam. The edges of its cells are composed of metal fibers with lumping of solid material at their intersections. Two quantities, the porosity and the pore density are used to describe this type of foam, where the latter is expressed in units of pores per inch (PPI). The properties of the Aluminum foam as delivered by the manufacturer, ERG (Energy Research and Generation corp.) are listed in table (4.1).

Three Carbon foam samples with different surface energy were prepared to investigate the effect of foam surface energy on the thermal performance.

Table (4.1) Aluminum foam properties

Sample #	# Pores Per Inch (PPI)	Foam density (1.0-Porosity)	Pore diameter (d_p) [m]	Fiber diameter (d_{fiber}) [m]
1	5	6.3 %	0.0042	0.0005
2	10	6.6 %	0.0033	0.0004
3	20	6.1 %	0.0027	0.00033
4	40	6.3 %	0.0019	0.00024
5	10	3.4 %	0.0033	0.00037
6	10	11.8 %	0.0034	0.00043

All the samples dimensions are 4" X 4" X 2", with tolerances: Thickness ± 0.01 ", Length and Width ± 0.03 "

4.3 Thermal conductivity measurement

A schematic of the experimental setup for thermal conductivity measurements is shown in Fig. (4.1). The heater of the guarded hot plate was insulated from one side, by a two cm thick styrofoam layer. The other side of the heater was taped at the top of the foam sample. A flow of cooling water was used to cool the bottom side of the sample. The rest of the foam sides were insulated by thick layers of styrofoam.

Fourteen K-type thermocouples were used to measure the temperature at different points. Three were attached between the heater and the top foam

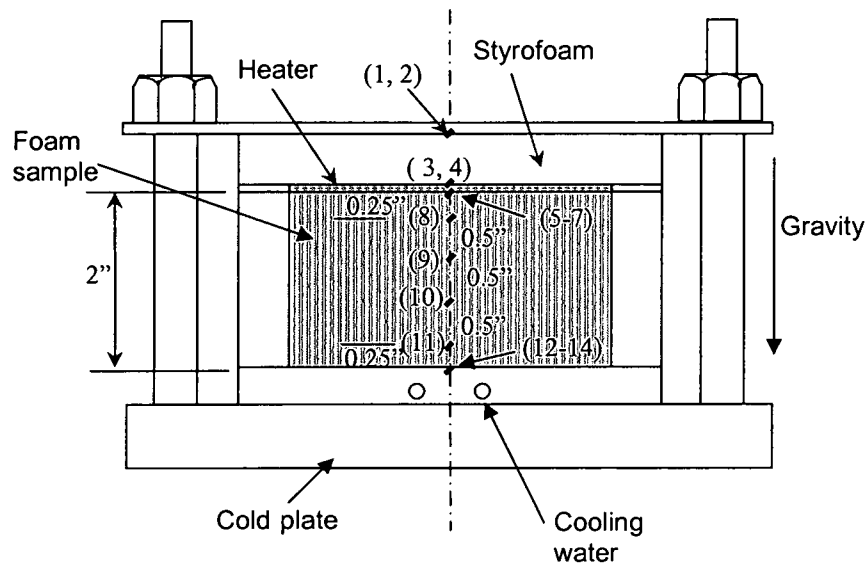


Fig. (4.1) Test rig for thermal conductivity measurement
(The number between brackets is the thermocouple number)

surface and three between the cold plate and the lower foam surface. To estimate the losses from the upper Styrofoam plate, two thermocouples were attached at each side of the styrofoam layer. Also, four thermocouples were attached inside the foam material at different levels through small plastic tubes. All the thermocouples were hooked up to the data acquisition to record the temperatures.

Since the metal foam sample was heated from the upper side and cooled from the lower side and insulated from the other four sides, the heat conduction is expected only in one direction and the air convection motion inside the foam pores will be negligible. Thus if the net heat from the heater is q , then at steady

state condition, $q - q_{\text{loss}} = k_{\text{eff}} A \frac{\Delta T}{L}$, and $k_{\text{eff}} = \frac{(q - q_{\text{loss}})L}{A\Delta T}$.

Only the losses from the upper side are estimated by measuring the temperature difference across the Styrofoam upper layer. This loss was negligible (less than one percent of the heater power). The thermal conductivity was calculated based on the temperature difference between the thermocouples (5-7) and (12-14) considering L as the total thickness of the foam sample. To make sure that the contact resistance between the foam sample and both the heater and the cold plate has minimal effect, the thermal conductivity also was measured based on the temperature difference between thermocouples 8 and 11 considering $L=1.5''$. Both of the two values were very close to each other. The calculated values for the effective thermal conductivity are shown in Table (4.2). The values showed that the effective thermal conductivity is mainly related to foam porosity because it changed from 2.7 to 7.5 when the porosity decreased from 96.6% to 88.4%. The smaller pore size foam with 40 PPI showed lower thermal conductivity. This could be attributed to the increase in the tortuous path of the heat as the pore size of the foam decreases.

Table (4.2) Measured thermal conductivity of Aluminum foam

Sample	K_{eff} [W/mK]
5PPI, 93.7% porosity	5.0
10PPI, 93.4% porosity	5.2
20PPI, 93.9% porosity	5.0
40PPI, 93.7% porosity	4.5
10PPI, 96.6% porosity	2.9
10PPI, 88.4% porosity	7.5

The temperature time history at points 8, 9, 10, and 11 with the calculated thermal conductivity near steady state conditions is shown in Fig. (4.2). It is shown that the temperature difference between each successive two points is equal, which means that the heat transfer was mainly due to conduction and the air motion effect was negligible.

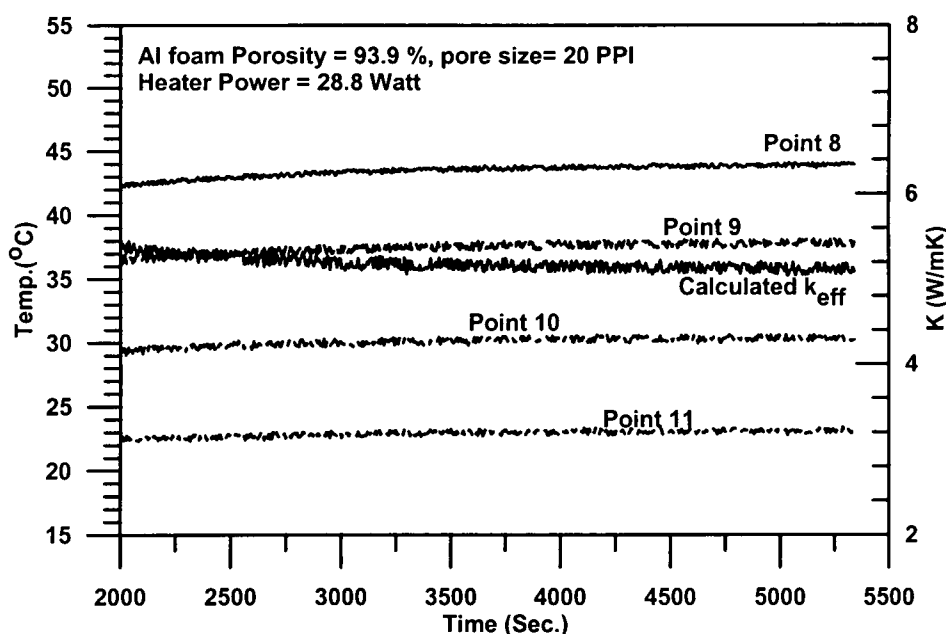


Fig. (4.2) Temperature time history and the calculated effective thermal conductivity for foam 20PPI, 93.9%, near the steady state condition

To estimate the percentage of error in the thermal conductivity measurements, the uncertainty in the thermocouple readings, the heater power, and the dimensions of the samples were estimated. For the thermocouples, it was found that the uncertainty of its readings is about ± 0.2 °C. This means that for the temperature difference of about 20 °C, the percentage of error in the temperature difference will be about one percent. According to the data provided

by the foam samples manufacturer, the uncertainty of the foam dimensions was ± 0.01 " in thickness and ± 0.03 " in length and width. This will give 0.5% error in thickness and 1.06% error in the area. Considering that the error in power will be in the range of two percent and the losses from the side walls will be in the range of one percent, and upon combining these individual uncertainties using Kline and McClintok [108], the uncertainty in the thermal conductivity measurements will be,

$$\%k_{\text{eff}} = \sqrt{(\% \text{power})^2 + (\% \text{Area})^2 + (\% \Delta T)^2 + (\% L)^2 + (\% \text{losses})^2} = \pm 2.8\%.$$

4.4 Carbon foam surface activation and surface energy measurements

Carbon foam samples were activated using CO₂ as an activating agent. First, the samples were heated up to 900°C in inert atmosphere of Argon. Once the temperature was stabilized at 900°C, the inert gas was replaced by CO₂ for a time of one hour for foam 2 and three hours for foam 3.

The surface energy of the foam was measured using iGC (Inverse Gas Chromatography). A flame ionization detector (FID) was used to determine the retention times. IGC columns were prepared by packing the sample into a standard column (300 mm long and 3 mm inner diameter). Columns were packed manually by cutting a section of the sample and packing it into the column. Columns were analyzed two times in a row to check for irreversible sorption effects and equilibrium after preconditioning. Samples were exposed to the following pre-treatment and measurement conditions. Initially, the columns were preconditioned at 30 °C for two hours and 0% RH to achieve equilibrium throughout the sample. Then, the surface energy measurements were performed

at 30 °C and 0% relative humidity (RH) with a two-hour conditioning between runs on the same column. Then, the samples were heated to 30-105 °C for five hours to remove any surface contaminants. Finally, the samples were cooled back down to 30 °C and the surface energetics were measured again. All experiments were carried out at 10 sccm total flow rate, 100 μ l loop size, and injection vapor concentration of 0.03 P/P₀ for all elutants. Table (4.3) summarizes the dispersive surface energy of the carbon foam samples. Foam 1 is a pristine sample before treatment and foam 2 and foam 3 are sample subsequent surface functionalization.

Table (4.3) Surface energy of the carbon foam

Sample ID	Disperse surface energy (mJ/m ²)
Foam 1	1.18
Foam 2	23.64
Foam 3	25.92

4.5 Measuring PCM properties

4.5.1 Thermal properties

The PCM used in the experiments was a low melting temperature paraffin wax. It is an alkyl hydrocarbon k-18 paraffin wax. The nearest chemical formula to this material is C₁₈H₃₈. This type of wax was selected because its melting temperature is very close to the ambient temperature, so the losses in the experimental setup would be minimal. To find out the behavior of the PCM during

the melting and freezing processes DSC measurements were performed with Mettler TA4000 thermo-analysis equipment with a liquid nitrogen cooling system. From the measurements, it was possible to determine the latent heat of fusion, the melting point, and the specific heat of the wax. The DSC heat flow versus time curve for the melting and freezing processes of the PCM is shown in Fig.(4.3). It was found that the wax melting temperature was ranging from 25.4 up to 28.9 °C. The thermal conductivity of the PCM was taken as the same as the thermal conductivity of the hydrocarbon $C_{18}H_{38}$, which was in the range of 0.15-0.25 W/mK. All the properties of the PCM are tabulated in table (4.4).

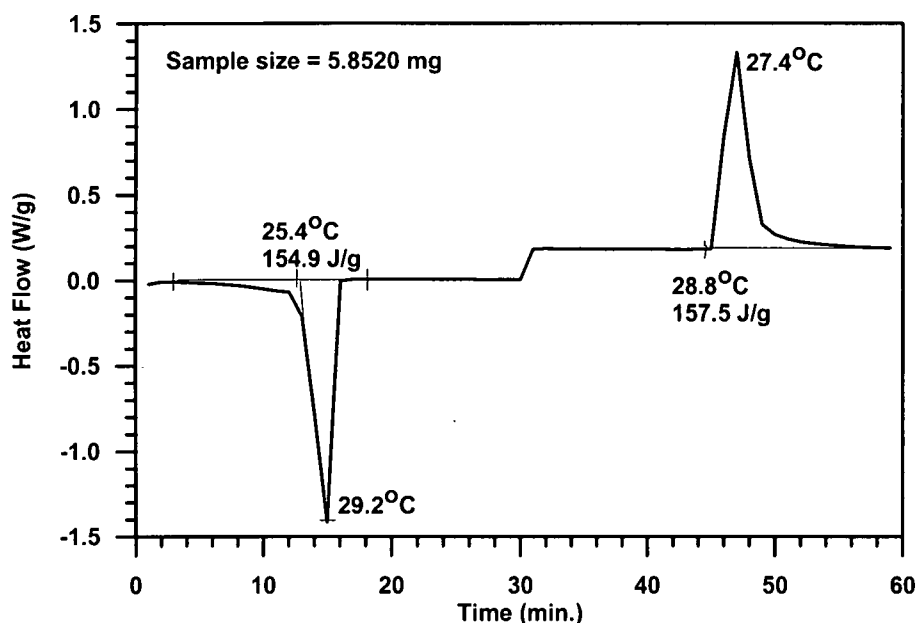


Fig. (4.3) DSC melting point and latent heat measurements

Table (4.4) Wax properties

Property	Value	Property	Value
Density [kg/m ³]	740-820	Thermal conductivity [W/mK]	0.15-0.25
Latent heat [kJ/kg]	155-157.5	Viscosity at 50 °C [cp]	3.0
Specific heat [kJ/kgK]	2.0-3.0	Thermal expansion coefficient [1/K]	1.2E-4
Melting temperature [°C]	25.5-28.9		

4.5.2 Viscosity

The viscosity of the molten liquid of the wax was measured with the Brookfield DV-III programmable Rheometer. The principle of operation of this Rheometer is to drive a spindle, which is immersed in the test fluid, through a calibrated spring. The viscous drag of the fluid against the spindle is measured by the spring deflection. The measuring range is determined by the rotational speed and the shape and size of the spindle. Two wax samples were prepared. The first sample was a pure wax and the second was a wax mixed with 3% by weight fume silicate to alter the viscosity. The viscosity was measured at different temperatures.

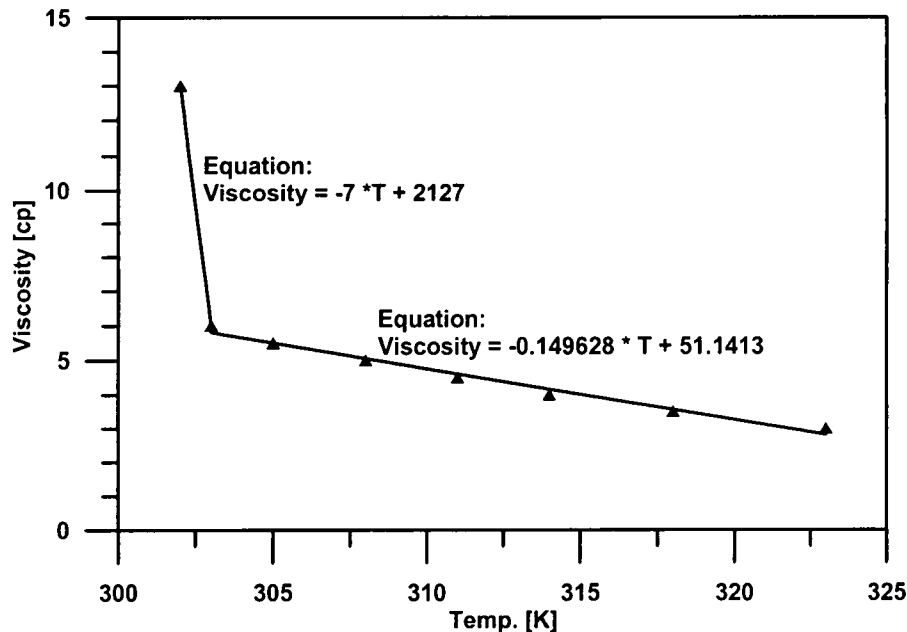


Fig. (4.4) Variation of pure wax viscosity with temperature

Figure (4.4) shows the viscosity change of pure wax with temperature. The viscosity changed linearly with temperature when it was in the purely liquid state. At temperatures near melting, when the wax started to solidify, the viscosity increased suddenly due to the formation of solid nucleates inside the wax. Two linear correlations were used to fit the experimental data, one near the melting point and the other at higher temperature. These correlations had been used in the numerical calculations. After dispersing the fume silicate into the wax, the viscosity increased by about 600%. Also, the decreasing rate of the viscosity with temperature became smaller because the viscous effect was mainly driven by the filler, the fume silicate, not by the pure material property as shown in Fig. (4.5).

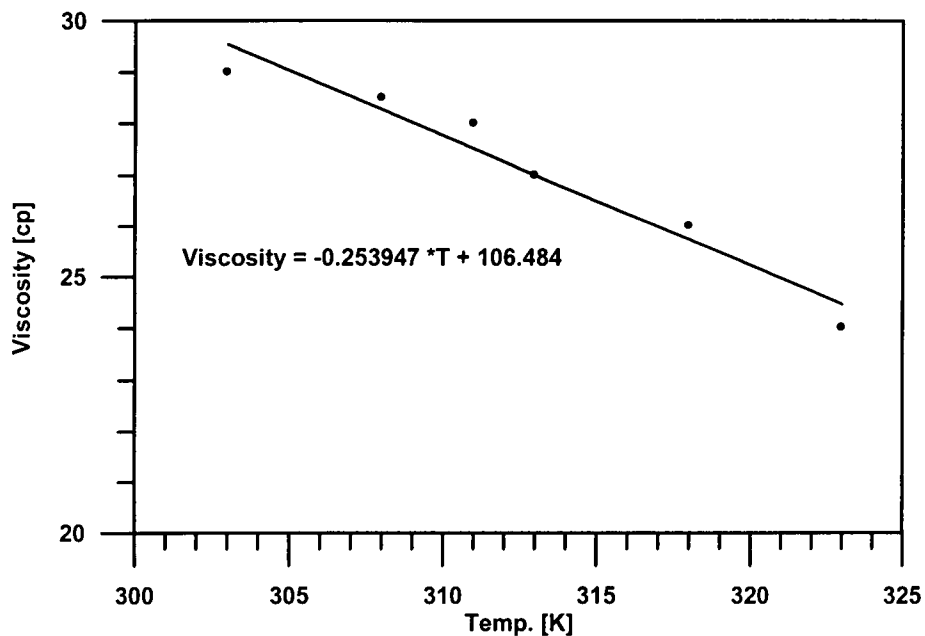


Fig. (4.5) Viscosity-temperature variations of wax with 3 % fume silicate

4.6 Enclosure manufacturing

To hold the PCM saturated foam sample and to prevent leakage during melting, a container was manufactured from plexiglass and Aluminum sheets. The four side-walls, front, rear, top, and bottom of the container were made of (7/16") thickness Plexiglass sheets to allow visual access as shown in Fig. (4.6). The sample experienced the heat source and sink from the left and right sides respectively. An aluminum plate of thickness (3/16)" is glued using a very thin silicon layer and tightened using screws to cover the container from the left side. Another Aluminum plate of thickness (1/8)" was used to cover the container from the right side. To seal the enclosure from the right side upon tightening, a thin

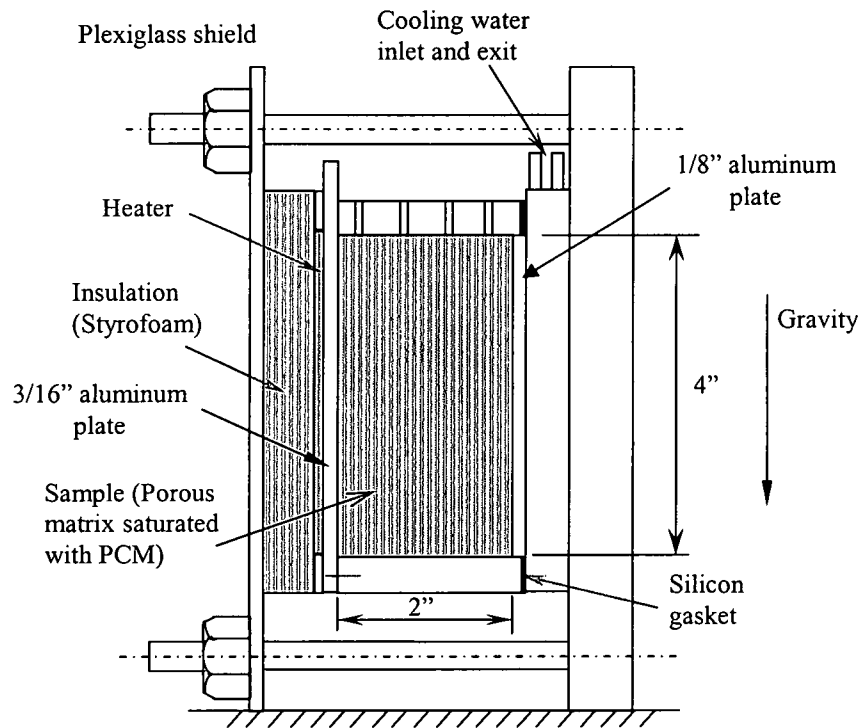


Fig. (4.6) Test rig

silicon gasket was placed between the cold plate and the plexiglass. A sufficient space was allowed at the top, and some holes were made at the top plexiglass plate to allow the expected volume change during melting, and to insert the thermocouples from the top plate into the foam material.

The heater and the cold plate were attached to the left and right aluminum plates respectively using thermal paste to minimize the thermal contact resistance. OmegaTherm highly conductive filled silicon paste (thermal conductivity = 2.5 W/mK) was used as the thermal paste. While conducting the experiments, the side-walls of the container were insulated by Styrofoam plates.

The insulation from the front side was removed for about 30 seconds for taking photos at different times through the test.

A total of 24 k-type thermocouples were used. Seven thermocouples were attached to the left side of the heater using thermal tape while five thermocouples were attached in the thermal paste layer between the right aluminum plate and the cold plate. The rest of the thermocouples were attached inside holes made in the foam material using fine plastic tubes to prevent their expected motion during the test. The thermocouples used to monitor the temperature inside the foam material were arranged in three levels; four at the top 0.66" from the top surface of the foam, four in the middle plane, and four at 0.66" from the bottom surface. The locations of all the thermocouples and their numbers, which will be used throughout this thesis, are shown in Fig. (4.7).

The thermocouple signals as well as the voltage and current going through the heater were measured using the 16 bits I/O board DT2805. An interface visual basic program was developed to acquire the data from thermocouples and record it in spreadsheet format on the computer. The thermocouple readings were sampled by a rate of 100 samples per second per channel and averaged to record a single reading. Time intervals of three seconds were set for all the data acquisition. The thermocouple readings were calibrated against a Mercury thermometer, it was found that the thermocouple readings were accurate within ± 0.2 °C in the temperature range from 0 to 100 °C.

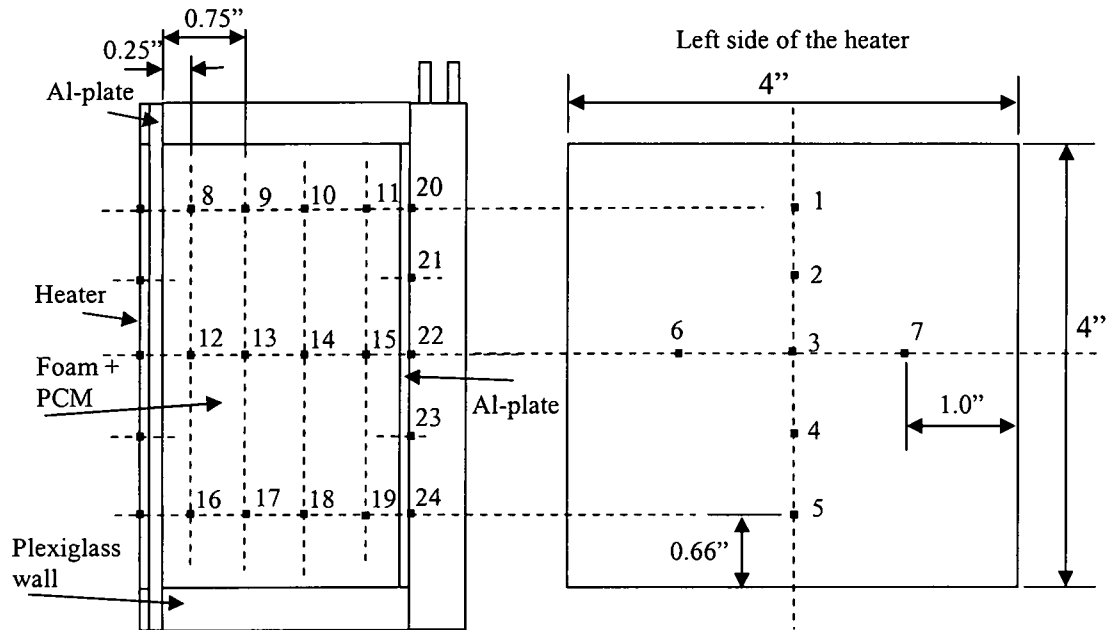


Fig. (4.7) Thermocouple locations

Before the experiment, the thermocouples at the lower plane of the foam were fixed inside the foam and the foam was placed inside the enclosure. Then the enclosure was slowly filled with molten PCM. This process was only used for aluminum foam, for carbon foam, the foam was heated and then inserted inside the wax at a temperature of $100\text{ }^{\circ}\text{C}$. The system was left to cool down and solidify and the test started when the thermocouple readings reached $18.0 \pm 0.5\text{ }^{\circ}\text{C}$. In all the experiments, the heater power supply was set to 50 percent, which produced about 28.9 Watts.

4.6.1 Visual tracing of the liquid solid interface

The liquid solid interface was traced by direct visualization. A high resolution digital camera was fixed in a suitable position in front of the test rig. After the highest temperature recorded by the thermocouples reached the

melting point of the PCM, a photo shot was taken every certain time interval. The photos were processed using Adobe-Photoshop software to extract the solid liquid interface position.

4.7 Results for Aluminum foams

The experimental results were extracted in terms of temperature-time history at different locations of the experimental setup as well as snap shots of the liquid-solid interface at selected time intervals. This data was used to validate the numerical model results. The liquid-solid interface for different aluminum foam porosity and with the same pore size is shown in Fig. (4.8). At the beginning of the melting process, a thin layer of PCM melted and this layer grew

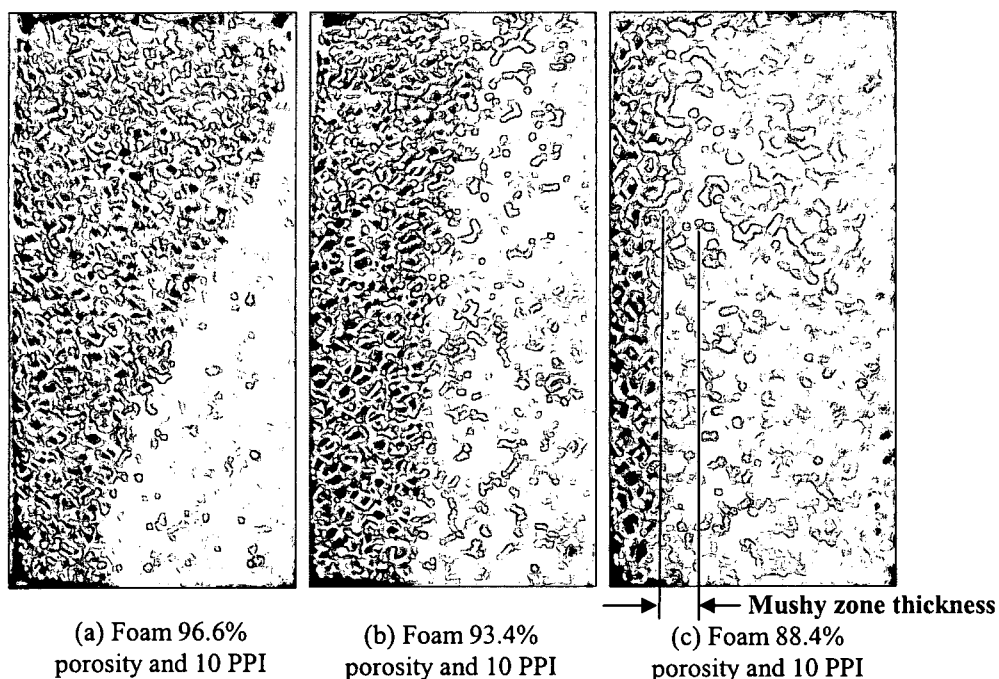


Fig. (4.8) Liquid-solid interface at time= 75 min from applying the heat for different porosity aluminum foam

thicker with time. Due to the temperature build up beside the hot surface, the hotter layer beside the hot wall moved upward due to buoyancy effect and turned to impinge on the solid liquid interface at the top region. This accelerated the melting process at the top more than at the bottom region. The lower thermal conductivity and the higher permeability of the lower density foam increased the temperature build up beside the hot surface and decreased the liquid motion resistance inside the porous structure respectively. Due to these two effects, we can see from the liquid-solid interface shape that the convection motion effect was very clear for the higher porosity foam. Conversely, for lower porosity foams the convection motion of the liquid phase became very small and the interface became nearly straight.

Another important point to be noted is, for higher density foam porosity 88.4%, the interface region became very thick. This could be noticed from the color change between the pure liquid region and the pure solid region. This happened due to the high thermal conductivity of this foam so the heat diffusion inside the foam material became faster than the heat exchange with the PCM. By examining the temperature-time history of the heater, it was found that using lower porosity foam can achieve lower heater temperature as shown in Fig. (4.9) but for the higher porosity foam, the steady state temperature was reached faster due to the higher effect of liquid phase convection motion.

Due to the fact that the permeability of the foam is directly proportional to the square of the pore size, the liquid-solid interface became more flat as the pore size decreased as shown in Fig. (4.10). The quantity of the molten wax

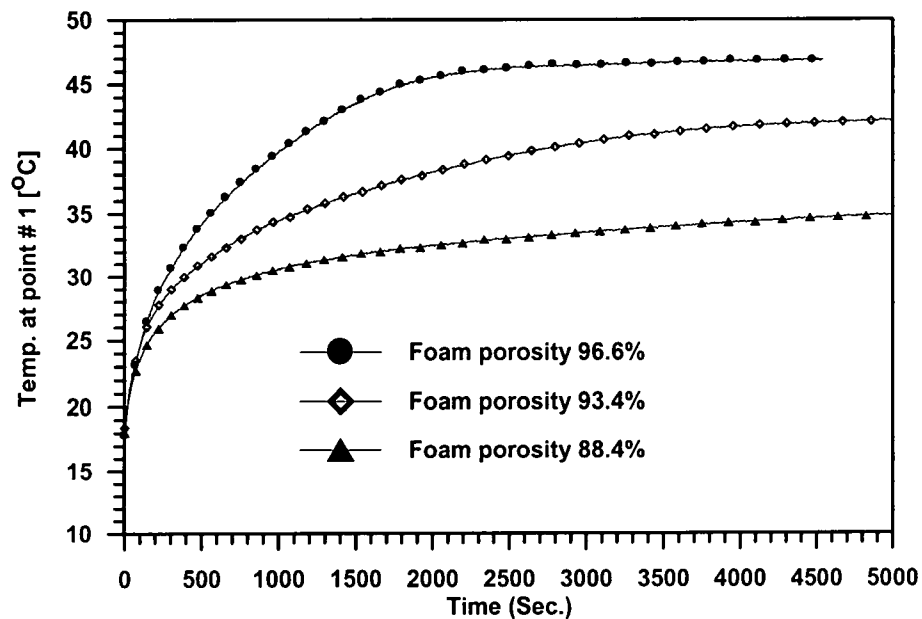
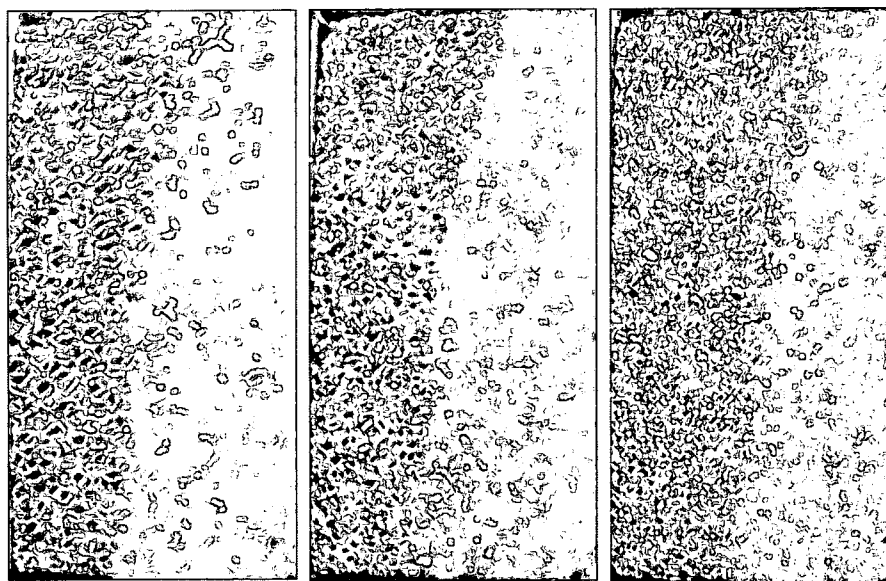


Fig. (4.9) Heater temperature-time history for different porosity Al foam



(a) Foam 93.4% porosity and 10PPI

(b) Foam 93.9% porosity and 20PPI

(c) Foam 93.7% porosity and 40PPI

Fig. (4.10) Liquid solid interface at time = 80 min from applying the heat for different pore size aluminum foams

seemed to be greater for smaller pore sizes, which means that the ability of smaller pore size foams to reject the heat generated inside the heater to the cooling plate is lower than that for larger pore size foams. At the same time, the steady state heater temperature increased with decreasing pore size for nearly the same porosity as shown in Fig. (4.11). In conclusion, we can say that, to maximize the heat transfer inside the foam we should use a combination of lower porosity with bigger pore size foams. Using this kind of foam is expected to be efficient in heat sink applications.

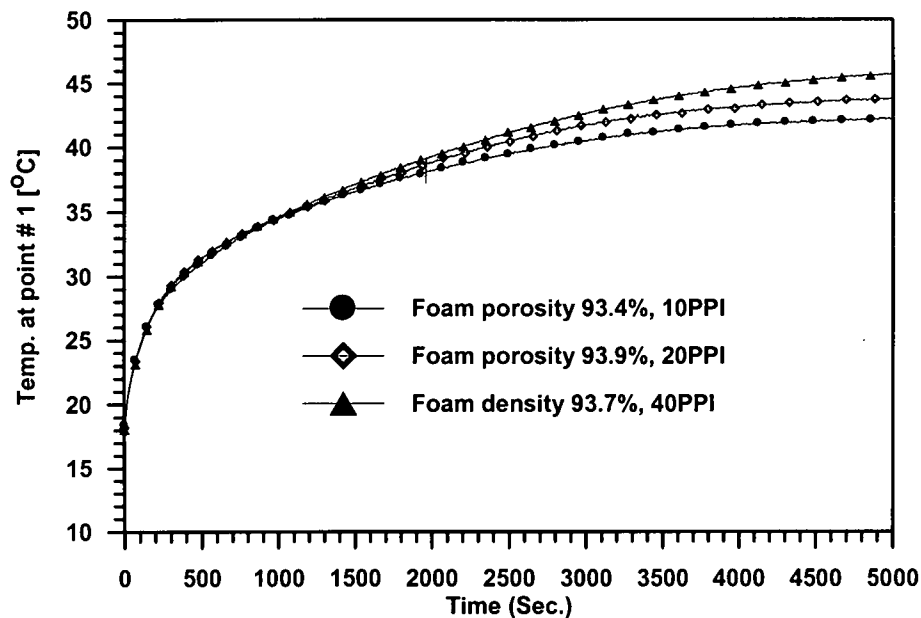


Fig. (4.11) Temperature time history for different pore size foams

Increasing the wax viscosity or decreasing foam pore size showed the same results. Reducing the pore size as mentioned before is reducing the permeability of the foam and consequently the liquid phase convection motion. Also, increasing the viscosity of the wax liquid phase increases the viscous

resistance to the liquid phase motion. This effect is clear in Figs. (4.12, 4.13). It was noticed that the liquid-solid interface became straight and the heater temperature increased for higher viscosity wax.

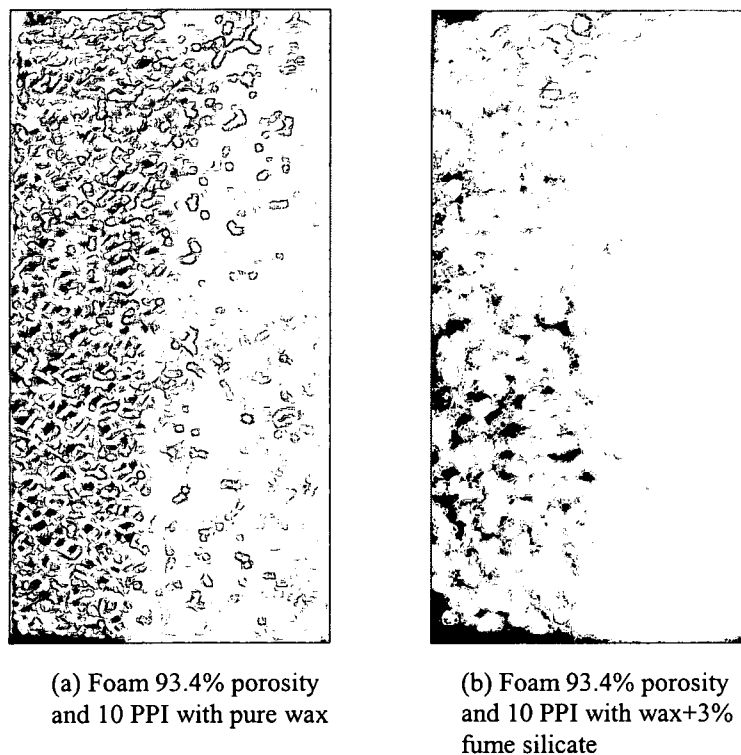


Fig. (4.12) Liquid-solid interface for aluminum foam (93.4% and 10 PPI) with different wax viscosity at time = 80 min

4.8 Results for carbon foam

Three carbon foam samples were infiltrated with wax. First, we heated the carbon sample and then inserted it in a hot wax at a temperature of 100 °C, above the wax melting point (about 70°C). We noticed that treated samples absorbed more wax than the pristine sample, and subsequent thermal conductivity was changed after surface activation.

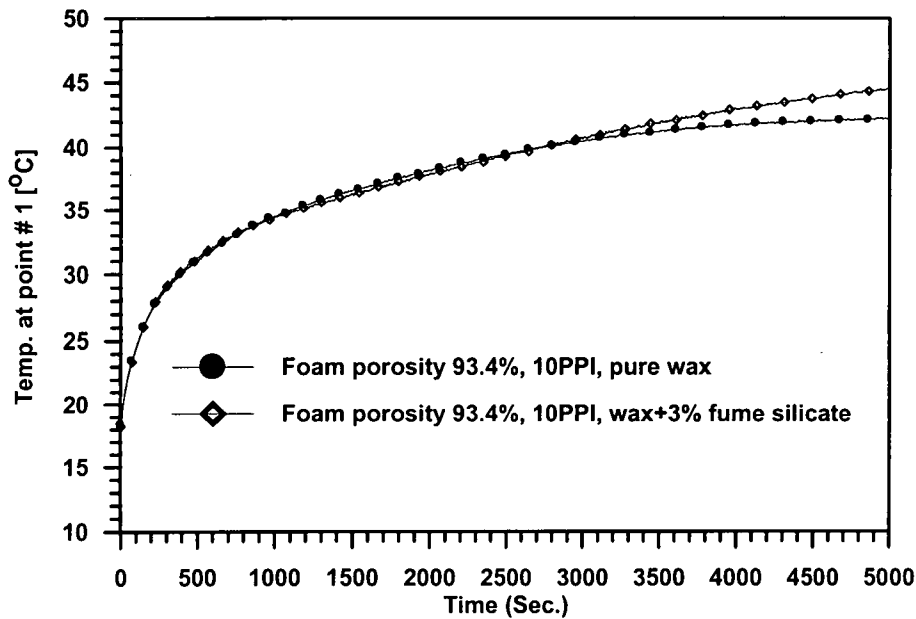


Fig. (4.13) Temperature-time history of the heater for different values of wax viscosity

Due to the change in the thermal conductivity and the absorbed quantity of wax in each sample, we normalized the temperature and calculated the Nusselt number for each case. The temperature was normalized based on the effective thermal conductivity of the carbon foam and the applied heat flux. For comparison, only the value of Nusselt number at steady state condition to normalize the change of the quantity of wax inside each sample was considered, because at a steady state condition no more melting for the PCM would occur. At steady state condition, the heat transfer inside this porous system should be affected only by the energy exchange from the carbon foam material to the PCM. The Nusselt number is defined as,

$$Nu = \frac{q''l}{k_{eff}(T - T_{init})}.$$

where l is the foam thickness, q'' is the heat flux coming from the heater, k_{eff} is the effective thermal conductivity of the foam, and T_{init} is the initial temperature.

Table (4.5) Results for Carbon foam

Sample #	Mass of wax [gm]	% increase of absorbed wax	Nu	% increase of Nu
1 (pristine)	312	0	1.298	0
2 (Treated for 1 hour)	332	6.33	1.428	10
3(Treated for 3 hours)	333	6.73	1.45	11.7

The changes in the absorbed mass of wax and the changes in Nusselt number for the three carbon foam samples are shown in table (4.5). The change in wax infiltration and Nu from sample 2 to 3 was very small compared to the change from the first to the second one. This is because after activating sample 2 the surface energy increased from 1.18 to 23.26, which was nearly equal to the surface energy of the molten wax. This can show that the enhancement due to surface activation came mainly from increasing the wettability between the two phases.

CHAPTER 5

NUMERICAL RESULTS AND PERFORMANCE OF FOAM-PCM COMPOSITE AS A HEAT SINK AND ENERGY STORAGE

5.1 Introduction

PCM and foam represent a good combination of composite materials that conduct and absorb heat. PCM absorbs heat as latent heat without significant temperature increase. On the other hand, metal or graphite foams can attain high thermal conductivity and serve as heat carriers.

In this chapter, we studied the thermal performance of PCM-foam systems in cooling and energy storage applications. For heat sinks, foam and PCM properties were considered as the design parameters. The foam properties include thermal conductivity, porosity, pore size, and surface characteristics. The PCM properties were latent heat, melting point, and viscosity of the liquid phase. In addition, design parameters such as shape, orientation, and the use of fins were included.

5.2 Numerical treatment of energy exchange between PCM and solid materials

In the numerical simulation, we used two-energy equation model. The computational domain contains both pure solid materials like the heater and

enclosure walls, beside foam saturated with PCM. A special numerical analysis was used to simulate the interactions between the solid materials and PCM. Using a one-energy equation model, PCM infiltrated foam will be treated as one material with appropriate properties. Therefore the analysis sees only different materials in contact with each other. But in our model, the solid phase of the foam and the PCM are considered as two different phases at different temperatures. In the pure solid materials such as heater or enclosure walls, the PCM phase does not exist.

To deal with this difficulty, the material type of each computational cell was marked using two flags, one for porous regions and the other for pure solid regions. If the cell lay in a porous region, its porous flag was set to one and the flag for pure solid was set to zero and vice versa. The thermal properties were set appropriately for each region based on its material type.

The numerical solution at each cell was carried out based on the cell type, solid or porous. This was implemented in the numerical solution by solving all the governing equations over the total computational domain. However, the following restrictions were considered.

- 1- Only inside the porous cells, the liquid fraction was updated and the melting-solidification source term was incorporated with the PCM phase energy equation.

- 2- The heat diffusion coefficient at the interface between any two different solid materials was taken as a harmonic mean with considering a certain contact resistance and contact thickness if it was necessary, such that:

$$k_{inter} = \frac{1}{0.5/k_{m1} + 0.5/k_{m2} + R_{contact} / R_{thick}}.$$

3- At the interface between any pure solid cell and any porous cell, an energy balance was made between the solid material and the PCM occupied inside the porous cell. This heat exchange was added to both cells as a heat source or sink.

4- In porous regions, the solid phase of the porous foam was assumed to exchange heat with the PCM through the foam interfacial surface area, $h_{sf} a_{sf} (T_{PCM} - T_s)$.

5- In solving the PCM phase energy equation for the cells located inside the pure solid regions, we set the heat coming from all the sides by diffusion or convection equal to zero. By adapting this restriction, the PCM phase temperature in the pure solid regions acts like a fictitious value, which will take the initial temperature value, and does not change throughout the solution.

6- In pure solid regions, the velocity is fixed to zero.

Regarding adjusting the velocity field of the molten liquid of the PCM beside the solid walls, the velocity component normal to any solid surface is set equal to zero. Moreover, the coefficients of the discretized momentum and pressure correction equations for the cells beside the pure solid regions were modified to account for the wall viscous effects and to insure zero pressure gradient normal to the wall.

By employing this method, the domain was made of two interacting layers (solid and PCM) with the assumption that PCM layer does not exist in the pure solid regions. The solid layer exchanged heat with the PCM layer and vice versa.

The PCM layer was considered to change its phase upon reaching its melting temperature. At the same time, the molten PCM layer could move through the porous foam.

5.3 Numerical model validation with the experimental work

In this section, the results for both the numerical simulation and the experimental work are compared with each other for melting of k-18 paraffin wax infiltrated inside aluminum foams. In the numerical solution, all the materials included in the experimental test rig were considered in the computational domain. The heater power was represented by a uniform heat generation inside the heater material. For all the cases, we assumed constant heat generation, which was (29 Watts). The left, bottom, and top boundaries of the computational domain were insulated while the right boundary was subjected to a heat convection from the cooling water ($h = 2000 \text{ W/m}^2\text{K}$ and $T_{\infty} = 13 \text{ }^{\circ}\text{C}$). All the results are shown in dimensional form for simplicity unless the normalized quantities are required to clarify any specific point.

In the experimental setup, the copper heater was glued to the left side aluminum plate of the enclosure using a thermal paste with a thermal conductivity of 2.5 W/mK . In the numerical simulation, we considered the presence of this paste layer by a thermal contact resistance of $0.0001 \text{ }^{\circ}\text{Cm}^2/\text{W}$ and contact thickness of 0.00025 m . The contact between the left and right aluminum plates of the container with the foam was considered to be in the range of $2\text{E-}4$ to $3\text{E-}4 \text{ }^{\circ}\text{Cm}^2/\text{W}$ with the same contact thickness. Because of the pore size of the aluminum foams was much larger than the thermocouple junctions,

the temperature data inside the foam was compared with the simulated temperature of the PCM phase. In the experimental work, a digital camera captured the solid-liquid interface. Picture frames of the interface were extracted and were used for the comparison. Fig.(5.1) shows the predicted and the experimental solid-liquid interface for aluminum foam of 93.4% porosity and 10 PPI. The thick lines in this figure represent the predicted mushy zones between the totally liquid PCM on the left side and the totally solid PCM on the right side while the dotted lines represent the extracted points from the pictures.

It can be observed from Fig. (5.1) that the numerical model has predicted the liquid-solid interface accurately. At the beginning of melting, the predicted interface deviated from the measured data at the top region. This could be due to the PCM volume change upon solidification. The volume change generated some vacant spaces adjacent to the container walls, which made the molten liquid to slip at the beginning of the melting process and accumulated down due to gravity.

Fig.(5.2) shows the comparison between the numerical and the experimental temperature time histories at different points. Some points are selected at the same level, having the same y coordinate. In addition, two points inside the foam material, one at the upper level and the second at the lower level, were selected to show the effect of liquid phase convection motion on the temperature field. As shown in the figure, the numerical model predicted the heater temperature with a great accuracy. However, there were small deviations between the measured and the predicted temperatures for the points inside the

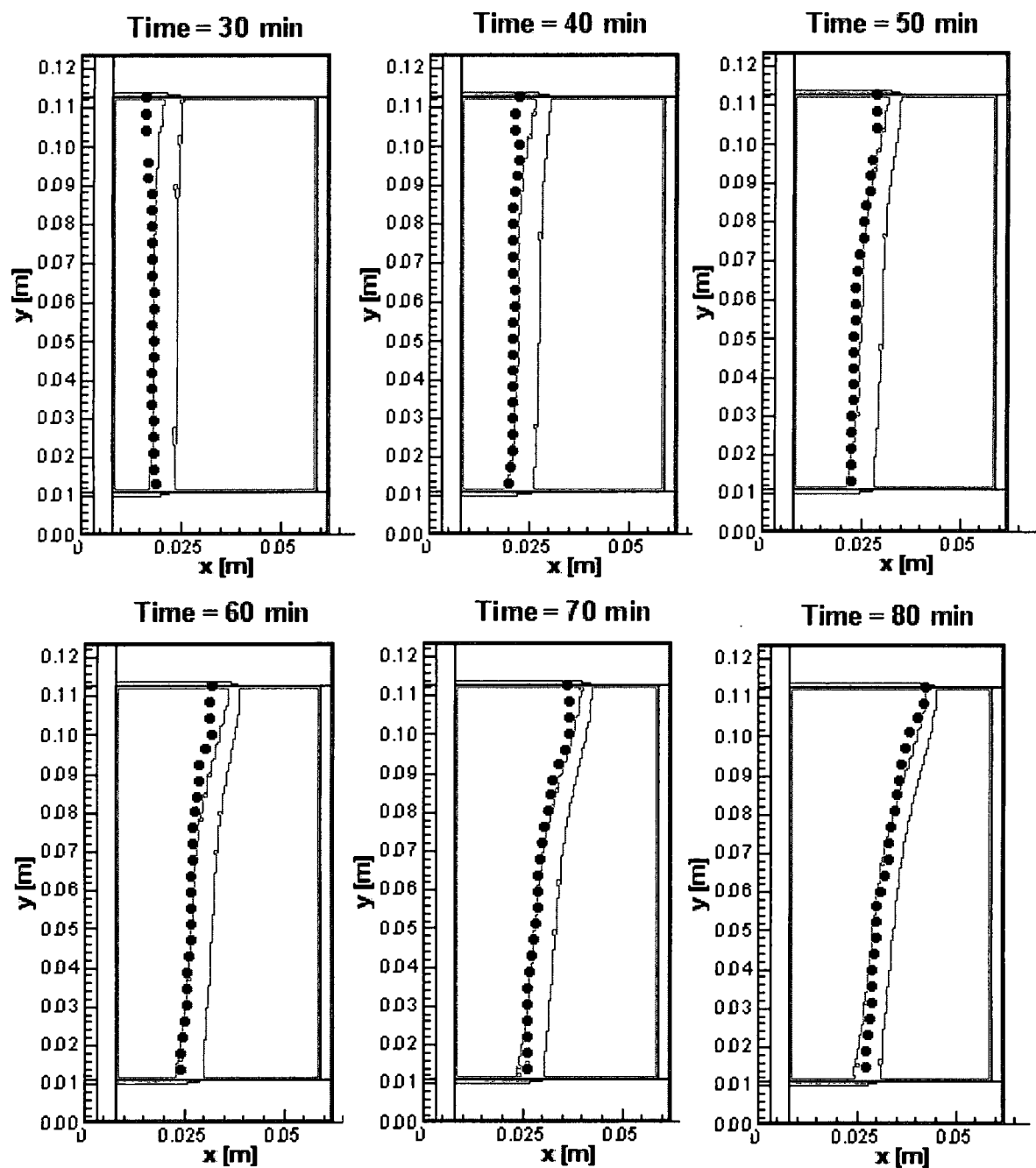


Fig. (5.1) Comparison between numerical and experimental solid liquid interface for aluminum foam 10 PPI, 93.4% porosity

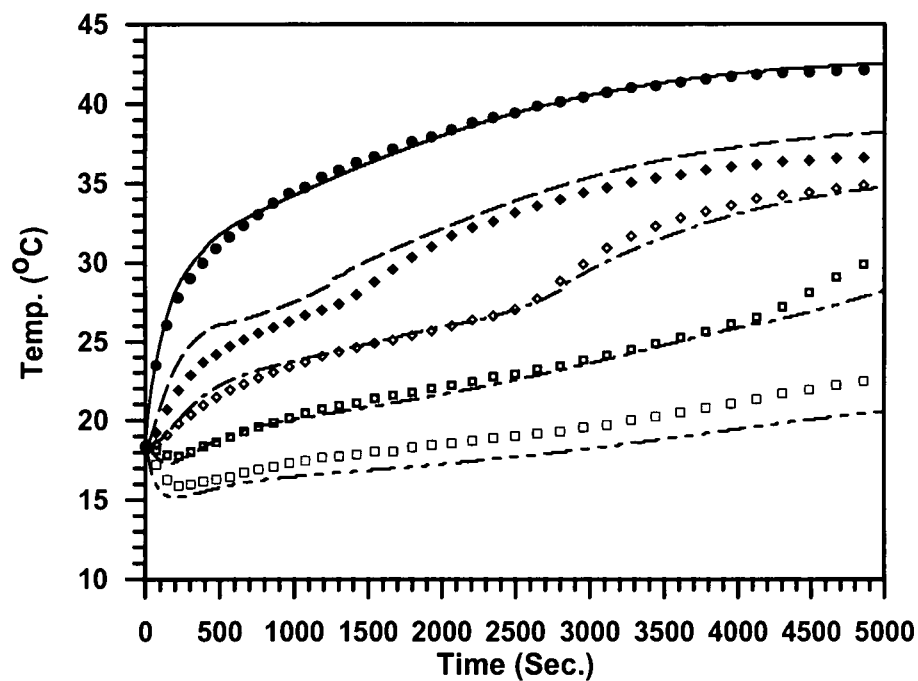
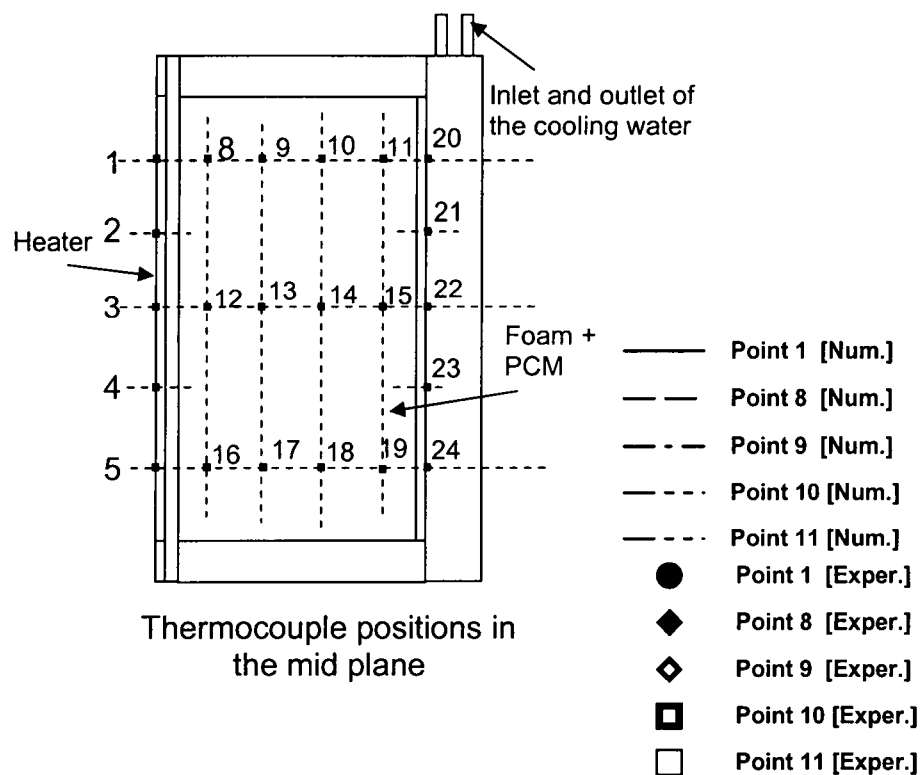


Fig. (5.2) Temperature-time history at different points at the same level

foam material. This was mainly due to the uncertainty in the thermocouple locations. The temperature at the top and the bottom levels inside the foam were very close to each other at the beginning of the melting process. After elapsing 2000 seconds, they started to deviate from each other due to the convection motion of the liquid phase as shown in Fig. (5.3).

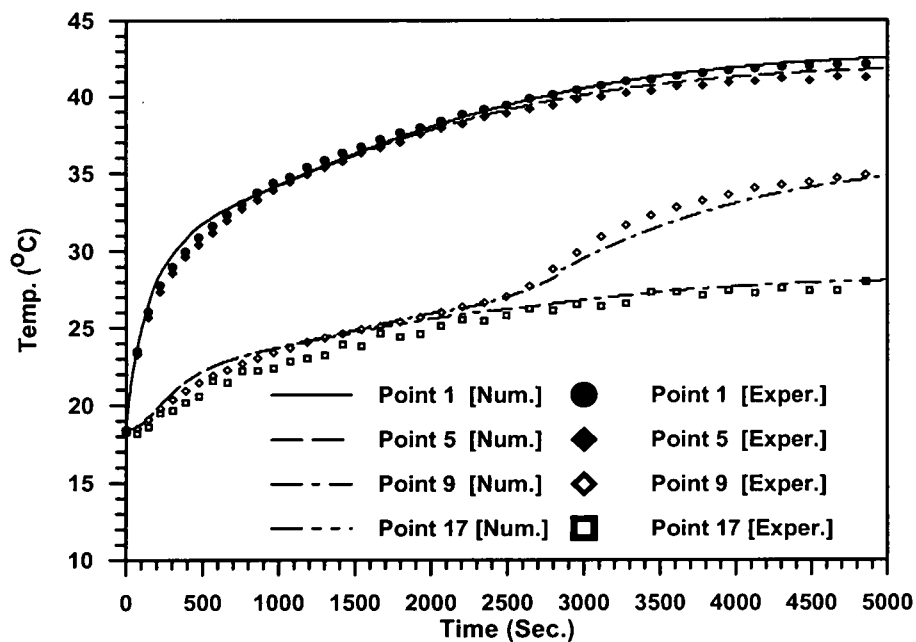


Fig. (5.3) Temperature time history at different points in different levels

After verifying the numerical results for a specific foam, 10PPI (pore per inch) and 93.4% porosity aluminum foam, it was important to check the validity of the numerical technique for different cases. In our validations, we tried to examine the performance of the numerical simulation for all the available experimental data for aluminum foams. The pore size of the foam was changed

from 10PPI to 40 PPI while the porosity of the foam was changed from 96.6% up to 88.4%.

Figure (5.4) shows the effect of changing the pore size on the heater temperature. The heater showed higher steady state temperature in the case of using foams with smaller pore size due to the sharp decrease in the foam's permeability. Both the experimental and numerical results followed the same trend.

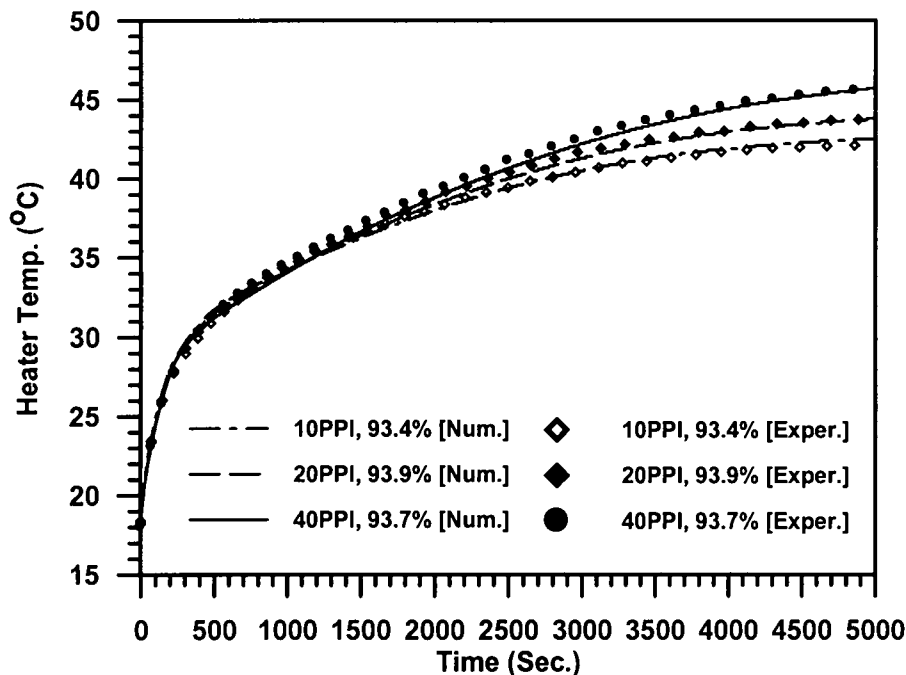


Fig. (5.4) Effect of changing pore size of the foam on steady state heater temperature

Although the smaller pore size foam (40PPI) showed lower thermal conductivity, the heater temperature for this foam was nearly the same or a little bit lower at the beginning of the melting process. We noticed this point in the experimental results. To investigate this point, the heater temperature was

normalized based on the heat flux from the heater and the effective thermal conductivity of the foam as,

$$\theta = \frac{(T - T_{\text{initial}})k_{\text{seff}}}{q''L}.$$

The non-dimensional temperature for the heater was plotted against the Fourier number at the beginning of the melting process as shown in Fig. (5.5). Both the experimental and numerical results showed that the smaller pore size foam kept the temperature of the heater lower. We do believe that this was due to the higher surface area of the smaller pore size foams. The higher surface area of the foam means higher interfacial heat exchange between the PCM phase and the foam solid material. But, after the convection motion of the liquid phase started to appear at later times, it dominated this effect and it kept the heater temperature for the bigger pore size foam lower.

Changing the metal foam porosity affects both its thermal conductivity and permeability. Figure (5.6) shows the temperature time history of the heater for different porosity Aluminum foams. Denser foams reduced the heater temperature due to their higher thermal conductivity. The steady state heater temperature has decreased by more than 10 °C by decreasing the porosity from 96.6% to 88.4%. Due to the higher permeability and the lower thermal conductivity of the higher porosity foams, the effect of convection motion of the

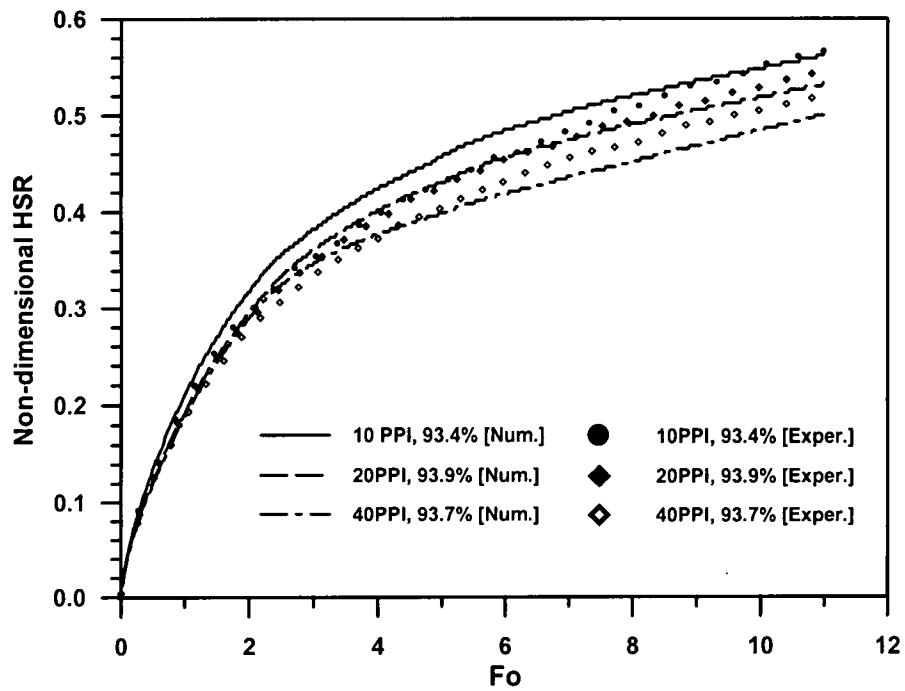


Fig. (5.5) Non-dimensional temperature against Fourier Number at the beginning of melting

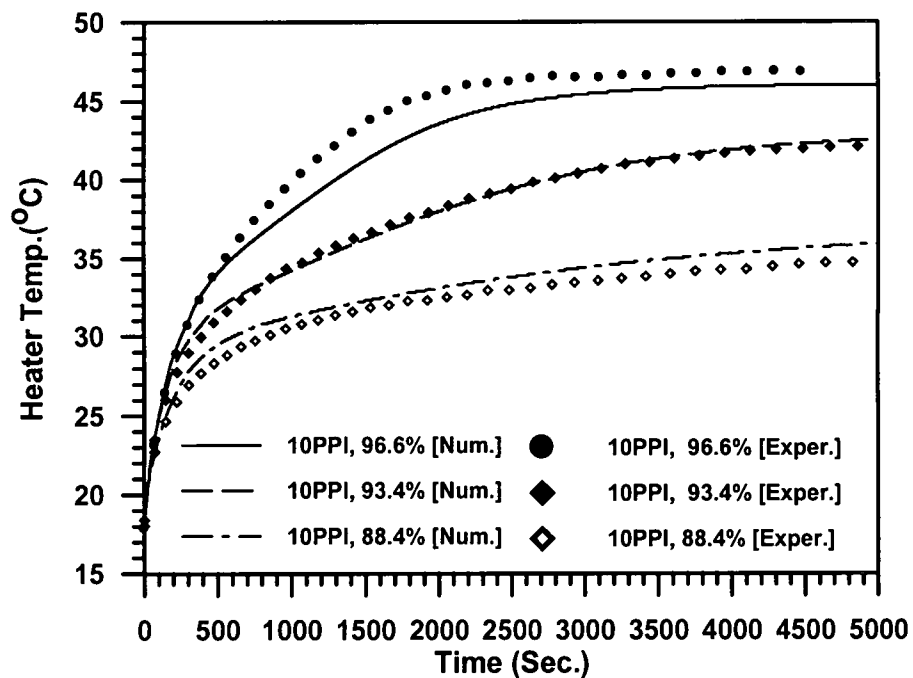


Fig. (5.6) Effect of porosity on the steady state heater temperature

liquid phase was stronger. This made the temperature of the heater to reach the steady state faster for higher porosity foams as shown in Fig. (5.6).

As mentioned in the experimental work, the viscosity of the wax was altered by doping a small percentage of fume silicate inside the wax. In the numerical simulation, the viscosity was changed from an average value of 4 cp to 28 cp. Figure (5.7) shows the comparison between the measured and the predicted heater temperatures for the two cases. Because the convection motion will be stronger for lower viscosity wax since higher viscosity needs more driving force to move the molten PCM inside the porous media, the steady state heater temperature showed lower value for the lower viscosity wax. At the same time, the liquid-solid interfaces for different viscosity values matched very well with the experimental results as shown in Fig. (5.8).

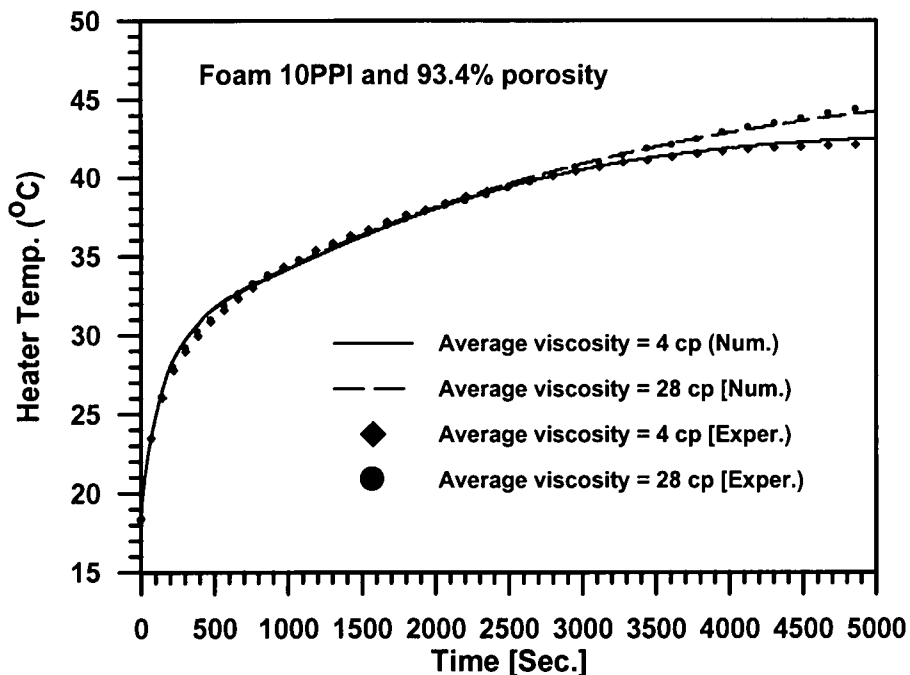


Fig. (5.7) Heater temperature for different wax viscosity

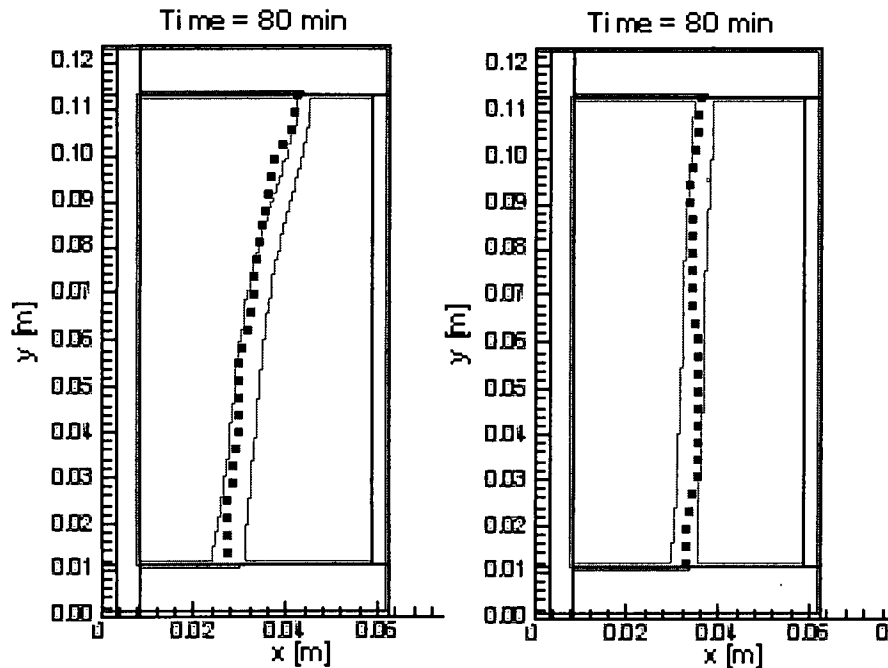


Fig. (5.8) Solid liquid interface for wax viscosity

Form the previous results, we can conclude that increasing the viscosity or decreasing the pore size have the same effect. This is because both of them increase the flow damping Darcy source term in the momentum equations, $(-\mu u/K)$, either by increasing the viscosity or by decreasing the permeability in the case of using smaller pore size foam.

From the previous comparison between the numerical prediction and the experimental measurements, it can be concluded that the numerical simulation based on our assumptions and the numerical procedures has predicted the temperature and liquid fraction fields accurately. In the light of these results, we decided that all the further studies will be carried out numerically.

5.4 Heat sink

Heat sinks are devices used to enhance the heat dissipation from a hot surface, usually the case of a heat-generating component, to a cooler ambient air. In most situations, heat transfer across the interface between the solid surface and the coolant air is the least efficient within the system, and the solid-air interface represents the greatest barrier for the heat dissipation. A heat sink lowers this barrier mainly by increasing the surface area that is in direct contact with the coolant. This allows more heat to be dissipated and/or lowers the device operating temperature. High performance heat sinks must satisfy several conditions. These conditions include high surface heat transfer, high thermal conductivity of its material, good aerodynamics, and good contact with the heating source. The heat sink's performance can be measured in terms of the Heat Sink Resistance (HSR), which is defined as the maximum temperature rise per unit input power. The common basic types of the heat sinks are: natural convective and forced convective. Typical values of HSR for natural convective range from 0.5°C/W to 5°C/W and forced convective from 0.02°C/W to 0.5°C/W .

Phase change materials can be used effectively in the design of heat sinks. The PCM heat sinks work efficiently in transient thermal control for space batteries, pulsed-power devices and re-entry thermal protection systems. Their advantages are: high heat capacity, lower weight compared to the traditional heat sinks, and compact & reliable. However, PCM heat sinks have poor conductivity.

5.4.1 Design parameters of the Foam-PCM heat sink

A heat sink consisting of a high thermal conductivity foam (Aluminum or carbon) saturated with a PCM as shown in Fig.(5.9) was considered. The heating source was an electronic chip brazed to an Aluminum substrate. A thin Aluminum enclosure was attached to the substrate to contain the foam with the PCM. To enhance the convective heat transfer from the surface, extended fins were attached to the heat sink enclosure. The heat transfer coefficient from the enclosure walls depends on the cooling system and the number of the attached fins. A suitable value was assumed, ($200 \text{ W/m}^2\text{K}$), although the actual magnitude is something arbitrary.

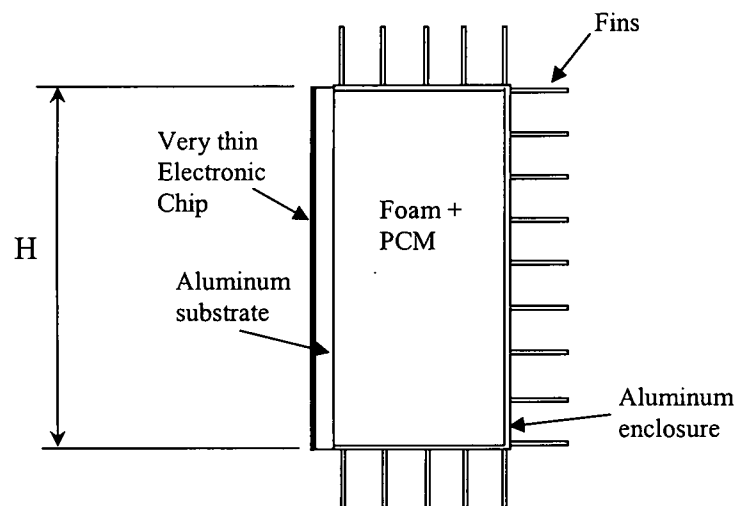


Fig. (5.9) Physical domain of the heat sink

Due to the small thickness of the real electronic chip, its heat capacity was neglected and the internal heat generation was replaced by a heat flux at the aluminum substrate surface. The foam material was assumed to be in good

contact with the enclosure walls and with the substrate. The dimensions of the heat sink were assumed to be 10 cm in height and 5 cm in width. In the case of applying steady heat generation, a 100 W heat source was assumed, which is comparable with the power generated from a high-energy power electronic chip. Ecosane was used as the PCM. Its melting temperature is 36°C. All the properties of this PCM are listed in Table (5.1).

Table (5.1) PCM properties for the heat sink

Property		Property	
T_m [°C]	36	ρ [kg/m ³]	769
k [W/mK]	0.15-0.2	L [kJ/kg]	247.3
μ [kg/m sec]	0.00415	β [1/K]	0.00085
c_p [J/kg K]	2460		

The substrate and the thin aluminum enclosure that contained the foam-PCM composite were included in the computational domain. In the case of applying pulsed heat generation, the heat source power was assumed to fluctuate like a step function between a minimum and a maximum value. Different design parameters were studied such as foam properties (porosity, pore size, thermal conductivity, and surface characteristics), heat sink shape, heat sink orientation, and use of internal fins inside the foam-PCM composite.

5.4.2 Steady heat generation

For steady heat generation, the results of the heat sink design are shown in terms of the percentage of improving the Heat Sink Resistance (HSR). The lower value means better performance. Moreover, the temperature and liquid fraction contours are shown if it is necessary for clarification.

Fig.(5.10) shows the temperature contours for both of the PCM and foam materials. This case corresponded to the use of aluminum foam of porosity 94% and 10 PPI while considering $h_{sf}=200 \text{ W/m}^2\text{K}$. It can be observed from the figure that the PCM temperature deviated from the foam temperature, which means that the heat transfer was far away from local thermal equilibrium. The heat diffused faster inside the foam material while the solid-liquid interface acted as a thermal barrier. This prevented the heat from diffusing inside the solid PCM

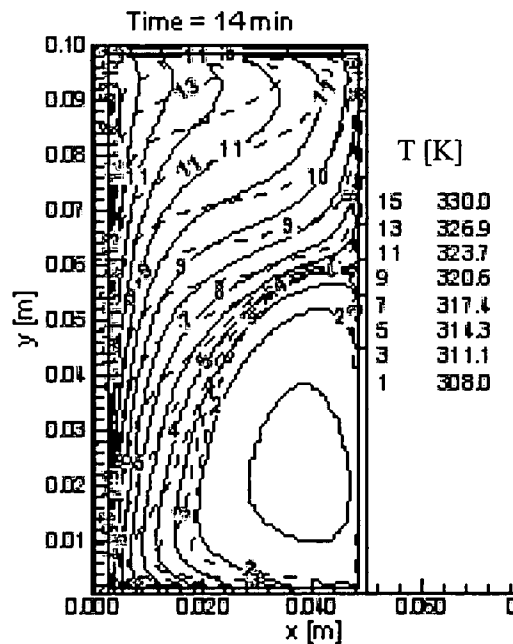


Fig. (5.10) PCM and solid phase temperature contours
Continuous (solid), Dotted (PCM)

region. At the same time, the hot PCM liquid phase beside the heating source moved to the top region due to the buoyancy forces. The PCM temperature was higher beside the hot substrate and at the top region of the heat sink while the solid temperature was higher beside the right wall and at the bottom region of the heat sink.

The heat exchange between the two phases made the solid temperature to follow the same pattern as the PCM phase. The resulting HSR for steady heat generation ranged from 0.34 to 0.404. The temperature time history at three different locations at the substrate is shown in Fig. (5.11). In the following section, the effect of changing the foam parameters on the maximum temperature of the junction between the aluminum substrate and the chip will be illustrated.

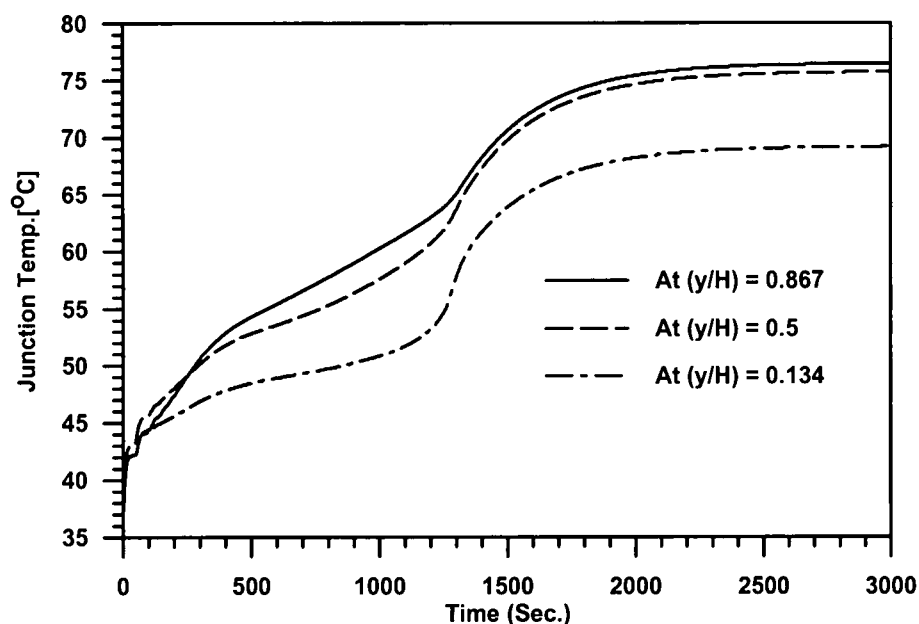


Fig. (5.11) Temperature time history at different point in the junction for Al foam (porosity =94%, and Pore size= 10PPI)

5.4.2.1 Changing foam porosity, pore size, and interfacial heat transfer coefficient

The test rig data showed that the most important foam parameters, which can affect the heat sink performance, are the foam thermal conductivity, pore size, and the interfacial heat transfer coefficient between the foam and the PCM. Foam effective thermal conductivity depends on foam porosity while permeability depends on both the porosity and pore size. The interfacial heat transfer coefficient can be related to PCM-foam wettability.

The porosity was changed from 88% to 97%, which is the maximum value that Aluminum foam can attain. The pore size was changed from 0.0012 m (corresponding to 40PPI) to 0.00434 m (corresponding to 5PPI). Only one parameter is allowed to change, the pore size is kept constant while the porosity changed and vice versa.

Maximum junction temperature-time history for using different foam porosity, pore size, and interfacial heat transfer coefficient are shown in Figs. (5.12-5.14) while Table (5.2) summarizes the HSR for the heat sink and the percentage of change of the HSR. Some of the following observations can be noticed:

- 1- Decreasing the porosity from 97% to 90% decreased the HSR but decreasing porosity from 90% to 88% did not make a significant difference. This occurred due to the reduction in liquid motion in low porosity foam.

- 2- For the same foam porosity, changing the pore size created a significant change in the HSR. Changing the pore size from 5PPI to 40PPI showed more than 7.5 percent change in HSR, which can only be achieved by changing the porosity from 97 to 88 %. This means that by using high pore size foam we can save about 11% of the foam material weight.
- 3- Changing the interfacial heat transfer coefficient by ten times can improve the performance by 5%. But we noticed that after increasing h_{sf} over 500, the change in HSR became negligible. This is because at this high value of h_{sf} the PCM and solid foam reaches local thermal equilibrium ($T_s = T_{pcm}$), which means that any further increase in h_{sf} can not make any difference.

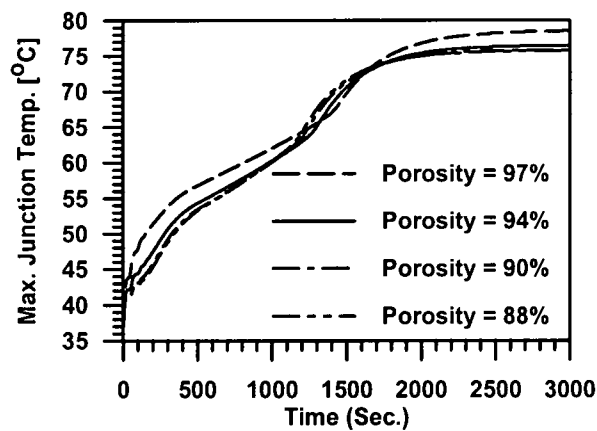


Fig. (5.12) Maximum junction temperature for different foam porosity

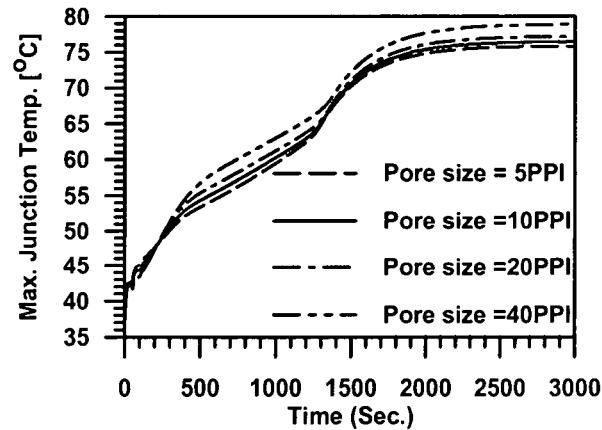


Fig. (5.13) Maximum junction temperature for different foam pore size

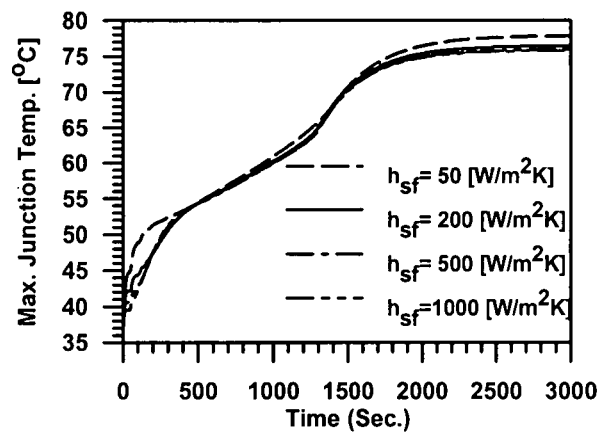


Fig. (5.14) Maximum junction temperature for different interfacial heat transfer coefficient

5.4.2.2 Adding fins

Using fins can alter the spreading of the heat inside the heat sink. In this design study, we checked the effect of adding one or two internal fins inside the porous matrix. In the case of adding one fin, a 3 mm thickness fin was attached to the substrate. In the case of using two fins, each fin thickness was assumed to be 1.5 mm to keep the same extra weight to the system constant. The presence of the fins influenced the temperature field inside the heat sink significantly as

Table (5.2) Changing of HSR for different foam properties

Change	HSR	% of change of HSR
(97%, 10PPI, hsf=200)	0.425	-5.2
(94%, 10PPI, hsf=200), Base case	0.404	0
(90%, 10PPI, hsf=200)	0.398	1.485
(88%, 10PPI, hsf=200)	0.397	1.7326
(94%, 5PPI, hsf=200)	0.398	1.485
(94%, 20PPI, hsf=200)	0.411	-2.475
(94%, 40PPI, hsf=200)	0.429	-6.188
(94%, 10PPI, hsf=50)	0.418	-3.465
(94%, 10PPI, hsf=500)	0.4	1.0
(94%, 10PPI, hsf=1000)	0.398	1.485

shown from the PCM temperature contours in Figs.(5.15). It was found that the heat diffusion was enhanced by inserting these supporting fins especially at the early times of the melting process, during conduction heat transfer mode. However, increasing the number of the fins from one to two did not lead to a significant difference on the steady state junction temperature. As shown in Fig. (5.16), adding fins can enhance the heat sink performance but increasing the number of these fins can deteriorate the performance by suppressing the liquid phase convection motion.

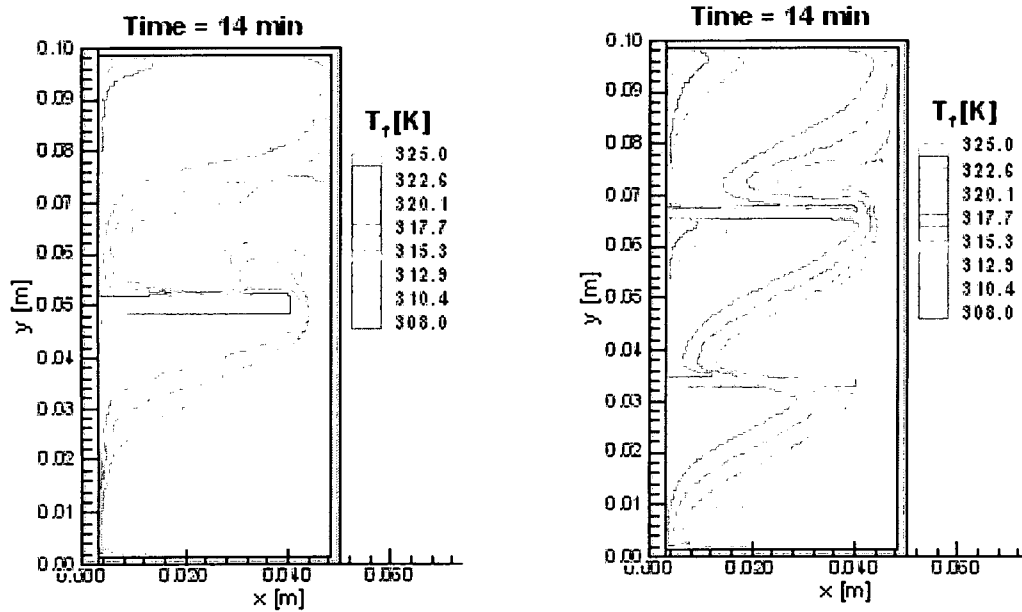


Fig. (5.15) PCM temperature contours for a heat sink supported with one and two fins

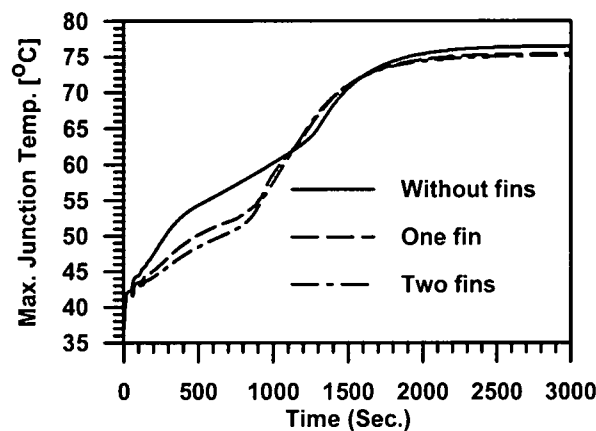


Fig. (5.16) Maximum junction temperature for using fins

5.4.2.3 Changing shape and orientation

The utilized metal foams had high porosity and big pore size. Consequently, the convection motion of liquid PCM caused the temperature field inside the heat sink to take a specific pattern based on the heat sink orientation. For the upright position in which the heat source was glued to the left side while

the gravity was in the negative y direction, we noticed that the hot region was concentrated at the top region of the heat sink. So, we suggested to change the shape of the heat sink by increasing the width of the top edge and decreasing the bottom edge. The volume of the heat sink was kept constant, as the rectangular shape.

Figure (5.17) shows the PCM temperature contours after 8 minutes from applying the heat source for different angles of the right side of the heat sink enclosure while Figs. (5-18, 5-19) show the temperature contours for different heat sink orientations, heating from bottom and top. The temperature contours took the same pattern in the case of changing the inclination angle of the right side like the rectangular case but by changing the heat sink orientation the temperature contours became completely different. In the case of heating from the bottom side, small Benard convection cells appeared. These cells merged with each other to make bigger ones as the melting process proceeded. At the end of melting, after all the PCM converted to liquid, only one big cell appeared. For heating from the top side, the temperature contours were straight, exactly like the pure conduction case except that the temperature showed higher values beside the metal enclosure wall.

Fig. (5-21) shows the effect of changing the heat sink shape and orientation on the maximum junction temperature. The calculated HSR values for the case of adding fins, changing shape, and changing the orientation are listed in Table (5.3). It is obvious that changing orientation created the biggest effect

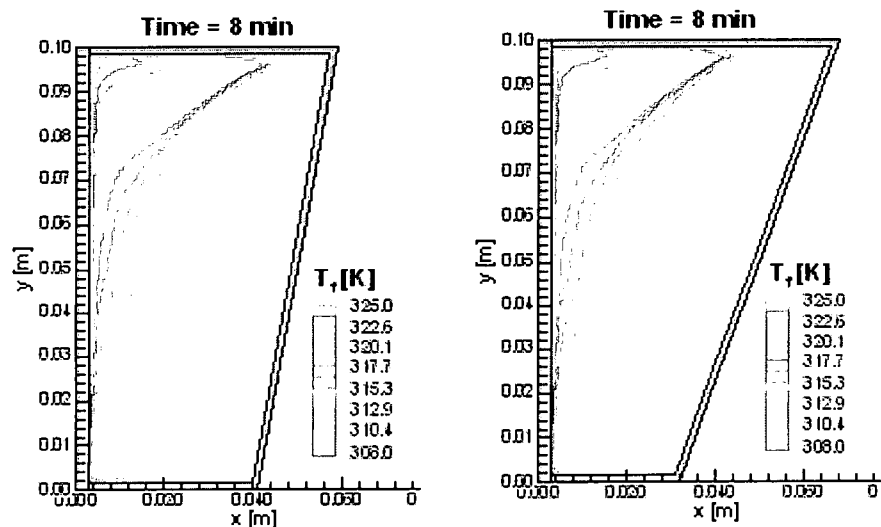


Fig. (5.17) PCM phase temperature contours for different angles (80°, and 70°)

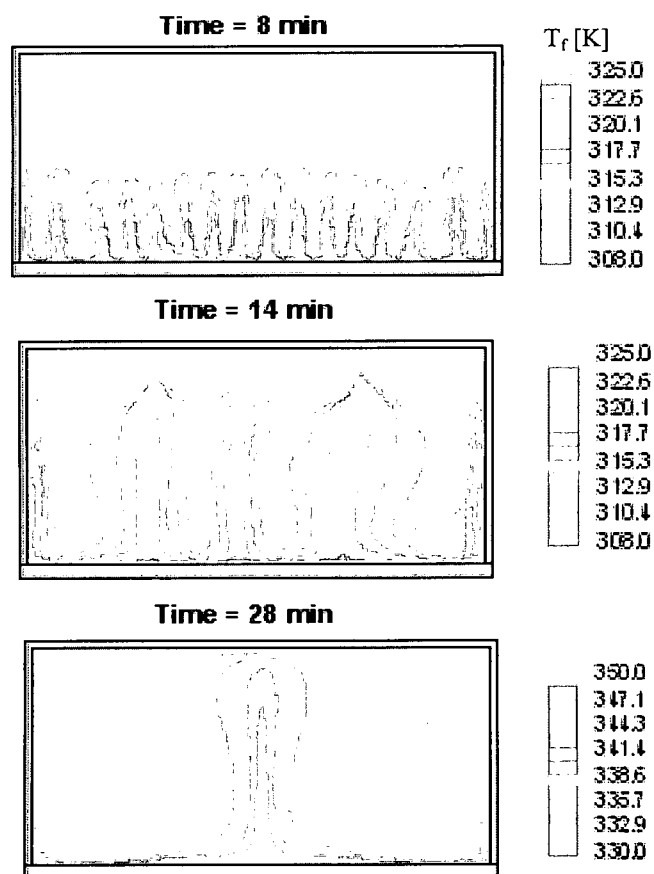


Fig. (5.18) PCM phase temperature contours for bottom heating

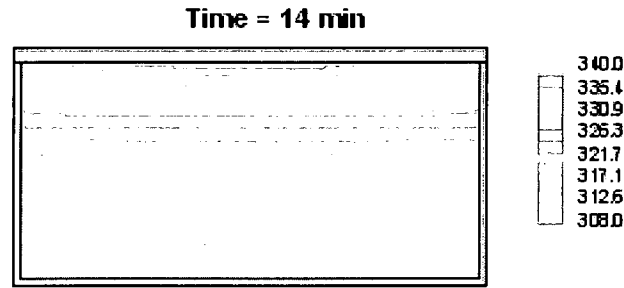


Fig. (5.19) PCM phase temperature contours for top heating

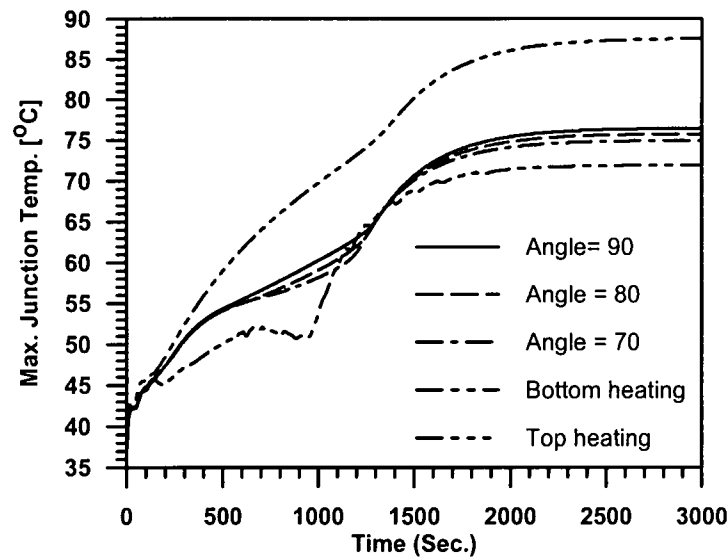


Fig. (5.20) Maximum junction temperature for different shapes and orientations

on the heat sink performance. The difference in the HSR for top and bottom heating was greater than 27%.

5.4.3 Performance for fluctuating power generation

The PCM played the role of a temperature damper in the heat sink, which was subjected to fluctuating heat generation. The key parameters that define the performance of the temperature damping effect of the PCM are the melting point

Table (5.3) HSR for adding fins and changing shape and orientation

Case	HSR	% of improvement
One fin	0.394	2.475
Two fins	0.391	3.217
Angle 80	0.397	1.733
Angle 70	0.389	3.713
Bottom heating	0.359	11.14
Top heating	0.471	-16.58

and the latent heat. The melting point defines the starting point of energy absorption as a latent heat while the latent heat defines the capacity of the energy storage. In this section, we investigated the effect of changing the PCM melting temperature and latent heat on a heat sink performance subjected to periodic spikes of heat generation. The generated heat ranged from a minimum

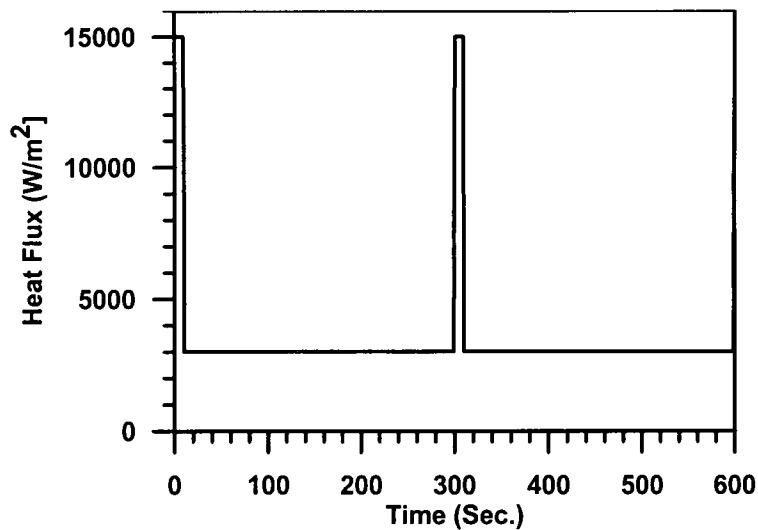


Fig. (5.21) Heat flux at the left side for fluctuating energy

value of 30 Watt to generated energy spikes of 150 Watt, which lasted for 10 seconds and repeated every 300 seconds as shown in Fig. (5.21).

The latent heat was changed from 150 kJ/kg to 250 kJ/kg and the melting temperature was changed from 36 °C, which was just above the ambient temperature by 0.5 degree to 45 °C. As shown from Figs. (5.22, 5.23), the junction temperature for both of the cases followed the same frequency as the applied heat flux. Using the higher latent heat and the lower melting temperature PCM resulted in lower junction temperature. This result was expected because

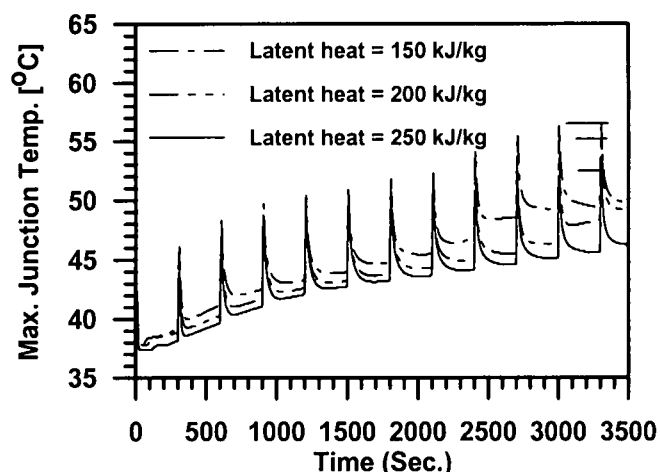


Fig. (5.22) Maximum junction temperature for different latent heat

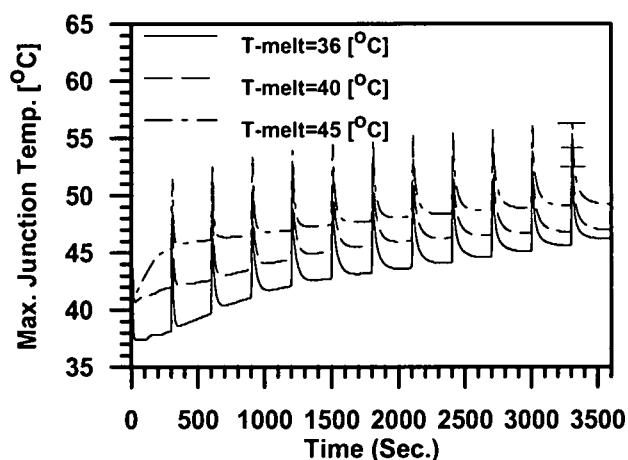


Fig. (5.23) Maximum junction temperature for different melting temperature

the lower the melting temperature the sooner the latent heat will participate in damping the temperature, and higher latent heat will produce a higher damping effect. It seems that using PCMs in heat sink designs is a very effective solution especially when the system experiences various levels of energy spikes. As shown in table (5.4), the calculated HSR based on the maximum power ranged from 0.108 to 0.136 °C/Watt while it was about 0.404 °C/Watt for the steady heat generation case. This was due to the heat absorption inside the PCM as a latent heat during the energy spike period and the release of it again during the minimum heat generation period.

Table (5.4) HSR for fluctuating heat generation

Case	HSR based on the Max. Power	% of improvement compared to steady heat generation
T _m =36, L=250 kJ/kg	0.1086	73
T _m =46, L=250 kJ/kg	0.136	66.3
T _m =36, L=150 kJ/kg	0.1375	65.9

5.5 Energy storage

Solid-liquid PCM energy storage stores energy in both sensible and latent heat forms. Initially, these solid-liquid PCMs perform like conventional storage materials; their temperatures rise as they absorb heat. Unlike conventional (sensible) storage materials, when the PCM reaches the temperature at which

they change phase (their melting point) they absorb large amounts of heat without getting hotter. When the ambient temperature around the PCM drops, the PCM solidifies, releasing its stored latent heat. Within the human comfort range of 68° to 86°F (20° to 30°C), latent thermal storage materials are very effective. They can store 5 to 14 times more heat per unit volume than sensible storage materials such as water, masonry, or rock. PCM energy storage can be used in solar domestic hot water heating or passive solar space heating systems. PCMs are usually more expensive than conventional heat storage materials. However, different PCMs are available such as Glauber's salt (sodium sulfate decahydrate), calcium chloride hexahydrate, and paraffin waxes.

Using PCMs in energy storage in space applications is very useful due to their higher energy to weight ratio. Space applications require using high melting temperature PCMs. One of the most interesting designs is a solar receiver with a cylindrical cavity, the walls of which are lined with a series of hermetically sealed Haynes 188 containment canisters. The canisters are filled with a high melting temperature PCM and stacked to the working fluid tube, as shown in Fig. (5.24). Using individual canisters in this design makes the design very reliable such that failure of a canister will affect only that individual canister itself. The most important factor in the design of such a solar heat receiver is the heat absorption rate or the storage response since the heat will be stored only during the specific time of sun exposure before eclipse.

5. 5.1 Effect of using carbon foam for space applications

In this section, we investigated the effect of using high thermal conductivity carbon foams to support the high melting temperature PCM on the

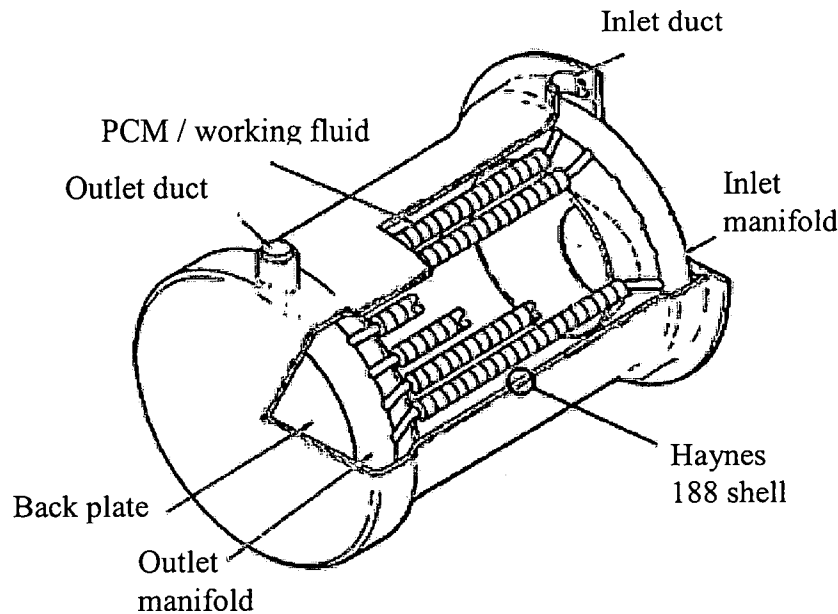


Fig. (5.24) Solar receiver [109, 110]

solar receiver output power. The space between the outer and inner tubes of each canister was filled with carbon foam saturated with LiF-CaF_2 as the PCM. The melting temperature of this PCM is about 767°C . All the properties of this material are listed in Table (5.5). The configuration and the dimensions of one canister are shown in Fig. (5.25). Convection motion of the molten PCM inside the foam is not considered in this case since the gravity in space could be neglected.

The heat delivered to the solar receiver was considered as a periodic radiation coming from the outer shell of the receiver. In the real case, this shell is

subjected to a solar collector that provides the energy during the period of the sun exposure. The period of the sun exposure and eclipse was 40 minutes, 20 minutes exposure and 20 minutes eclipse. During the period of the sun exposure, the outer shell of the receiver was assumed to be at a constant temperature

Table (5.5) High melting temperature PCM (LiF-CaF₂) properties [109]

Property		Property	
T_m [°C]	767	ρ [kg/m ³]	2590
K [W/mK]	3.8 – 1.7	L [kJ/kg]	816.0
μ [kg/m sec]	0.0023	β [1/K]	0.000287
c_p [J/kg K]	1770		

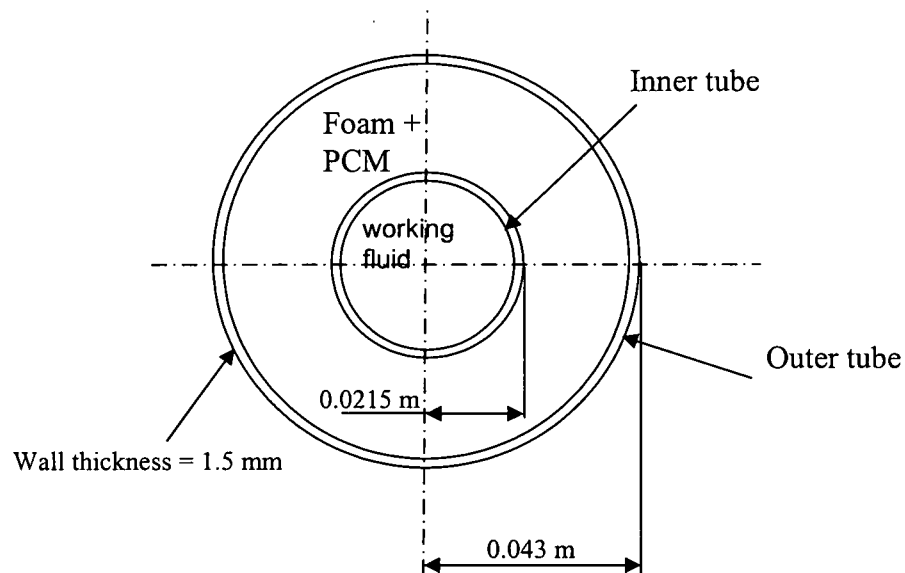


Fig. (5.25) Computational model for the energy Storage

above the melting point of the PCM by 200 °C. During the eclipse time, the outer wall of the canister was assumed to be insulated. The output energy from the solar receiver is obtained continuously from the working fluid that is flowing inside the inner tubes. The simulation for this energy storage was carried out for three consequent heating cycles.

The change of the output power delivered to the working fluid from the solar receiver for pure PCM and for foam enhancer with different thermal conductivity is shown in Fig. (5.26). The average value of the output power increased with increasing the thermal conductivity of the enhancer foam, however, for pure PCM the output power was more stable and uniform. It was noticed that increasing the thermal conductivity of the foam over a certain limit did not bring any more improvement. For this particular case, it was above 15 W/mK, which means enhancing the PCM by more than 800%. This happened

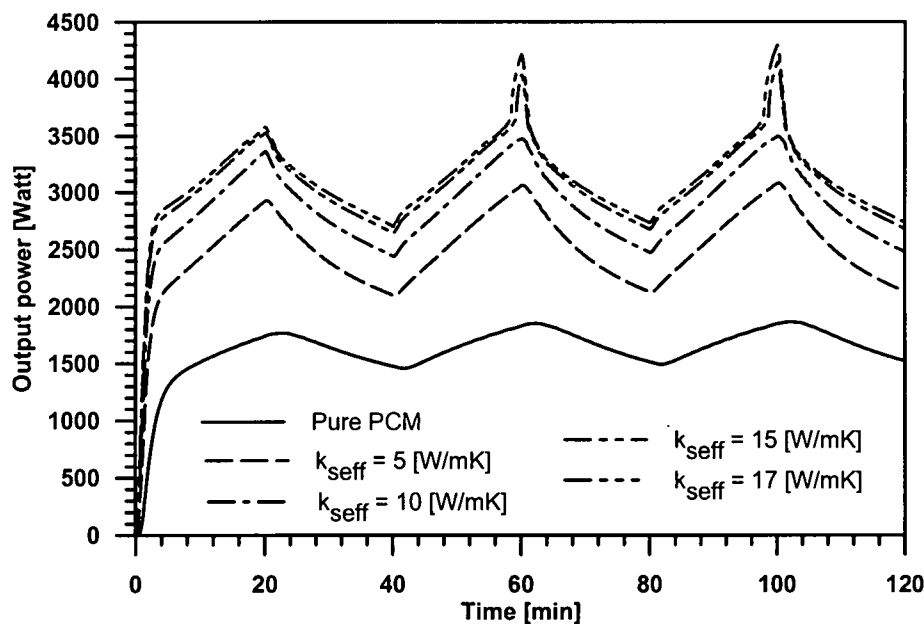


Fig. (5.26) Output power from the solar receiver for different foam thermal conductivity

because after enhancing the PCM by this value for the assumed value of the outside shell temperature, the PCM was completely melted during the first cycle charging period as shown in Fig. (5.27). Changing the pore size of the foam in this case did not bring any difference because of the absence of the liquid phase motion inside the porous media.

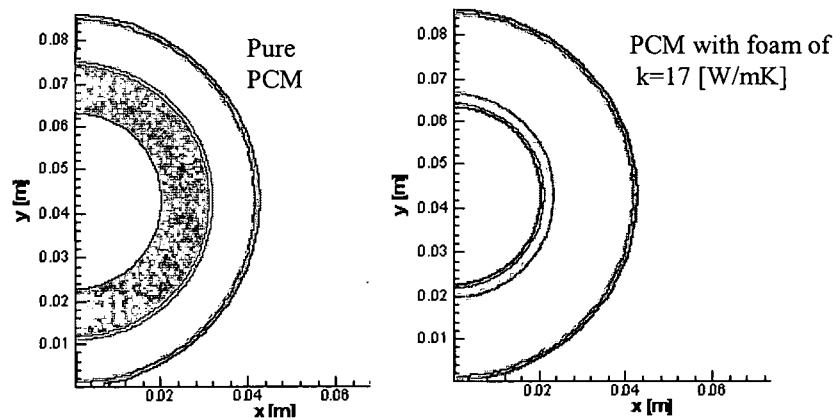


Fig. (5.27) Liquid fraction contours at the end of first cycle charging time, Time =20 min

5.5.2 Using Aluminum foam in energy storage for ground applications

The same configuration for the solar receiver could be used as a low melting temperature PCM energy storage to store energy from a fluctuating heat source for ground applications. A low melting temperature PCM, Ecosane, was used in this case. The same boundary conditions for the case of the solar collector were considered except that the outer wall of the canister was considered to be subjected to a convection heat transfer from another hot fluid flowing around the outer tube during the charging period. At the discharging period, the outer tube wall also was kept insulated. The working fluid inside the inner tube was considered to be just below the PCM melting temperature. In this

case, the motion of the molten phase of the PCM was considered and high porosity aluminum foams were used to enhance the PCM thermal conductivity.

The solid liquid interface is portrayed in Fig.(5.28) for the pure PCM between the two cylinders at different times during the three charging-discharging cycles. At the end of the charging period for the first cycle, 20 minutes, a considerable thickness of the PCM was melted. The melted region at the top and the bottom of the tube became thicker because of the creation of Benard convection cells at the bottom and the motion of the hot liquid beside

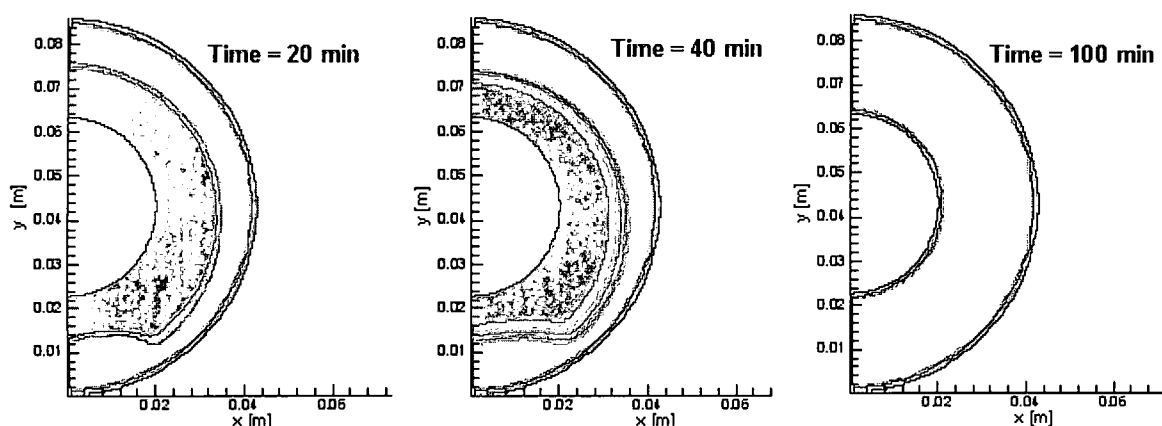


Fig (5.28) Liquid fraction contours for pure PCM at different times

outer wall upward to the top region respectively. During the discharge time where there was no heat coming from the outer cylinder wall, the interface started to get thicker. This happened because of the heat diffusion inside the PCM and the solidification of some of the PCM during the discharging period. It was found that the PCM did not melt completely until the third charging cycle. While, for using

Aluminum foam with 97% porosity, it was found that the total PCM was melted during the first charging cycle.

The output power was nearly zero for the pure PCM case during the first cycle because of its lower thermal conductivity as shown in Fig. (5.29). The output power did not increase until the liquid solid interface nearly reached the inner cylinder wall. Adding aluminum foam enhancer improved the energy absorption of the storage and increased the output power incredibly. The estimated value of the average output power using Aluminum foam of porosity 97% was about five times greater than that for using pure PCM. As shown in Fig.(5.29), the enhancement of the output power decreased with reducing the foam porosity, it did not change significantly after reducing the foam porosity below 90%.

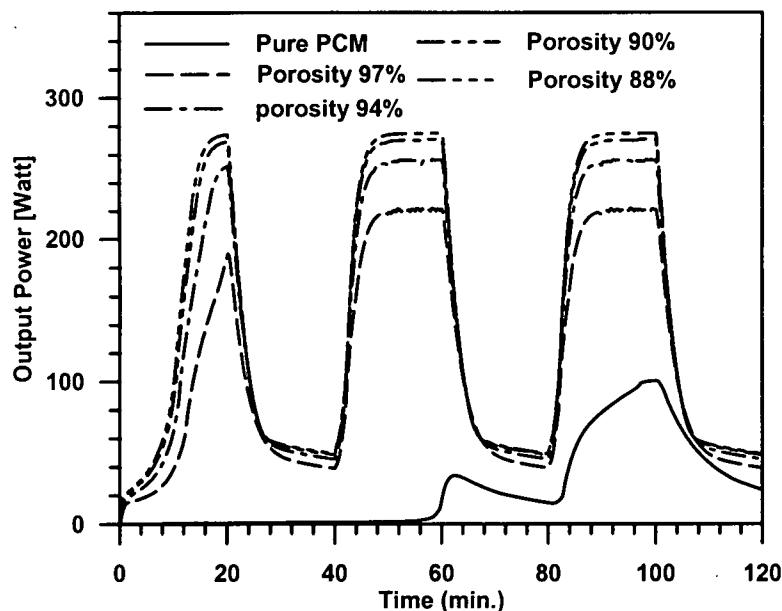


Fig. (5.29) Changing of energy storage output power with time for using different porosity Al foam

As a result of considering the PCM liquid phase motion, changing the foam pore size affected the output power of the storage. The output power amplitude increased by about 9% for increasing the pore size from 40PPI to 5 PPI as shown in Fig. (5.30). The enhancement due to using bigger pore sizes was not as high as the improvement due to changing the foam porosity, because the thickness of the PCM layer was not so big, it was about 2 cm, and the convection motion of the liquid phase was limited.

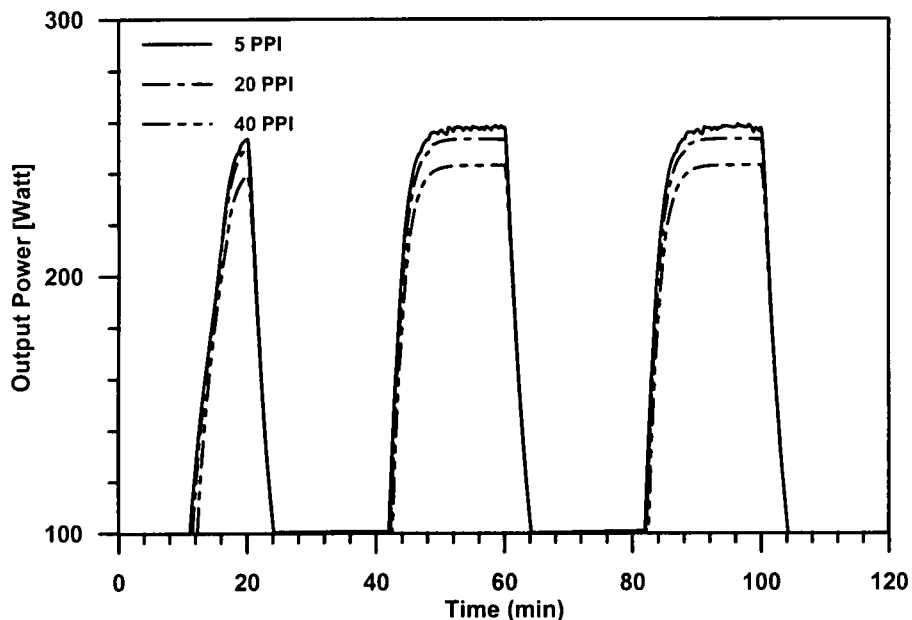


Fig. (5.30) Changing of energy storage output power with time for using different pore size Al foam

CHAPTER 6

CONCLUSIONS AND RECOMMENDATIONS

Solid to liquid phase change materials including paraffin waxes, metallic alloys and inorganic salts undergo reversible phase transitions, and act as thermal capacitors. In the past, they were used for passive solar energy storage. These materials also can be used in cooling applications for electronic devices.

Most PCMs exhibit a low density, suitable melting point for cooling applications, and high latent heat but low thermal conductivity. The lower thermal conductivity causes slow cooling response to the transient heating, which may lead to spike temperatures. Similar problems occur in energy storage systems, which reduce heat charging and discharging rates. Enhancing thermal conductivity of PCMs has a great impact on the design of heat sinks for modern electronic devices and a new generation of energy storage devices for energy harvesting systems.

In the last ten years, a great development has been carried out in the manufacture of graphite and metallic open cell foam materials. These foams exhibit high thermal conductivity, light weight, and good mechanical properties. Infiltrating these foams with appropriate PCM's can open a generation of new composite materials that may be used in thermal management applications,

especially for cooling electronic devices and for the space energy storage. The foam material serves as a heat carrier, and the PCM as heat storage. Due to the large difference in thermal properties of foam and PCM, the phase change of the PCM from solid to liquid and vice versa, and the complicated nature of the heating load, the heat transfer behavior in such systems seems to be very complex.

In this study, we used both theoretical and experimental techniques to investigate the heat transfer phenomena and solid-liquid PCM phase transition inside high thermal conductivity foams. Through the theoretical work, we developed a numerical code based on solving the volume averaged conservation equations of mass, momentum, and energy with phase change in porous media. A finite difference technique based on control volume approach with a non-staggered curvilinear body fitted grid was used to be suitable in dealing with regular or irregular geometries. Energy transport in this system was studied using a two-equation model to be able to consider local thermal non-equilibrium between the solid material of the foam and the PCM. The natural convection motion of the molten liquid of PCM inside the porous matrix was studied considering Darcy, Brinkmann, and Forchheimer effects. To close up the mathematical model, simple analytical models were developed for the effective thermal conductivity of high porosity metallic foams and for the wettability of small pore size carbon foam.

In the experimental investigation, a test rig was built to validate the numerical work. High porosity metal Aluminum foams and high thermal

conductivity carbon foams were used as the porous material, and low melting temperature paraffin wax was used as the PCM. The temperature field was measured at different points inside the test rig while the phase change interface was captured at different times through the melting process. Upon comparing experimental measurements and numerical results, it was found that the numerical model has predicted the temperature field and solid-liquid interface location with good accuracy. A parametric study was carried out to investigate the key parameters that affect the performance of foam-PCM composite as a heat sink for electronic devices and for energy storage applications.

Some key conclusions can be summarized as follows:

The numerical model showed good agreement with the experimental data for melting of PCM inside high thermal conductivity foams. Numerical analysis showed that heat transfer phenomena is far from local thermal equilibrium, the solid phase temperature and the PCM phase temperature deviated too much from each other. The code is robust and generic to study heat transfer behavior of PCM-foam systems.

Many parameters seem to affect the heat transfer behavior of PCM-foam systems. Some of these parameters are dependent on the properties of the foam (such as porosity, thermal conductivity, pore size, and surface characteristics) and PCM (melting point, latent heat, and viscosity of the liquid phase). Surface activation can improve the foam PCM absorption and enhance the heat transfer process. In addition, the convection motion of PCM molten liquid has a large effect. It enhances the heat transfer and accelerates the melting rate of the PCM.

High thermal conductivity foams could be a good method to enhance PCM thermal conductivity. Thermal conductivity of paraffin wax was increased fourteen times by using Aluminum foam with 97% porosity.

The parametric study for using foam-PCM composites in heat sink and energy storage applications showed the following results:

- 1- Decreasing foam porosity improves the performance of the heat sink since low porosity foam exhibits high thermal conductivity, but its lower permeability reduced the liquid convection motion.
- 2- Using foam with large pore size improves the performance of the heat sink for steady heat generation.
- 3- Increasing the interfacial heat transfer coefficient by enhancing foam-PCM wettability enhances the performance by more than five percent.
- 4- Adding fins inside foam to enhance heat spreading could be useful but increasing the number of the fins can bring the opposite effect.
- 5- Changing orientation and shape were found to be the most important parameters that can affect the heat sink performance for steady heat generation.
- 6- Using a PCM could be a very effective solution for designing heat sinks for electronic chips subjected to heat generation spikes. Lower melting point and higher latent heat resulted in better performance.
- 7- For energy storage applications, using foam material can enhance the output power of the storage significantly. In space applications,

enhancing thermal conductivity was the main parameter since the buoyancy effect is minimal due to the absence of gravity.

- 8- In ground energy storage applications, decreasing foam porosity and increasing pore size enhanced storage output power.

Based on the results gained throughout this study, additional research works would be fruitful:

- 1- Using the developed model to study 3-D heat sink. This can be done easily by extending the current numerical code to 3-D. However, any calculation would require high performance computer resources.
- 2- Validating the proposed model for the foam wettability experimentally
- 3- Performing an extensive experimental study on the micro-heat transfer at the interface between the foam and PCM during phase change process.
- 4- Performing more experimental study on the effect of using coated foam with different materials, which can change flow resistance and interfacial heat transfer coefficient between the two phases.

REFERENCES

- 1- Crank J., Free and Moving Boundary Problems, 1984, Claredon Press, Oxford
- 2- Zerroukat, M and Chatwin, C. R., 1994, Computational Moving Boundary Problems, Taunton, Somerset, England: Research Studies Press; John Wiley and Sons, New York
- 3- Soma Das and Tapas Dutta, 1993, "Mathematical modeling and experimental studies on solar energy storage in a phase change material", Solar Energy, Vol. 51, No. 5, pp. 305-312
- 4- Bareiss, M. and Beer, H., 1984, "An analytical solution of the heat transfer process during melting of an unfixed solid phase-change material inside a horizontal tube", Int. Journal of Heat and Mass Transfer, Vol. 27, No. 5, pp. 739-746
- 5- Moallemi, M.K., and Viscanta, R., 1985, "Analysis of close-contact melting heat transfer", Int. Journal of Heat and Mass Transfer, Vol. 29, pp. 855-867
- 6- Lacroix, M., 2001, "Contact melting of a phase change material inside a heated parallelepipedic capsule", Energy Conversion & Management, Vol. 42, pp. 35-47

- 7- Hoseon Yoo, Hiki Hong, and Charn-Jung Kim, 1998, "Effects of transverse convection and solid-liquid density difference on the steady close-contact melting", *Int. Journal of Heat and Fluid Flow*, Vol. 19, pp. 368-373
- 8- Wang, Y., Amiri, A., and Vafai, K., 1999, "An experimental investigation of the melting process in a rectangular enclosure", *Int. Journal of Heat and Mass Transfer*, Vol. 42, pp. 3659-3672
- 9- Gau, C. and Viskanta R., 1984, "Melting and solidification of a metal system In a rectangular cavity", *Int. Journal of Heat and Mass Transfer*, Vol. 27, No.1, pp. 113-123
- 10-Gau, C. and Viskanta, R., 1986, "Melting and solidification of pure metal on a vertical wall", *Journal of Heat Transfer*, ASME, Vol. 108, pp. 174-181
- 11-Ho, C.J., and Viskanta, R., 1984, "Heat transfer during melting from an isothermal vertical wall", *Journal of Heat Transfer*, ASME, Vol. 106, pp. 12-19
- 12-Debabrata, P., and Joshi, Y.K., 2001, "Melting in a side heated tall enclosure by a uniformly dissipating heat source", *Int. Journal of Heat and Mass Transfer*, Vol. 44, pp.375-387
- 13-Jianfeng, W., Yingxiu Ouyang, and Guangming Chen, 2001, " Experimental study of charging process of a cylindrical heat storage capsule employing multiple-phase-change materials", *Int. Journal of Energy Research*, Vol. 25, pp. 439-447

- 14-Ahmet Sari, Kamil Kaygusuz, 2002, "Thermal performance of palmitic acid as a phase change energy storage material", *Energy Conversion And Management*, Vol. 43, pp. 863-876
- 15-Gulseren Baran, and Ahmet Sari, 2003, "Phase change and heat transfer characteristics of a eutectic mixture of palmitic and steric acids as PCM in a latent heat storage system", *Energy Conversion and Management*, Vol. 44, pp. 3227-3246
- 16-Giovanni Casano, and Stefano Piva, 2002, "Experimental and numerical investigation of the steady periodic solid-liquid phase-change heat transfer", *Int. Journal of Heat and Mass Transfer*, Vol. 45, pp. 4181-4190
- 17-Patankar, S. V., 1980, *Numerical Heat Transfer and Fluid Flow*, Hemisphere, Washington, DC
- 18-Tanahill, J.C., Anderson, A., and Pletcher, R., 1984, *Computational Fluid Mechanics and Heat Transfer*, Taylor and Francis
- 19-Ye, T., Mittal, R., udaykumar, H.S., and Shyy, W., 1999, "An accurate cartesian grid method for viscous incompressible flows with complex immersed boundaries", *Journal of Computational Physics*, Vol. 156, pp. 209-240
- 20-Pope,S.B., 1978, "The calculation of turbulent re-circulating flows in general orthogonal coordinates", *Journal of Computational Physics*, Vol. 26, No. 2, pp 197-217

- 21-Rhie, C.M., and Chow, W.L., 1983, "Numerical study of the turbulent flow past an airfoil with trailing edge separation", AIAA Journal, Vol. 21, pp.1525-1533
- 22-Zang, Y., Street, L. R., and Koseff, J. R., 1994, "A non-staggered grid, fractional step method for time-dependent incompressible Navier-Stokes equations in curvilinear coordinates", Journal of Computational Physics, Vol. 114, pp. 18-33
- 23-Warsi, Z. U., Thompson, J. F., and Mastin, C. W., 1985, "Numerical Grid Generation Foundations and Applications", North Holland, Amsterdam
- 24-Eiseman, P.R., 1987, "Adaptive grid generation", Computer Methods in Applied Mechanics and Engineering, Vol. 64, pp. 321-376
- 25-Sparrow, E., Patankar, S. V., and Ramadhyani, S., 1977, "Analysis of melting in presence of natural convection in the melt region", Journal of Heat Transfer, ASME, Vol. 99, pp. 520-526
- 26-Yong K. W. and Lacroix, M., 1995, " Melting of a PCM inside a vertical cylindrical capsule," Int. Journal for Numerical Methods in Fluids, Vol. 20, pp. 559-572
- 27-Damir, J. and Gretar, T., 1996, "A front-tracking method for dendritic solidification", Journal of Computational Physics, Vol. 123, 127-148
- 28-Attinger, D., and Poulikakos, D., 2001, "Melting and resolidification of a substrate caused by molten microdroplet impact", Journal of Heat Transfer, ASME, Vol. 123, pp. 1110-1122

- 29-Sripada, S.S., Cohen, I.M., Ayyaswamy, P.S., 2003, "Melting of a wire anode followed by solidification: A three-phase moving interface problem", *Journal of Heat Transfer*, ASME, Vol. 125, pp.661-668
- 30-Dursunkaya, Z., and Odabasi, G., 2003, "Numerical solution of solidification in square prism using an algebraic grid generation technique", *Heat and Mass Transfer*, Vol. 40, pp. 91-97
- 31-Kamal, A.R., Maria Das Gracas E. da Silva, 2003, "Melting of PCM around a horizontal cylinder with constant surface temperature", *Int. Journal of Heat and Mass Transfer*, Vol. 42, pp. 1145-1152
- 32-Voller, V.R., and Swaminathan, C.R., 1990, "Fixed grid techniques for phase change problems: A review", *Int. Journal for Numerical Methods in Engineering*, Vol. 30, pp. 875-898
- 33-Brent, A. D., Voller, V.R., and Reid, K.J., 1988, "Enthalpy-porosity technique for modeling convection-diffusion phase change: Application to the melting of a pure metal", *Numerical Heat Transfer*, Vol. 13, pp. 297-318
- 34-Asako, Y.m Faghri, M., Charmchi, M., and Bahrami, P.A., 1994, "Numerical solution for melting of unfixed rectangular phase-change material under low-gravity environment" *Numerical Heat Transfer, Part A*, Vol. 25, pp.191-208
- 35-Asako, Y.m Faghri, M., 1999, "Effect of density change on melting of unfixed rectangular phase-change material under low gravity environment", *Numerical Heat Transfer, Part A*, Vol. 36, pp. 825-838

- 36-Rady,M.A., and Mohanty, A.K., 1996, "Natural convection during melting and solidification of pure metals in a cavity", Numerical Heat Transfer, Part A, Vol. 29, pp.49-63
- 37-Ghasemi, B., and Molki, M., 1999, "Melting of solids in square cavities", Int. Journal of Heat and Fluid Flow, Vol. 20, pp. 446-452
- 38-Sasaguchi, K., Kunsano, K., and Viskanta, R., 1997, "A numerical analysis of solid-liquid phase change heat transfer around a single and two horizontal, vertically spaced cylinders in a rectangular cavity", Int. Journal of Heat and Mass Transfer, Vol. 40, pp. 1343-1354
- 39-Ng, K.W., Gong, Z.X., and Mujumdar, A.S., 1998, "Heat transfer in free convection-dominated melting of a phase change material in a horizontal annulus" Int. Comm. Heat Mass Transfer, Vol. 25, pp. 631-640
- 40-Khillarkar, D.B., Gong, Z.X., and Mujumdar, A.S., 2000, "Melting of a phase change material in concentric horizontal annuli of arbitrary cross-section", Applied Thermal Engineering, Vol. 20, pp. 893-912
- 41-Fulvio Stella, and Marilena Giangi, 2000, "Melting of a pure metal on a vertical wall: Numerical simulation", Numerical Heat Transfer, Part A., Vol. 38, pp. 193-208
- 42-Scanlon, T.J., and Stickland, M.T., 2004, "A numerical analysis of buoyancy-driven melting and freezing", Int. Journal of Heat and Mass Transfer, Vol. 47, pp. 429-436

- 43-Ilegbusi, O.J., and Mat, M.D., 1998, "Modeling flowability of mushy zone with a hybrid model utilizing coherency solid fraction", *Materials Science and Engineering A*, Vol. 247, pp. 135-141
- 44-Ilegbusi, O.J., and Mat, M.D., 2002, "Application of a hybrid model of mushy zone to macrosegregation in alloy solidification", *Int. Journal of Heat and Mass Transfer*, Vol. 45, pp. 279-289
- 45-Shyy, W., et al., 1996, *Computational Fluid Dynamics With Moving Boundaries*, Taylor and Francis
- 46-Udaykumar, H.S., Mittal, R., and Shyy Wei, 1999, "Computation of solid-liquid phase fronts in the sharp interface limit on fixed grids", *Journal of Computational Physics*, Vol. 153, pp. 535-574
- 47-Bugaje Ml., 1997, "Enhancing the thermal response of latent heat storage systems", *Int. Journal of Energy Research*, Vol. 21, 759-766
- 48-Chow, L.C., Zhong, J.K., and Beam, J.E., 1996, "Thermal conductivity enhancement for phase change storage media", *Int. Comm. Heat Mass Transfer*, Vol. 23, pp. 91-100
- 49-Siegel , R., 1977, "Solidification of low conductivity material containing dispersed high conductivity particles", *Int. Journal of Heat and Mass Transfer*, Vol. 20, pp. 1087-1089
- 50-Velraj, R., Seeniraj, R.V., Hafner, B., Faber, C., and Schwarzer, K., 1999, "Heat transfer enhancement in a latent heat storage", *Solar Energy*, Vol. 65, pp. 171-180

- 51-Cabeza, L.F., Mehling, H., Hiebler, S., and Ziegler, F., 2002, "Heat transfer enhancement in water when used as PCM in thermal energy storage", *Applied Thermal Engineering*, Vol. 22, pp. 1141-1151
- 52-Uros Stritih, 2004, "An experimental study of enhanced heat transfer in rectangular PCM thermal storage", *Int. Journal of Heat and Mass Transfer*, Vol. 47, pp. 2841-2847
- 53-Fukai J, Kanou M, Kodama Y, Miyatake O., 2000, "Thermal conductivity enhancement of energy storage media using carbon fibers", *Energy Conversion & Management*, Vol. 41, pp. 1543-1556
- 54-Fukai, J., Hamada, Y., Morozumi, Y., and Miyatake, O, 2002, "Effect of carbon-fiber brushes on conductive heat transfer in phase change materials", *Int. Journal of Heat and Mass Transfer*, Vol. 45, pp. 4781-4792
- 55-Hamada, Y. Ohtsu, W., and Fukai, J., 2003, "Thermal response in thermal energy storage material around heat transfer tubes: Effect of additives on heat transfer rates", *Solar Energy*, Vol. 75, pp. 317-328
- 56-Hoogendoorn, C.J., and Bart, G.C., 1992, "Performance and modeling of latent heat storage", *Solar Energy*, Vol. 48, pp. 53-58
- 57-Erk H, Dudukovic M., 1996, "Phase change heat regenerators: Modeling and experimental studies", *AIChE J.*, Vol. 42, pp. 791-808
- 58-Chapotard C, Tondeur D., 1983, "Dynamics of latent heat storage in fixed beds, a non-linear equilibrium model, the analogy with chromatography", *Chem. Eng. Commun.*, Vol. 24, pp. 183-204

- 59-Mauran S, Prades P, L'haridon F., 1993, "Heat and mass transfer in consolidated reacting beds for thermochemical systems", Heat Recovery Systems & CHP, Vol. 4, pp. 315-319
- 60-Py X, Olives R, Mauran S., 2001, "Paraffin/porous graphite-matrix composite as a high and constant power thermal storage material", Int. J. of Heat and Mass Transfer, Vol. 44, pp. 2727-2737
- 61-Maxwell, J.C., 1954, A Treatise on Electricity and Magnetism, Vol. 1, Oxford University Press, 1891, Reprinted by Dover, New York
- 62-Kaviany, M, 1995, Principles of Heat Transfer In Porous Media, Springer, New York
- 63-Calmidi, V.V., and Mahajan, R.L., 1999, "The effective thermal conductivity of high porosity fibrous metal foams", Journal of Heat Transfer, ASME, Vol. 121, pp. 466-471
- 64-Boomsma, K., and Poulikakos, D., 2001, "On the effective thermal conductivity of a three-dimensionally structured fluid-saturated metal foam", Int. Journal of Heat and Mass Transfer, Vol. 44, pp. 827-836
- 65-Peak, J.W., Kang, B.H., Kim, S.Y., and Hyun, J.M., "Measurement of effective thermal conductivity and permeability on aluminum foam metal", Direct contact with ERG Materials and Aerospace
- 66-Bhattacharya, A., Calmidi, V.V., and Mahajan, R.L., 2002, "Thermophysical properties of high porosity metal foams", Int. Journal of Heat and Mass Transfer, Vol.45, pp. 1017-1031

- 67-Du Plessis, P., Montillet, A., Comiti, J., and Legrand, J., 1994, "Pressure drop prediction for flow through high porosity metallic foams", *Chemical Engineering Science*, Vol. 49, pp. 3545-3553
- 68-Fourie, J.G., and Du Plessis, J.P., 2002, "Pressure drop modeling in cellular metallic foams", *Chemical Engineering Science*, Vol. 57, pp. 2781-2789
- 69-Weaver, J. A., and Viskanta, R., 1986, "Freezing of Water Saturated Porous Media in a Rectangular Cavity", *Int. Commun. Heat Mass Transfer*, Vol. 13, pp. 245-252
- 70-Chellaiah, S., and Viskanta, R., 1989, "Freezing of water-saturated porous media in the presence of natural convection: Experiments and analysis", *Journal of Heat Transfer*, ASME, Vol. 111, pp. 425-432
- 71-Chang, W., and Yang, D., 1996, "Natural convection for the melting of ice in porous media in a rectangular enclosure", *Int. Journal of Heat and Mass Transfer*, Vol. 39, pp. 2333-2348
- 72-Beckermann, C., and Viskanta, R., 1988, "Natural convection solid/liquid phase change in porous media", *Int. Journal of Heat and Mass Transfer*, Vol. 31, pp. 35-46
- 73-Harris, K.T., Haji-sheikh, A., and Agwu, A. G., 2001, "Phase change phenomena in porous media- A non-local thermal equilibrium model", *Int. Journal of Heat and Mass Transfer*, Vol. 44, pp. 1619-1625

- 74-Vafai, K., and Sozen, M., 1990, "Analysis of energy and momentum transport for fluid flow through porous media", Journal of Heat Transfer, ASME, Vol. 112, pp. 690-699
- 75-Vafai, K., and Sozen, M., 1990, "An investigation of latent heat storage porous bed and condensing flow through it" Journal of Heat Transfer, ASME, Vol.112, pp.1014-1022
- 76-Calmidi, V., and Mahajan, R., 2000, "Forced convection in high porosity metal foams", Journal of Heat Transfer, ASME, Vol. 122, pp. 557-565
- 77-Phanikumar, M., and Mahajan, R., 2002, "Non-darcy natural convection in high porosity metal foams", Int. Journal of Heat and Mass Transfer, Vol. 45, pp. 3781-3793
- 78-Whitaker, S., 1999, "The Method of Volume Averaging," Kluwer Academic Publishers, Norwell, Ma, USA
- 79-Nakayama, A., Kuwahara, F, Umemoto, T., and Hayashi, T., 2002, "Heat and fluid flow within an anisotropic porous medium", Journal of Heat Transfer, ASME, Vol. 124, pp. 746-753
- 80-Quintard, M. and Whitaker, S., 1993, "One- and two-equation models for transient diffusion processes in two-phase systems", Advances in Heat Transfer, Vol. 23, pp. 369-465
- 81-Hsu, C. T., 1999, "A closure model for transient heat conduction in porous media", Journal of Heat Transfer, ASME, Vol. 121, pp.733-739

- 82-Li, J., Peterson, G.P., and Cheng, P., 2004, "Three-dimensional analysis of heat transfer in a micro-heat sink with single phase flow", *Int. Journal of Heat and Mass Transfer*, Vol. 47, pp. 4215–4231
- 83-Bhattacharya, A., and Mahajan, R.L., 2002, "Finned metal Foam heat sinks for electronics cooling in forced convection", *Journal of Electronic Packaging*, ASME, Vol. 124, pp. 155-163
- 84-Hasnain S.M., 1998, "Review on sustainable thermal energy storage technologies, part I: Heat storage materials and technologies", *Energy Conversion and Management*, Vol. 39, pp. 1127-1138
- 85-T.J. Lu, 2000, "Thermal Management of high power electronics with phase change cooling", *Int. Journal of Heat and Mass Transfer*, Vol. 43, pp.2245-2256
- 86-Suman Chakraborty, and Pradip Dutta, 2003, "Analytical solution for heat transfer during cyclic melting and freezing of phase change material used in electronic or electrical packaging", *Journal of Electronic Packaging*, Vol. 125, pp. 126-133
- 87-Siva p. Gurram, Yogendra K. Joshi, and Jungho Kim, 2002, "Thermal management of high temperature pulsed electronics using metallic phase change materials", *Numerical Heat Transfer, Part A*, Vol. 42, pp. 777-790
- 88-Evan A.G, He,M.Y., Hutchinson, J.W., and Shaw, M., 2001, " Temperature distribution in advanced power electronics systems and the effect of phase change materials on temperature suppression during power pulses", *Journal of Electronic Packaging*, ASME, Vol. 123, pp. 211-217

- 89-Marc Hodes et. al., 2002, "Transient thermal management of a handset using Phase Change Material (PCM)", Journal of Electronic Packaging, Vol. 124, pp. 419-426
- 90-F.L. Tan, and C.P. Tso, 2004, "Cooling of mobile electronic devices using phase change materials", Applied Thermal Engineering, Vol. 24, pp. 159-169
- 91-M.J. Huang, P.C. Eames, and B. Norton, 2004, "Thermal regulation of building-integrated photovoltaics using phase change materials", Int. Journal of Heat and Mass Transfer, Vol. 47, pp. 2715-2733
- 92-Writz, R.A., Ning Zheng, and Dhanesh Chandra, "Thermal management using dry phase change materials", Proc. Fifteenth IEEE Semiconductor Thermal Measurement and Management Symposium, March 1999, San Diego, CA
- 93- Writz, R.A., Shuo Peng, and Alan Fuchs, "A Polymer-based thermal energy storage composite for temperature control of sensors and electronics", The 6th ASME-JSME Thermal Engineering Joint Conference, March 2003
- 94-D. Pal, and Y.K. Joshi, 1997, "Application of phase change materials to thermal control of electronic modules: A computational study", Journal of Electronic Packaging, Vol. 119, pp. 40-50
- 95-Marsu Ishizuka, 2004, "Operation time control of a high density packaging using a low melting point alloy", IEEE Transactions on Components and Packaging Technologies, Vol. 27, No. 2, pp. 239-243

- 96-Shankar Krishnan and Suresh V. Garimella, 2004, "Analysis of a phase change energy storage system for pulsed power dissipation", IEEE Transactions on Components and Packaging Technologies", Vol. 27, pp. 191-199
- 97-Shankar Hrishnan, and Suresh V. Garimella, 2004, "Thermal management of transient power spikes in electronics – phase change energy storage or copper heat sinks", Journal of Electronic Packaging, Vol. 126, pp. 308-316
- 98-Assar, A.M., 1997, "Mould surface roughness and interfacial heat transfer using heat flow model", Materials Science and Technology, Vol. 13, pp. 702-704
- 99-Loulou, T., Artiyukhin, E.A., and Bardou, J.P., 1999, "Estimation of thermal contact resistance during the first stages of metal solidification process: II- Experimental setup and results", Int. Journal of Heat and Mass Transfer, Vol. 42, pp. 2129-2142
- 100- Taha, M.A., El-Mahallawy, N.A., El-Mestekawi, M.T., And Hassan A.A., 2001, "Estimation of air gap and heat transfer coefficient at different faces of Al and Al-Si castings solidifying in permanent mould", Material Science and Technology, Vol. 17, pp. 1093-1101
- 101- Narayan, K., and Griffiths, W.D., 2002, "One-dimensional predictive model for estimating of interfacial heat transfer coefficient during solidification of cast iron in sand mould", Material Science and Technology, Vol. 18, pp. 804-810

- 102- Wang, G.X., and Matthys, E.F., 2002, "Experimental determination of the interfacial heat transfer during cooling and solidification of molten metal droplets impacting on metallic substrate: effect of roughness and superheat", *Int. Journal of Heat and Mass Transfer*, Vol. 45, pp. 4967-4981
- 103- Syed M.S. Wahid, 2003, "Numerical analysis of heat flow in contact heat transfer", *Int. Journal of Heat and Mass Transfer*, Vol. 46, pp. 4751-4754
- 104- Prasher, R.S., Shipley, J., Koning, P., and Wang, J., 2003, "Thermal resistance of particle laden polymeric thermal interface material", *Journal of Heat Transfer*, ASME, Vol. 125, pp. 1170-1177
- 105- Ravi, S. Prasher, 2001, "Surface chemistry and characteristics based model for the thermal contact resistance of fluidic interstitial thermal interface materials", *Journal of Heat Transfer*, ASME, Vol. 123, pp. 969-975
- 106- Vafaj, K., and Tien, L.C., 1981, "Boundary and inertial effects on flow and heat transfer in porous media", *Int. Journal of Heat and Mass Transfer*, Vol. 24, pp. 195-203
- 107- Feustel, H.E., 1995, "Simplified numerical description of latent storage characteristics for phase change wallboard", Lawrence Berkeley Laboratory report LBL-36933
- 108- Kline, J., and McClintok, F.A., 1953, "Describing uncertainties in single-sample experiments", *Mechanical Engineering*, Vol. 75, pp. 3-8

R70203/980

- 109- Carsie, A. Emmanuel K., Joseph, N., and Kerslake, T.W., "Parametric analysis of cyclic phase change and energy storage in solar heat receivers", 32nd Intersociety Energy Conversion Engineering Conference, Honolulu, Hawaii, July 27-August 1, 1997
- 110- Yu-Ming Xing, Xin Xu, Xiugan Yuan, Hai-Ting Cui, Yun-hao Zhang, 2004, "Numerical simulation of high-temperature phase change heat storage system", Heat Transfer – Asian Research, Vol. 33, pp. 32-41